Transducers for Sound and Vibration - FEM Based Design

Liu, Bin

Publication date:
2001

Transducers for Sound and Vibration
- The Finite Element Method Based Design

Bin Liu

June 2001

Department of Manufacturing Engineering and Management
Technical University of Denmark

Transducers for Sound and Vibration

- The Finite Element Method Based Design

Published and distributed by:
Section for Production Technology
Department of Manufacturing Engineering and Management
Technical University of Denmark

Publication no. IPL-055-01

Printed in Denmark

Preface

This thesis was written as part of fulfillment of the Ph.D. degree at the Technical University of Denmark (DTU).

The project was completely financially supported by Brüel & Kjær Sound & Vibration A/S.

The goal of this project is to develop transducers for sound and vibration better and faster by means of the numerical method.

The lab work on the processing of piezoelectric accelerometers and on the measuring of condenser microphones was done by Brüel & Kjær employees.

Acknowledgements

During the project many people have been involved helping in different ways. First, I would like to thank my supervisor at the Section of Production Technology, Torben Lenau, who has been a support to me during the project. In the same way I also would like to thank Dan Ulrich who is my former project leader at Brüel & Kjær and Jens Ole Gulløv who is the company contact person from Brüel & Kjær.

The staff at Brüel & Kjær have been very kind and helpful and I would like to thank them for their invaluable help, in particular Knud Styhr Hansen, Lars Munch Kofoed, and Birger Kriegbaum for comments and discussions on piezoelectric accelerometers, and Patrick Scheeper for all measurement and the inspiring discussions on microphones.

Nærum, June 2001

Bin Liu
Ph.D. no. P 972967
Department of Manufacturing Engineering and Management
Technical University of Denmark

Brüel & Kjær Sound & Vibration A/S
Tel: +45 7741 2328
E-mail: binliu@bksv.com

Abstract

Transducers for Sound and Vibration
---The Finite Element Method Based Design

The design of transducers for sound and vibration based on the Finite Element Method (FEM) is described in this thesis. Here transducers for sound and vibration are condenser microphones and piezoelectric accelerometers.

According to the study of piezoelectric accelerometers' specifications, Chapter 2 presents the design considerations from a theoretical point of view. Besides these design considerations, in order to obtain better and faster design an efficient design method is needed as well. A comparison between the available development methods made in Chapter 3 shows that among the methods mentioned the FEM can make more accurate estimations of the design performances, simulate more detailed specifications, visualize simulated results, and improve the scientific understanding.

In order to demonstrate how to realize these advantages, Chapter 4 describes the detailed simulation procedure by simulating an existing piezoelectric accelerometer. The results substantiate that the FEM can be used to simulate the piezoelectric accelerometers to the degree of precision required for R&D for existing accelerometers and the FEM can improve the scientific understanding of piezoelectric accelerometers.

Based on the FE method described in Chapter 4, detailed analyses are made for different piezoelectric accelerometer designs in Chapter 5. The results show that with same seismic mass: (1) DeltaShear design has the highest sensitivity due to the contribution from the other components to the active seismic mass; (2) Annular Shear design has the highest mounted resonance frequency; (3) the Upright compression design has the biggest base bending effect; (4) the Planar shear design is the lightest.

Chapter 6 presents the design procedures of two new designs. Good agreements are achieved between the specifications of the physical and virtual prototypes. The results substantiate that the FEM can simulate the piezoelectric accelerometers to the degree of precision required for R&D for prevision accelerometers. Besides, detailed analyses such as the analysis of the thickness of the thick film, the analysis of the glue influence, etc. are made. All these works improve the scientific understanding of piezoelectric accelerometers.

After the description of the successful FEM implementation to the piezoelectric accelerometer design, the thesis describes the FEM application to the condenser microphone design. It has to be stated that the work behind this part is not aiming to simulate all detailed microphone specifications since we for example cannot calculate on the microphone acoustics due to the

fact that the strong point of the commercial code used for this project is structure analysis. The main purpose is to simulate the open-circuit sensitivity and the diaphragm collapse voltage.

Traditional condenser microphones based on precision mechanics and silicon condenser microphones based on micro-mechanics are discussed in this part. As presented in Chapter 7, the main construction difference between the two kinds of microphones related with the work done in this thesis is the shape of the diaphragm and the backplate. The traditional one has a circular diaphragm and a circular backplate while the silicon one has an octagonal diaphragm and a quadratic backplate.

The modeling of circular condenser microphones is described in Chapter 8. Good agreements are achieved between the simulated and analytical static deflection profile, fundamental resonance frequency, and collapse voltage. Comparisons between the simulated and measured capacitance and open-circuit sensitivity of two B & K Type 4190 ½″ microphones present good agreements. The optimization of the backplate dimension according to the open-circuit sensitivity is presented at last.

Chapter 9 presents the modeling of silicon condenser microphones. Due to the special shape of the diaphragm and the backplate, there is not any analytical model for these microphones. The FE simulation result is the only available reference for the fundamental resonance frequency, static deflection profile, collapse voltage and the open-circuit sensitivity. An experimental verification is made with three B & K silicon condenser microphones. Good agreements are achieved. At the end, the optimization of the backplate dimension according to the open-circuit sensitivity is made.

The work presented in Chapter 8 and 9 show: (1) the FEM can be used to simulate traditional and silicon condenser microphones to the degree of precision required for R&D for existing products; (2) the virtual prototype improves the scientific understanding of traditional and silicon condenser microphones; (3) the FE simulation gives designers the opportunity to go to the limits of what is physically possible with traditional and silicon condenser microphones to achieve the best design concerning the open-circuit sensitivity.

Finally, in Chapter 10 the most important conclusions of this thesis are summarized and some suggestions for the future work are given.

Abstrakt

Transducere til Lyd og Vibration
---Baseret på Finite Element Metoden

Denne Ph.D. afhandling beskriver design af transducere til lyd- og vibrationsmåling, baseret på Finite Element Metoden (FEM). De diskuterede transducere er kondensator mikrofoner og piezoelektriske accelerometre.

I Kapitel 2 præsenteres teoretiske designovervejelser vedrørende specifikationer på piezoelektriske accelerometre. For at få et bedre design i kortere tid, er der behov for en mere effektiv design metode. En sammenligning mellem forskellige design metoder i Kapitel 3 viser, at Finite Element Metoden kan give mere nøjagtige estimater af et designs specifikationer, og simulere flere detaljerede specifikationer end med analytiske metoder. Desuden kan resultaterne visualiseres, og den videnskabelige forståelse kan øges.

For at demonstrere disse fordele, vises et detaljeret eksempel af simulering af et piezoelektrisk accelerometer i Kapitel 4. Resultaterne viser, at Finite Element Metoden kan bruges til at simulere piezoelektriske accelerometre med den fornødne nøjagtighed til brug i udviklingsprojekter og samtidigt fremme den generelle videnskabelige forståelse af accelerometre.

Kapitel 5 beskriver en detaljeret undersøgelse af forskellige accelerometer designs, baseret på simuleringsmetoden fra Kapitel 4. Ved brug af samme seismiske masse viser simuleringerne at: (1) DeltaShear designet har den største følsomhed på grund af det største bidrag fra andre komponenter til den aktive seismiske masse; (2) Annular Shear designet har den største monterede resonans frekvens; (3) Upright Compression designet har den største følsomhed overfor base bøjning; (4) Planar Shear designet har den laveste masse.

To nye designs bliver præsenteret i Kapitel 6. En god overensstemmelse mellem specifikationerne af de fysiske- og virtuelle prototyper er opnået. Disse resultater bekræfter, at FEM kan simulere accelerometre med den fornødne nøjagtighed til R&D. Desuden er der lavet detaljerede undersøgelser af effekten af tykfilmens tykkelse, effekten af limfugen, o.s.v. Disse undersøgelser har fremmet den videnskabelige forståelse af piezoelektriske accelerometre.

Foruden den succesrige implementering af FEM til design af piezoelektriske accelerometre, beskriver denne afhandling også anvendelsen af FEM til design af kondensator mikrofoner. Udledning af specifikationer for kondensatormikrofonen, som kræver akustisk simulering er udeladt idet FEM ikke pt. er et oplagt værktøj til dette. Det primære formål er, at beregne mikrofonens open-circuit-følsomhed og membranens kollapsspænding.

Traditionelle (=finmekaniske) og mikromekaniske mikrofoner er beskrevet i denne del af afhandlingen. Som beskrevet i Kapitel 7, er den primære konstruktionsmæssige forskel mellem disse to typer kondensator mikrofoner membranens- og bagpladens facon. Den traditionelle mikrofon har et rund membran og rund bagplade, mens den mikromekaniske har et ottekantet membran og en kvadratisk bagplade.

Modellering af runde kondensator mikrofoner er beskrevet i Kapitel 8. En god overensstemmelse er opnået mellem den simulerede og den analytiske statiske membranudbøjning, den fundamentelle resonansfrekvens, og kollapsspændingen. En sammenligning mellem den simulerede og den målte kapacitet og open-circuit følsomhed af to B&K 4190 ½-inch microfoner viser en god overensstemmelse. Optimering af open-circuit følsomhed ved at finde den optimale bagpladestørrelse bliver også præsenteret.

Modellering af silicium kondensator mikrofoner bliver præsenteret i Kapitel 9. På grund af den specielle udformning af membran og bagplade, eksisterer der ikke analytiske modeller til disse mikrofoner. Finite Element simulering har givet unikke værdier for den fundamentelle resonansfrekvens, den statiske membranudbøjning, kollapsspændingen og open-circuit følsomhed. En eksperimentel sammenligning er lavet med tre B&K silicium kondensator mikrofoner. En god overensstemmelse er opnået. Optimering af bagpladestørrelse, for at finde den største open-circuit følsomhed, bliver også præsenteret.

Resultaterne fra Kapitel 8 og 9 viser, at (1) FEM kan bruges til at simulere traditionelle og silicium kondensator mikrofoner med den nødvendige præcision til brug i R&D; (2) virtuelle prototyper fremmer den videnskabelige forståelse af traditionelle og silicium kondensator mikrofoner; (3) FE simulering giver designere mulighed for at finde de fysiske grænser for open-circuit følsomheden for både traditionelle og silicium kondensator mikrofoner.

Endelig beskriver Kapitel 10 devigtigste konklusioner fra denne afhandling, og giver forslag til fremtidig forskning.

Nomenclature

a	acceleration
A	area
C_a	accelerometer capacitance
C_c	cable capacitance
C_I	preamplifier input capacitance
C_m	microphone capacitance
C_p	parasitic capacitance
d	piezoelectric constant
$d(r)$	diaphragm deflection
$d(0)$	diaphragm center deflection
d_0	un-deflected distance between the diaphragm and the back-plate
D	dielectric displacement
E	electric field / Young's modulus
F	frequency
f_n	natural resonance frequency (Hz)
f_m	mounted resonance frequency (Hz)
f_{res}	resonance frequency of the diaphragm
F	force
F_e	harmonic excitation force
F_{el}	electrostatic force
H	thickness of the diaphragm
J	imaginary
k	spring constant or equivalent stiffness of PZ material
L	octagonal diaphragm dimension
L_B	quadratic backplate dimension
m	mass
m_s	total seismic mass
m_b	accelerometer base mass
M	mass of a diaphragm
P	uniform pressure load
Q	charge
Q_a	charge source
Q_M	mechanical factor
Q_0	static charge
r	distance from the center of the diaphragm
R	radius of the diaphragm
R_B	back-plate radius
R_a	internal leakage resistance of piezoceramics
s	elastic compliance

S	strain
S_q	charge sensitivity
S_v	voltage sensitivity
S_m	mechanical sensitivity of a condenser microphone
S_e	electrical sensitivity of a condenser microphone
S_o	open-circuit sensitivity of a condenser microphone
T	stress / the tension of the diaphragm
T_c	Curie temperature
V	velocity / voltage change caused by diaphragm displacement
V	bias voltage between the back-plate and the diaphragm
V_c	collapse voltage
X	displacement
X_b	displacement of the base
X_s	displacement of the seismic mass
Y	elastic modulus
ρ	density of the diaphragm
σ	tensile stress
ε_0	vacuum permittivity ($8.85\times10^{-12}\ F/m$)
ε	permittivity
ν	Poisson's ratio
ω	excitation frequency (rad/sec)
ω_m	mounted resonance frequency (rads/sec)
ω_n	natural resonance frequency (rads/sec)
ϕ	phase angle
λ	damping coefficient
$[\ ]^T$	inverse matrix
$\dot{}$	first derivation with respect to time
$\ddot{}$	two derivation with respect to time

Contents

1 Introduction

1.1 Introduction and the background of this project

The objective of this project is to design transducers for sound and vibration better and faster by using a numerical simulation method.

Generally speaking, a transducer is a device for producing an electrical signal from another form of energy. Terminology speaking, a transducer is a device which provides a usable *output* in response to a specified *measurand*. Further, an *output* is defined as an "electrical quantity", and a *measurand* is "a physical quantity, property, or condition which is measured" [1-1].

The measurand for a transducer is the input quantity being measured by that transducer. The primary measurands, which are considered to be at the most elementary level of existence, are (1) position, (2) motion (velocity, acceleration, jerk), (3) sound, (4) light, (5) electromagnetic radiation (other than light), (6) particle radiation (other than light), (7) temperature, (8) flow, (9) force (pressure) and (10) potential difference [1-2].

This project, as implied by the thesis name, concerns the transducers for sound and vibration. These transducers have many application areas. Take microphones and accelerometers as examples. Microphones convert acoustical energy into electrical energy, which are mainly used to measure sound. Their application areas include tele-communications, broadcasting, recording of music, consumer electronics, acoustic measurements and so forth. Accelerometers convert mechanical force into electrical signal, which are primarily used to measure vibration. We can say that as long as it is necessary to measure a vibration, accelerometers have to be used. Washing machine designers use accelerometers to reduce noise. Automobile manufacturers use accelerometers to improve the structure design, reduce the noise both interior and exterior, and detect impact crash with air bags. The electronics industry uses accelerometers in photolithography operations, in chip manufacturing, and in semiconductor imaging to design and test both products and manufacturing systems. In short, the transducers for sound and vibration play a very important role in industries.

This project is financially supported by Brüel & Kjær Sound & Vibration (B & K). At the very beginning, the project was only supposed to consider accelerometers. Therefore it should not be a surprise that the background given next is mainly based on the accelerometers. But as later required, the work has also extended to the simulation of condenser microphones.

Before starting the project, B & K was in a weak competitive position in the accelerometer market because B & K was not able to respond fast to requests for customized products, and it

had limited R&D human resources for new product development. Therefore B & K was not able to exploit opportunities that appeared in the market. These opportunities could help B & K expand the product range in a focused way with reduced financial risk [1-3].

To change the situation, B & K had to be able to offer customized products faster, which is to reduce the total time to market. The most critical issues in relation to the time to market were: (1) the ability to quickly give a reliable prediction of the accelerometer performance in order to be able to get an order for the product and (2) the ability to supply and make prototypes faster. It means that total development time from initial idea to first produced prototype had to be reduced from 6 months on modifications and 2 year on totally new designs to 6 weeks and 6 months, respectively. To achieve these improvements it was necessary to optimize the design process in order to be able to give a faster prediction of the performances of the design. Furthermore it was necessary to optimize the logistic setup and the design of the production processes in order to be able to offer prototypes faster [1-3].

For the design process the goal was to be able to predict the performances of a modified accelerometer within 10 working days with reliability on the performances of about $\pm 5\%$. Furthermore to optimize the cycle time of the design phase and offer special design products even faster, a database of common components was gradually built. This would reduce the need for totally new designs and instead build new products on the basis of existing components [1-3].

B & K accelerometers used to be modeled with analytical and combined analytical-experimental methods. The analytical method is simplified to an Equivalent Electrical Circuit method that is developed on the basis of the electromechanical analogy. As a one-dimension method, the Equivalent Electrical Circuit model has limited accuracy and cannot be used for two- or three-dimension analysis because it normally ignores the coupling effect between different modes. To a certain extent, the traditional development methods cannot respond the market request fast enough with required accuracy. Therefore, the purpose of B & K financially supporting this project is to improve the development technique, and to improve the flexibility of the piezoelectric accelerometer development.

The finite element method (FEM) is one of numerical techniques. So far, it has been used in many industries successfully. The method can be flexibly used to model any arbitrary geometry and characterize any given property of a material. For the piezoelectric accelerometer modeling, besides the pure mechanical analysis, the most challenging aspect is to simulate the electrical characteristics. Therefore the FEM is chosen as a promising design tool to reduce the time to market for piezoelectric accelerometers.

In addition to accelerometers, the modeling of microphones was added to the project. The reason is that for the micro-machined silicon condenser microphone traditional development methods, which are the Equivalent Electrical Circuit and the trial-and-error, based development is too expensive and too time-consuming. Furthermore, the trade-off between the specifications cannot be obtained by the traditional design methods. Therefore the FEM is put forward once again to improve the design method.

This project considers fast response to market requests from the point of view of development method. The main purposes of the work behind this thesis are to get an improved scientific

understanding and a rough guideline for the future piezoelectric accelerometers and condenser microphones design.

The importance of this project is to introduce the advanced FEM to the design of the transducers for sound and vibration in order to get better and faster design by using computer models. The content of the project is divided into two parts, piezoelectric accelerometers and condenser microphones.

The first part presents the studies of several typical designs of piezoelectric accelerometers in detail including the analysis of the influence of variations in material properties, structure configurations and external loading. The work substantiates that the FEM can be used to simulate the piezoelectric accelerometers to the degree of precision required for R&D for prevision accelerometers. The detailed analyses of available designs can be a brief guide for the future design. The work has also improved the scientific understanding of piezoelectric accelerometers.

The second part describes the studies of condenser microphones including the circular condenser microphone and the silicon condenser microphone. The work shows that the condenser microphones can be simulated by the FEM to the degree of precision required for R&D. The work improves the scientific understanding of condenser microphones. At the same time, the work gives designers the opportunity to go to the limits of what is physically possible with condenser microphones to get the best design.

In short, the project shows that by using the numerical method the design of transducers becomes more reliable, accurate and efficient. It not only gives us better and faster design, but also modernizes the design method of transducers.

1.2 Outline of the thesis

The thesis is divided into two parts including accelerometers and microphones.

Chapter 2 is going to answer “What is a piezoelectric accelerometer?” and “What considerations need to be thought about during the design?” It introduces the piezoelectric accelerometer operation principle, sensing material, specifications and the detailed designs in order to let readers have a technical overview about piezoelectric accelerometers.
Chapter 3 is going to answer “Why do we need a new design tool?” It briefly describes the development methods for piezoelectric accelerometers. A comparison between these methods is made afterwards to show what we can expect to get from the new development method. It has demonstrated that the FEM simulation can largely extend the range of problem handled in the design phase with satisfactory accuracy.
Chapter 4 is going to answer “What kind of problems can the new design tool solve for designers?” It presents how the new method can get what we expect done.
Chapter 5 is going to answer “What benefits can be achieved by using the FEM?” In this chapter and the next one, we use “virtual prototype” to replace “FE model”. Based on the analysis on the virtual prototypes, scientific understanding of piezoelectric accelerometer designs can be improved, which is helpful for making future design.

Chapter 6 is going to answer “How can the virtual prototypes and the improved scientific understanding help designers to design?” It presents two new designs finished by using virtual prototypes. The two designs show that the FEM based design is more accurate and faster than the traditional method based design.

Chapter 7 is going to answer “What is a condenser microphone?” The construction, the operation principle and the specifications of a condenser microphone are described. The design tradeoff between the sensitivity and the resonance frequency is presented as well.
Chapter 8 is going to answer “What can be obtained with the new design tool for a circular condenser microphone?” In order to verify the simulated results, a comparison between the measured and simulated results of an existing microphone product is made. A very good agreement is achieved. After that, an optimization on the microphone backplate dimension is done. Based on the optimization, certain sensitivity can be obtained by adjusting the backplate dimension.
Chapter 9 is going to answer “What can be obtained with the new design tool for a silicon condenser microphone?” The simulation of a silicon condenser microphone with an octagonal diaphragm and a quadratic backplate is presented. A good agreement is achieved for the comparison between the simulated and the measured results. At the end of the chapter, an optimization on the backplate dimension is done.

Finally, some conclusions and suggestions for the further research are presented.

References:

1-1 “Electrical Transducer Nomenclature and Terminology”, the Instrument Society of America, the ANSI MC 6.1, 1975
1-2 James R. Carstens, “Electrical Sensors and Transducers”, Regents/Prentice Hall, 1992
1-3 Information from Dan Ulrich (former project manager).

2
Transducers for Vibration

2.1 Introduction

We have already seen that accelerometers are used to measure vibrations. Generally they can be symbolized as in Fig. 2.1. In the spring-mass system, a seismic mass m_s is suspended with a spring in a housing. When the housing is moved with an acceleration a, a relative displacement X of the seismic mass is produced by the inertial force and is detected as an electrical signal. This is the operational concept for accelerometers.

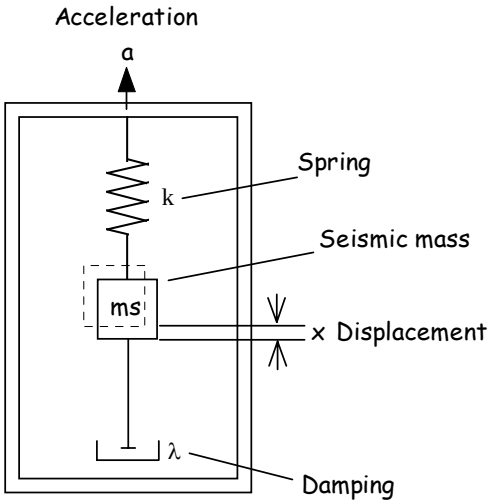

Fig. 2.1: Basic spring-mass system of an acceleration transducer.

In this chapter, the following will be presented. An overview of accelerometers is shown first. Then the sensing element of piezoelectric accelerometers, the piezoelectric material, is introduced. After that, the operation principle, specifications and different designs of piezoelectric accelerometers are described in detail.

2.2 Accelerometers

Fig. 2.1 shows that an accelerometer should be able to detect the displacement X of the seismic mass. Mainly two methods can do this: to monitor the strain induced in the spring or to detect the position of the seismic mass directly [2-2]. Piezoelectric and piezoresistive accelerometers use the strain-detecting method. Other

accelerometers, such as capacitance, magnetic, optical, inductive, reluctive accelerometer and so forth, take the position-detecting method.

Another way to classify the accelerometers is based on the function of the deflection output signal of the sensing element. If the signal can be read directly, the accelerometer is open-loop. All accelerometers mentioned above belong to this group. If the deflection signal is used to feedback in a circuit that physically drives the mass back to the equilibrium position [2-2, 2-7], the accelerometer is closed-loop. Servo accelerometer and Tunnel current accelerometer belong to this group.

Since I am interested in piezoelectric accelerometers, only this type accelerometer is going to be introduced in detail. As for other accelerometers, information can be found from many handbooks and articles, such as [2-1, 3, 4, 6, 9, 14, 22, 23, 36, 39], etc. A brief comparison between different accelerometers is given in Table 2.1.

The term *piezoelectric* comes from the Greek *piezein* which means to press and, for a time, the phenomenon was referred to as *pressure electricity* [2-1]. In fact, piezoelectric accelerometers are among the most common electromechanical transducers available. They take advantage of a material property that couples the mechanical and electrical fields. It means that a mechanical stress is accompanied by the establishment of an electrical field, and the application of an electrical field produces a strain on the material. The electromechanical coupling in piezoelectric accelerometers is fundamentally linear. This means that there is no need to apply a mechanical or electrical bias to the material in order to obtain the linear operation. In principle, piezoelectric transducers can compete with all other electromechanical transducers, including electromagnetic motors and generators. In practice, piezoelectric accelerometers are limited to devices involving only very small mechanical displacements and small amounts of electrical charge per cycle [2-1].

Fig. 2.2 shows the simplified mechanical part of Brüel & Kjær DeltaShear® accelerometer [2-16]. The active elements of the accelerometer are the piezoelectric elements. They act as springs connecting the base of the accelerometer to the seismic masses via the rigid center post.

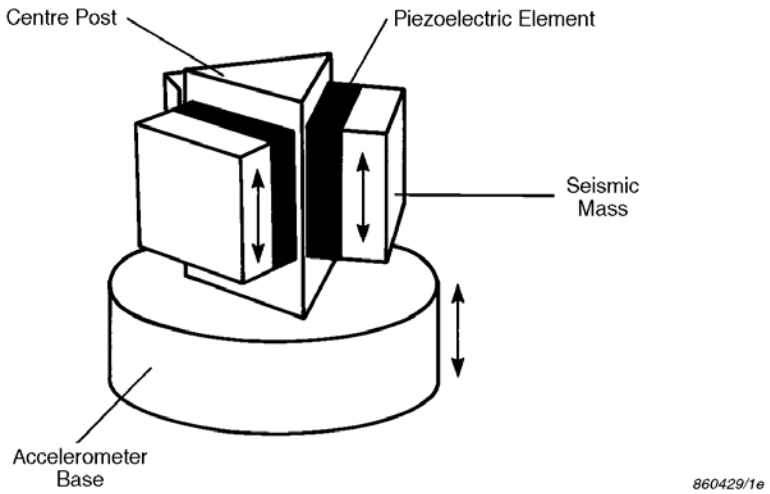

Fig. 2.2: Schematic of Brüel & Kjær Delta Shear® piezoelectric accelerometer.

The movement of the seismic masses created by an acceleration produces stress on the piezoelectric elements. Because of the piezoelectric effect, the piezoelectric elements induce some charge on their surfaces. The charge is proportional to the applied stress. As the seismic masses are constant, the charge produced by the elements is proportional to the acceleration of the seismic masses. Over a wide frequency range, the magnitude and phase of the acceleration acting on the seismic masses are the same as those on the base. Consequently the output of the accelerometer is proportional to the acceleration of the base. Therefore, the output is also proportional to the acceleration of the surface on which the accelerometer is mounted.

Table 2.1: Comparison between accelerometers.

	Inductive acc.	**Reluctive acc.**	**Potentio-metric acc.**	**Vibrating-wire acc.**	**Resonant acc.**	**Servo acc.**	**Tunnel current acc.**
Sensing element	Varied inductance	Inductance bridge	Voltage divider rule	Tension of a wire	Resonant frequency shift	Capacitive	Tunnel current effect
Frequency range	Wide	Medium	Narrow	Medium	Narrow	Low	
Accuracy	High	Medium	High	high	high	High	High
Robustness		Medium	Fragile	Medium	Medium	Fragile	
Cost	Low	High	Low	High	Low	High	
Application area	Large dynamic range, high temperature	High temperature, high-nuclear-radiation area	Slow varying acceleration			Inertial guideline systems	
Advantage	High linearity		High output signal		Continuous function test		
Disadvantage	Limited motion	High frequency	Damping needed	Sensitive to temperature,	Sensitive to stress		Not commercially
DC-detection			Yes		Yes	Yes	

	Piezo-electric acc.	Piezo-resistive acc.	Capacitance acc.	Magnetic acc.	Optical acc.
Sensing element	Piezoelectirc material	Piezo-resistive element	"Capacitor"	Magneto-elastic amorphons material	Light modulating agent
Frequency range	Wide	Wide	Wide	Medium	Wide
Accuracy	High/medium	Medium	High	Medium	High
Robustness	Very robust	Very robust	Medium	Medium	Medium
Cost	Medium low	Low	High	High	High
Application area	Vibration analysis and machine vibration	Shock	Human vibration, high temperature application	Machine vibration, no-contact	No-contact, electro-magnetic environment
Advantage	High linearity, high dynamic range, good temperature	Low output impedance	Simple external signal conditioning	The contactless sensing	Light weight, electrical isolation, no spark and fire
Disadvantage	Low output signal, high	Needing external	Sensitive to interference	Large viscous damping	Complex packaging
DC-detection	No	Yes	Yes	Yes	Yes

2.3 Piezoelectric materials

Piezoelectricity is the ability of certain crystalline materials to develop an electrical charge proportional to a mechanical stress [2-24]. Such materials are called piezoelectric materials. It was discovered by J. and P. Curie in 1880. Quartz and Rochelle salt are the first known piezoelectric materials. In 1947, Gray discovered a new piezoelectric material called barium titanate. The piezoelectric effect in poled barium titanate is substantially higher in magnitude than for the previously known materials. A strong piezoelectric effect was discovered in lead zirconate titanate (PZT) by Jaffe in the early of 1950s [2-37] and this material has remained the preferred piezoelectric material since its discovery.

2.3.1 Definitions

Ferroelectricity [2-43]

A ferroelectric crystal is defined as a crystal which exhibits a spontaneous electric dipole moment; in other words, a crystal for which, even in the absence of an applied electric field

the center of positive charge does not coincide with the center of negative charge. All ferroelectrics will be piezoelectric, but not all piezoelectrics will be ferroelectric (e.g., quartz). The crystals, such as tourmaline, which develop an observable spontaneous electric moment only on heating are called pyroelectric, while crystals with a lower coercive force, such that the direction of the spontaneous moment can be altered by an electric field, are called ferroelectric.

Polarity
Piezoelectric material is divided into two groups. Group one has the piezoelectric crystal quartz. Group two has the piezoelectric ceramic PZT and polyvinylidene fluoride (PVDF). In fact, a ceramic is an agglomeration of small crystals which are fitted together randomly. Therefore, even though the individual crystals might be strongly piezoelectric, a ceramic of an ordinary piezoelectric material does not exhibit a piezoelectric effect because the effects from the individual crystals cancel each other. To make the ceramic piezoelectric, an electrical field must be applied. Because of the ferroelectric effects, the polar axes of the crystallites in the ceramic can be switched to those directions which are nearest to that of the electrical field. This is called "poling" treatment [2-24, 30]. In the following description, the "poling" or "polarity" will be used.

Curie Point
All ferroelectric substances have a definite temperature of transition above which the phenomenon of ferroelectricity disappears. This temperature is called the "Curie Point" [2-32].

Mechanical Factor Q_M [2-27]
The mechanical factor Q_M is the ratio of the reactance to the resistance in the series equivalent circuit representing the piezoelectric resonator. The Q_M factor is also related to the sharpness of the resonance frequency. It can be expressed as

$$Q_M = \frac{f_a^2}{2\pi f_r Z_m C^T (f_a^2 - f_r^2)} \tag{2.1}$$

where f_a is the anti-resonance frequency, f_r is the resonance frequency, Z_m is the minimum impedance at f_r, C is the capacitance, and the superscript T denotes that all stresses on material are constant or no external forces.

It can be expressed as following as well.

$$Q_M = \frac{f_r}{f_1 - f_2} \tag{2.2}$$

where f_1 and f_2 are –3dB points from the resonance frequency f_r.

2.3.2 The piezoelectric effect in piezoelectric materials
For ordinary solids, a stress T only causes a proportional strain S, related by an elastic modulus, $T = Y \cdot S$. But for piezoelectric materials, the applied stress also induces an electrical charge as an additional creation because of piezoelectric effect [2-1, 24, 25, 28, 29].

The piezoelectric effect can be illustrated with Fig. 2.3 in a cylinder of piezoelectric ceramic.

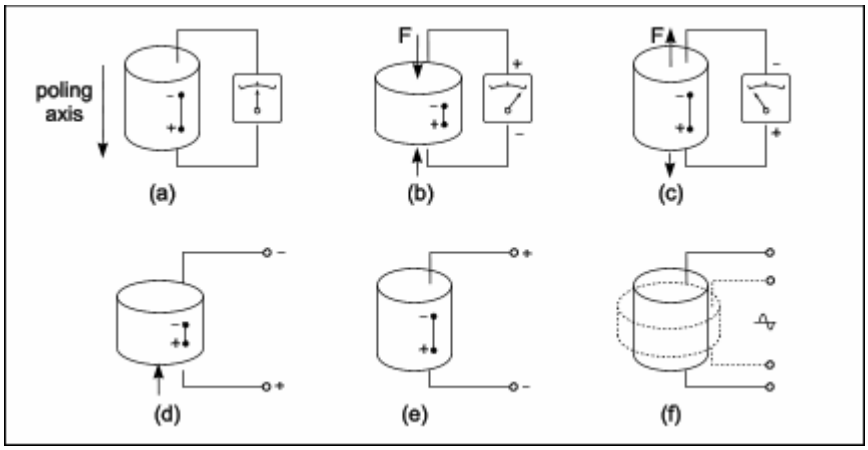

Fig. 2.3: The piezoelectric effect in a cylinder of piezoelectric ceramic.

Fig. 2.3(a) shows the neutral state. Fig. 2.3(b) and (c) show that when a mechanical stress is applied to the cylinder of piezoelectric ceramic, correspondent to the poling axis, it can produce electrical charge which is proportional to the stress, and it is of opposite sign for compression and tension. In terms of dielectric displacement D (charge Q per unit area) and stress T, we may write

$$D = Q/A = d \cdot T \tag{2.3}$$

where d expressed in coulombs/Newton.

Fig. 2.3(d) and (e) show that when a field E is applied to a piezoelectric material, a proportional strain S is caused, expansion or contraction depending on polarity.

$$S = d \cdot E \tag{2.4}$$

where d expressed in (meter$\times$Volt/meter).

Fig. 2.3(f) shows that the mechanical deformation will expand and contract sinusoidally when a sinusoidal electrical field is applied. It is also based on the eqn. (2.4).

For eqns. (2.3) and (2.4), the proportionality constant is the piezoelectric constant d which is numerically identical for both.

$$d = D/T = S/E \tag{2.5}$$

A high piezoelectric constant d is desirable for materials intended to develop motion or vibration, such as piezoelectric actuators.

What was mentioned above can be generalized as the equations of state of the piezoelectric effect as [2-1, 24, 25]:

$$D = d \cdot T + \varepsilon^T \cdot E \tag{2.6}$$

$$S = s^E \cdot T + d \cdot E \tag{2.7}$$

Eqn. (2.6) describes the direct piezoelectric effect while eqn. (2.7) the converse. It is a characteristic consequence of the piezoelectric effect that the elastic and dielectric constants are affected by electrical and elastic boundary conditions respectively.

For the symmetry of piezoelectric ceramics, the general eqns. (2.6) and (2.7) are replaced by the specific set of equations [2-24, 31, 34, 35].

Direct effect:

$$\begin{aligned} D_1 &= \varepsilon_1 \cdot E_1 + d_{15} \cdot T_5 \\ D_2 &= \varepsilon_1 \cdot E_2 + d_{15} \cdot T_4 \\ D_3 &= \varepsilon_3 \cdot E_3 + d_{31} \cdot (T_1 + T_2) + d_{33} \cdot T_3 \end{aligned} \tag{2.8}$$

Converse effect:

$$\begin{aligned} S_1 &= s_{11}^E \cdot T_1 + s_{12}^E \cdot T_2 + s_{13}^E \cdot T_3 + d_{31} \cdot E_3 \\ S_2 &= s_{11}^E \cdot T_2 + s_{12}^E \cdot T_1 + s_{13}^E \cdot T_3 + d_{31} \cdot E_3 \\ S_3 &= s_{13}^E \cdot (T_1 + T_2) + s_{33}^E \cdot T_3 + d_{33} \cdot E_3 \\ S_4 &= s_{44}^E \cdot T_4 + d_{15} \cdot E_2 \\ S_5 &= s_{44}^E \cdot T_5 + d_{15} \cdot E_1 \\ S_6 &= s_{66} \cdot T_6 \end{aligned} \tag{2.9}$$

The subscripts shown on the left hand side of eqns. (2.8) and (2.9) can be illustrated with Fig. 2.4 [2-31].

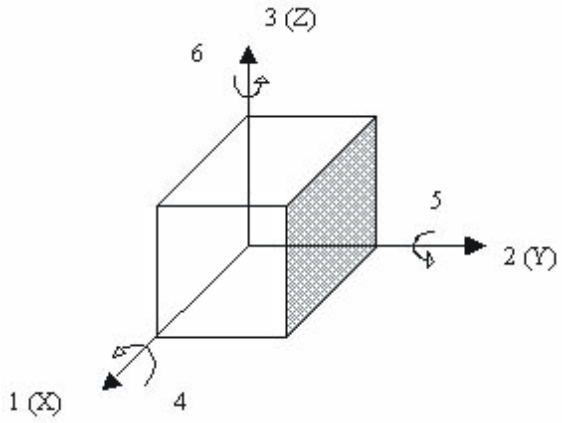

Fig. 2.4: The coordinate system of piezoelectric materials.

The subscript 3 refers to the poling axis, 1 and 2 refer to an arbitrarily chosen orthogonal axes in the plane normal to 3. Subscripts 4, 5 and 6 refer to shear stress and strain in planes normal to the 1, 2 and 3 axes, respectively. A shear strain, such as S_4, is a measure of the change of angle between the two initially orthogonal axes in the plane perpendicular to axis 1.

Conventionally, the first subscript of the d constant gives the "electrical" direction while the second gives the component of the mechanical deformation or stress.

The permitivities ε_1 and ε_3 give the electrical displacement while the stress remains constant, usually zero. They are the free permitivities sometimes indicated by the superscript T.

Similarly, the elastic compliances s_{11}, … denote the interaction of a strain and a stress with the condition of constant field. They are the "short-circuit" compliances marked, if necessary, by the superscript E, which indicates constant (usually zero) field. Moreover, each elastic coefficient s_{11}, … relates to application of a single stress component while the other are kept fixed (condition of no lateral restraint). Within this limitation, stress and strain are interchangeable, $s_{31} = s_{13}$. Rigorously the permittivity ε is also a tensor and should have two subscripts.

2.3.3 Piezoelectric materials

Due to the fact that most piezoelectric accelerometers use quartz or PZT as the sensing element, this section only focuses on the two materials. The comparison between them is given in Table 2.2 [2-29, 33]. As for other piezoelectric materials, information can be found from [2-25, 27, 31, 38].

Table 2.2: The comparison between quartz crystal and polycrystalline ceramic.

Quartz crystal	Polycrystalline ceramic
Naturally piezoelectric material	Artificially polarized, man-made material
Exhibits excellent long term stability	Less stable than quartz crystal
Must be cut along certain crystallographic directions	Unlimited availability of sizes and shapes
High voltage sensitivity	High charge sensitivity
Materials available to operate at 315°C	Materials available to operate at 540°C
Non-pyroelectric	Output due to thermal transients
Low temperature coefficient	Characteristics vary with temperature

Natural piezoelectric quartz [2-24, 25, 26] has no tendency to relax to an alternative state, therefore accelerometers using quartz as piezoelectric element have long term stability and repeatability. Piezoceramics are easy to fabricate into a variety of shapes and sizes while quartz must be cut along certain crystallographic directions, which limits the possible geometrical shapes.

Since quartz has a low capacitance value, the voltage sensitivity is high compared to most ceramic materials. This feature makes it ideal for voltage amplified systems. Compared to quartz, piezoceramics have higher charge sensitivity.

As for the thermal response of quartz versus piezoceramics, both of them give an output during a temperature change named pyroelectric effect. Though the pyroelectric effect of quartz is much lower than that of piezoceramics, when the materials are not mounted within a sensor housing, the difference becomes insignificant when they are mounted within a sensor, which means they are isolated from fast thermal transients.

A very important feature of piezoelectric materials is that they can only measure dynamic or changing events. The reason is that static events will cause an initial output, this signal will slowly decay (or drain away) based on the internal leakage resistance of piezoelectric material and leakage in the connected measuring equipment. Therefore, piezoelectric accelerometers are not able to measure a continuous static event, such as, inertial guidance, barometric pressure or weight measurement.

Piezoceramic materials Type Pz23 and Pz27 from Ferroperm used in the project are lead zirconate titanate [2-27]. They are characterized by relatively high Curie Point (>350°C), low mechanical Q_M factor and high electrical resistivity at elevated temperatures. Pz27 has higher dielectric constant, higher charge coefficients and higher electromechanical coupling coefficients than Pz23. But it has lower temperature stability than Pz23. Another piezoceramic from Ferroperm is Type Pz45, which is bismuth titanate. It has very high Curie Point (>500°C) and working temperature of up to 400°C. It has low dielectric constant, low dielectric loss and high temperature stability. The used properties of Pz23, Pz27 and Pz45 are listed in Table 2.3 [2-27].

Table 2.3: Material data for standard test specimens.
(Data are measured at 25°C and 24 hours after poling.)

	Symbol		Pz23	Pz27	Pz45
Curie temperature	$T_c >$	(°C)	350	350	500
Recommended temperature	<	(°C)	250	250	400
Piezoelectric constant	$-d_{31}$	(10^{-12}C/N)	130	170	3
	d_{33}		330	425	16
	d_{15}		335	500	
Dielectric constant	$\varepsilon_{11}^T / \varepsilon_o$		1730	1730	
	$\varepsilon_{33}^T / \varepsilon_o$		1700	1700	
Density	ρ	(10^3 kg/m^3)	7.70	7.70	7.15
Elastic compliance	s_{11}^E	(10^{-12} m^2/N)	15	17	8
	s_{33}^E		19	23	9
Poisson's ratio	σ^E		0.39	0.39	0.25
Mechanical Quality factor	Q_M		100	80	>500

Since the piezoelectric material is the active element of piezoelectric accelerometers, the principle of piezoelectric accelerometers depends on the element configuration. Acting as true precision springs, the different element configurations shown in Fig. 2.5 offer various advantages and disadvantages [2-33].

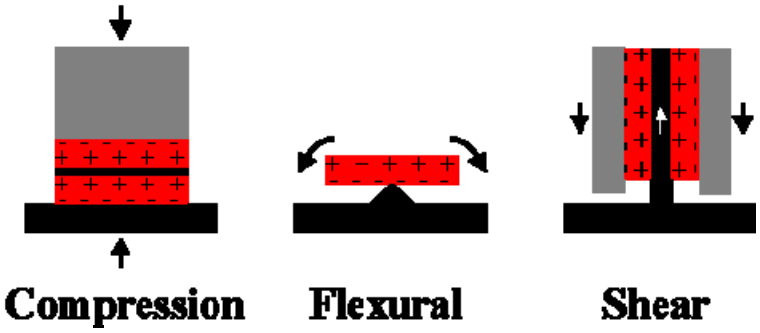

Fig. 2.5: The different element configurations.

The high rigidity of the compression configuration makes it useful for implementation in high frequency pressure and force transducers, but this design is sensitive to thermal transients and base strain. The simplicity of flexural configuration is offset by its narrow frequency range and low over-shock survivability. The shear configuration can offer a well balanced blend of wide frequency range, low off axis sensitivity, low sensitivity to base strain and low sensitivity to thermal inputs.

2.4 The specifications of piezoelectric accelerometers

The following specifications need to be considered during design. The order denotes the priority for the general application accelerometer.

2.4.1 Design principle

According to Fig. 2.5, there are three piezoelectric element configurations, compression, flexural and shear. Correspondingly there are three accelerometer design principles. The last paragraph of the last section mentions the features of each design principle. The next section will introduce all available design for each principle. The detail analysis will be shown in Chapter 5.

From a design point of view, the frequency range and the dynamic range will influence the choice of the design principle most.

2.4.2 Number of axis

The number axes an accelerometer can have can be one, two and three. The most common is one axis. By putting three units into one housing, we can have a two axes accelerometer if we use two of the three units or have a triaxial accelerometer if we use all three units. The newest triaxial piezoelectric accelerometer uses the advanced OrthoShear design which only has one unit. The design can be changed to two axes by deleting the circuit for the third axis of the preamplifier.

From a design point of view, the traditional triaxial accelerometer takes the same principle as the one-axis. The newest triaxial accelerometer has more complicated construction, but as one unit gives all three axes it has fewer parts.

Generally speaking, the number of the accelerometer axes designed is mainly determined by the complexity of the tested structure and the application.

2.4.3 Weight and size

When an accelerometer is mounted on a measured object, the added mass of the accelerometer may produce substantial changes in the vibratory response of the object. This is called mass loading effects. The resonance frequency of the measured object will be changed according to the ratio between the accelerometer weight and the object weight. The frequency change can be expressed as

$$\frac{f_n - \Delta f_n}{f_n} = \sqrt{\frac{m}{m + \Delta m}} \tag{2.10}$$

Detailed explanation can be found from [2-41]. It will not be repeated here.

From a design point of view, the lighter and smaller the accelerometer, the more accurate the measurement. Another consideration is that the center of gravity of an accelerometer should be as close as possible to the mounting surface.

2.4.4 Sensitivity

A piezoelectric element acts as a capacitor C_a in parallel with a very high internal leakage resistance R_a, which can be ignored from a practical point of view. Consequently, a piezoelectric accelerometer may be treated as either an ideal charge source, Q_a in parallel with C_a and the cable capacitance C_c or a voltage source V_a in series with C_a and loaded by C_c, as shown in Fig. 2.6 [2-5].

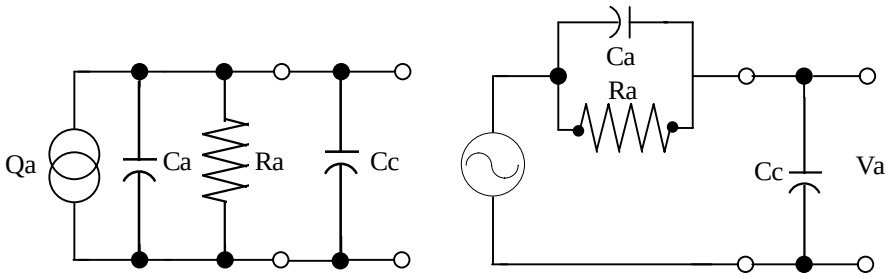

(a) Charge Equivalent. (b) Voltage Equivalent.

Fig. 2.6: The equivalent circuit of a piezoelectric element.

In other words, the sensitivity of an accelerometer can be expressed as charge sensitivity or voltage sensitivity defined as the resultant charge Q_a, or the load-dependent signal V_a appearing at the output, divided by the acceleration a as following:

$$\text{Charge sensitivity: } S_q = \frac{Q_a}{a} \tag{2.11}$$

$$\text{Voltage sensitivity: } S_v = \frac{V_a}{a} \tag{2.12}$$

Fig. 2.6(b) shows that the voltage produced by the accelerometer is divided between the accelerometer capacitance C_a and the cable capacitance C_c. It means that a change in the cable capacitance C_c caused either by a different type of cable or by a change in the length of cable will cause a change in the voltage sensitivity. Therefore, we use charge sensitivity to describe the accelerometer sensitivity in this thesis.

Refer to Fig. 2.4 and Fig. 2.7 to illustrate the sensitivity. Assume the piezoelectric elements are polarized along Y-direction. Forces are applied on the planes normal to 2 axis, which is T_5.

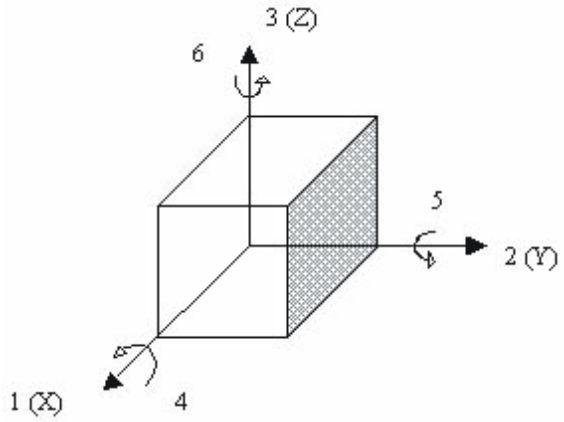

Fig. 2.7: The coordinate system of piezoelectric materials.

Rewrite eqn. (2.8), we have

$$D_1 = d_{15} \cdot T_5 + \varepsilon_1^E \cdot E_1 \tag{2.13}$$

When the charge sensitivity is considered, the electrical field strength $E = 0$, eqn. (2.13) can be simplified to

$$D = d_{15} \cdot T_5 \tag{2.14}$$

As shown in Fig. 2.2, subject to an acceleration in the axial direction, the stress acted on the ceramic element produced by the seismic mass movement is

$$T = m_s \cdot a / A \tag{2.15}$$

where m_s is the sum of the seismic mass and half of the sensing elements mass, and *A* is the area of the plane facing the seismic mass.

Therefore, the charge sensitivity can be expressed as

$$S_q = Q / a = D \cdot A / a = d_{15} \cdot T \cdot A / a = d_{15} \cdot m_s \tag{2.16}$$

The sensitivity expressed by eqn. (2.16) is for a shear design. For a compression design, the sensitivity is

$$S_q = d_{33} \cdot m_s \tag{2.17}$$

If we consider a damped single degree of freedom model, the output at resonance $S_q(f_0)$ is given by [2-40]

$$S_q(f_0) = \frac{S_q(f) \cdot Q_M}{\sqrt{1 + 1/(2Q_M^2)}} \tag{2.18}$$

where $S_q(f)$ is the charge sensitivity at a frequency *f*, well below the resonance. [2-27] shows that for Pz23 Q_M=100, for Pz27 Q_M=80. Therefore, for the most common used ceramic we have

$$\frac{S_q(f_0)}{S_q(f)} \approx Q_M \approx 40dB \tag{2.19}$$

From a design point of view, in order to increase the sensitivity, we can increase the seismic mass and use a more sensitive ceramic. All these considerations are made for charge accelerometer, which means preamplifier is not included.

2.4.5 Transverse sensitivity

Transverse output is the output to an acceleration perpendicular to the accelerometer ideal sensitive axis [2-10, 16]. The *transverse sensitivity* is defined as the ratio of the maximum transverse output to the magnitude of transverse input, divided by the sensitivity in the ideal direction [2-18].

In fact the transverse sensitivity of an ideal accelerometer should be zero, but practically it cannot be treated as not existing. Fig. 2.8 explains the reason. Manufacturing tolerances and

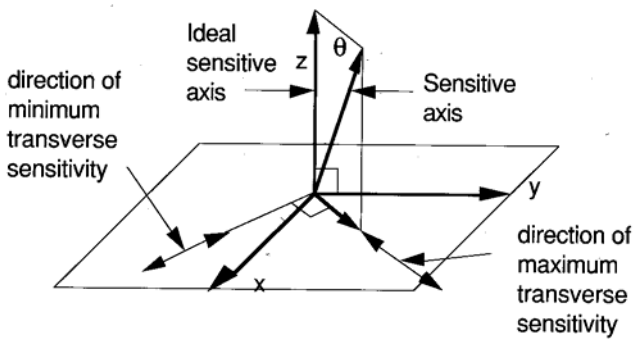

Fig. 2.8: The transverse sensitivity illustration.

sensor element variations tilt the sensitivity axis by an angle θ, placing a component with magnitude equal to $sin(\theta)$ in the transverse plane. [2-18] presents that only 1° misalignment creates a transverse component 1.74% of the magnitude of the sensitive axis. The transverse sensitivity is described as a percentage of the main axis sensitivity. There is no theoretical equation to estimate the number.

From a design point of view, in order to reduce the transverse sensitivity, we should make the design more symmetric around the ideal axis.

2.4.6 Dynamic range

The *dynamic range* is defined as the difference between the maximum sinusoidal excitation level to the minimum detectable level. The lowest level is determined by the mechanical-thermal noise if we consider an accelerometer without amplifier. Setting the signal-to-noise ratio equal to unity, the detectable level *a* can be expressed as [2-42]

$$a = \sqrt{\frac{4k_B T\omega_0}{mQ}} \tag{2.20}$$

where k_B is the Boltzmann constant (1.38×10^{-23} JK^{-1}), T the absolute temperature, ω_0 the resonance frequency, m the seismic mass and Q the quality factor of the mechanical system. Therefore in order to low the detectable level, we should increase the seismic mass (meaning increase the sensitivity and decrease the resonance frequency), and increase the Q (determined by the whole system).

From a design point of view, in order to enlarge the dynamic range, we should increase the robustness of the construction to increase the high limit. Hard ceramic as Pz45 can go to a higher level than soft one as Pz27, but has much lower sensitivity. We should increase the seismic mass and choose the ceramic with high Q to lower the minimum detectable level.

2.4.7 Capacitance

The *capacitance* of an accelerometer is defined as the ratio of its charge sensitivity to its voltage sensitivity. It is determined by the ceramic material properties and the geometry (area and the thickness). According to eqn. (2.16) and (2.17), we know that the charge sensitivity does not have any relationship with the capacitance. Therefore based on $V \cdot C = Q$, it can be

seen that the lower the capacitance, the larger the voltage output. At the same time, the lower the capacitance, the lower the noise produced by the ceramic.

From a design point of view, a compromise has to be made between the voltage output and the mounted resonance frequency. In order to increase the voltage output, the capacitance should be as small as possible. It means that the ceramic should be as thin as possible. But the thin ceramic will reduce the stiffness, which means reduce the mounted resonance frequency. Therefore a compromise has to be made carefully.

2.4.8 Frequency

Frequency includes *natural resonance frequency*, *mounted resonance frequency*, *transverse resonance frequency*, *usable frequency range and phase shift* [2-16].

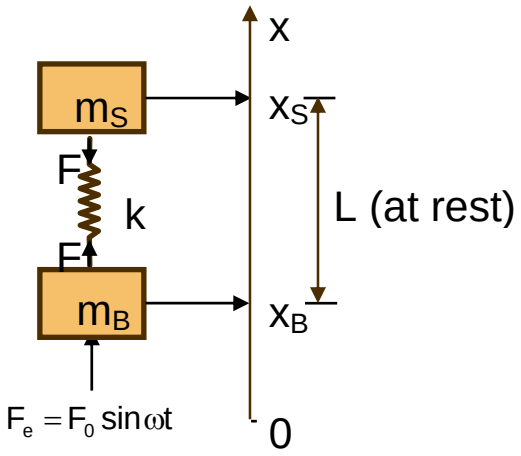

Fig. 2.9: Simplified model of a piezoelectric accelerometer.

If we consider an accelerometer as an undamped, single degree of freedom, harmonically driven mass-spring system, it can be schematically represented as shown in Fig. 2.9. The following equations describe the forces present in the system.

$$F = k \cdot (X_s - X_b - L) \quad \text{(spring force)} \tag{2.21}$$

$$m_b \cdot \ddot{X}_b = F + F_e \quad \text{(force on the base)} \tag{2.22}$$

$$m_s \cdot \ddot{X}_s = -F \quad \text{(force on the seismic mass)} \tag{2.23}$$

The motion equation for the system is

$$\ddot{X}_s - \ddot{X}_b = -\frac{F}{m_s} - \frac{F + F_e}{m_b} = -\frac{k}{\mu} \cdot (X_s - X_B - L) - \frac{F_e}{m_b} \tag{2.24}$$

or:

$$\mu \cdot \ddot{r} = -k \cdot r - \frac{\mu}{m_b} \cdot F_0 \cdot \sin \omega t \tag{2.25}$$

where

$$\frac{1}{\mu}=\frac{1}{m_s}+\frac{1}{m_b}, \qquad r = X_s - X_b - L, \qquad F_e = F_0 \cdot \sin \omega t .$$

When the accelerometer is subjected to a free vibration, that is, F_e=0, then

$$\mu \cdot \ddot{r} = -k \cdot r \tag{2.26}$$

Assume that the displacement of m_s relative to m_b varies harmonically with amplitude, that is, $r = R\sin \omega t$, then

$$-\mu \cdot R \cdot \omega^2 \cdot \sin \omega t = -k \cdot R \cdot \sin \omega t \tag{2.27}$$

Therefore, the natural resonance frequency of the accelerometer, ω_n, can be written as

$$\omega_n^2 = k \cdot (\frac{1}{m_s}+\frac{1}{m_b}) \tag{2.28}$$

When the force is considered, it must be included in the analysis along with the natural resonance frequency, ω_n defined as eqn. (2.28). Eqn. (2.25) can be rewritten as

$$\ddot{r} + \omega_n^2 \cdot r + \frac{1}{m_b} \cdot F_0 \sin \omega t = 0 \tag{2.29}$$

Assume again that the displacements of the masses vary sinusoidally, then

$$-\omega^2 \cdot R \cdot \sin \omega t + \omega_n^2 \cdot R \cdot \sin \omega t + \frac{F_0}{m_b} \sin \omega t = 0 \tag{2.30}$$

Therefore,

$$R = -\frac{F_0}{m_b(\omega_n^2 - \omega^2)} \tag{2.31}$$

At frequencies well below the natural resonance frequency of the accelerometer $(\omega << \omega_n)$ the displacement, now called R_l, is expressed by

$$R_l = -\frac{F_0}{m_b \omega_n^2} \tag{2.32}$$

The ratio of the displacement at low frequency R_l to the displacement at high frequency R can be denoted as follows

$$A = \frac{R}{R_l} = \frac{-\frac{F_0}{m_b(\omega_n^2 - \omega^2)}}{-\frac{F_0}{m_b\omega_n^2}} = \frac{1}{1-(\frac{\omega}{\omega_n})^2} \tag{2.33}$$

This important result A shows that the displacement between the base and the seismic masses increases when the forcing frequency becomes comparable to the natural frequency of the accelerometer. Consequently the force on the piezoelectric elements and the electrical output from the accelerometer also increase.

Natural resonance frequency is the frequency at which the accelerometer's active sensing element will go into resonance and respond with the maximum movement for a specific applied acceleration in its undamped state [2-16]. According to eqn. (2.28), it can be expressed as:

$$f_n = \frac{1}{2\pi}\sqrt{k \cdot (\frac{1}{m_s} + \frac{1}{m_b})} \tag{2.34}$$

If the accelerometer is mounted with perfect rigidity onto a structure that is much heavier than the total weight of the accelerometer, that is, m_b is much larger than m_s, the resonance frequency will be lower. If the measured structure is infinitely heavy, in other words, $m_b \to \infty$, then

$$f_m = \frac{1}{2\pi}\sqrt{k \cdot \frac{1}{m_s}} \tag{2.35}$$

This is the *mounted resonance frequency*.

It is clear that the accelerometer resonance frequency can be improved by reducing the seismic mass and/or increasing the equivalent stiffness of the piezoelectric material.

Eqns. (2.34) and (2.35) show that when an accelerometer is mounted on a measured object, the resonance frequency determined by the mass of the accelerometer package and the spring constant of the adhesive layer might cause error in measurements. When a small mass loading effect and a wide frequency range are required, a small size and small mass of the accelerometer are essential factors. These are mentioned in 2.4.1. A general rule to avoid the mass loading effect is to ensure that the accelerometer mass is less than one tenth of the mass of the tested structure.

Fig. 2.10 shows the relative change in electrical output from an accelerometer [2-16]. Piezoelectric accelerometers have low-frequency and high-frequency limits. (1) The *high-frequency limit* is because an accelerometer responds to vibration whose frequency is less than the natural frequency of the transducer. The limit is determined by the mounted resonance frequency and the damping of the transducer. Practically the limited frequency is one third of the mounted resonance frequency. An attempt to use such a transducer beyond this frequency limit may result in distortion of the signal. The high-frequency limit for slightly damped vibration-measuring instrument is important because these instruments exaggerate the small amounts of harmonic content that may be contained in the motion, even when the operating frequency is well within the usable frequency range of the instrument. (2) The *low-frequency limit* is normally determined by the leakage time constant of built-in or external charge amplifier. If the leakage time constant is long enough, the limited low frequency of an amplifier can be 2×10^{-6} Hz [2-15]. In this case, the lower usable frequency is mainly limited by the internal leakage resistance of piezoelectric materials. In general, a sensing element using external power or a carrier voltage does not have a lower frequency limit, whereas a self-generating sensing element cannot operate at zero frequency.

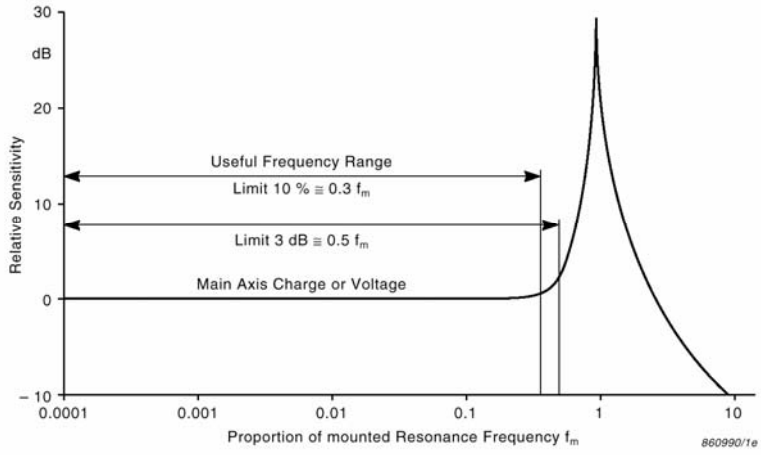

Fig. 2.10: Relative sensitivity of an accelerometer vs. frequency.

The range of frequencies over which the accelerometer is supposed to be used is only the flat portion of the response curve shown in Fig. 2.10, which is called the *usable frequency range*.

Accelerometers have many resonant modes. One of them is called the transverse mode. It is induced when the vibration is normal to the main axis. The output of the mode is not what we want. Besides this, the output signal produced by the transverse mode is normally bigger than the signal produced by other useless modes such as torsion mode. Therefore it is very important to find the *transverse resonance frequency* to avoid the accelerometer working at this particular frequency. But there is no theoretical equation to estimate the transverse resonance frequency.

Piezoelectric materials present a coupling between the mechanical and electrical forces. The *phase* shift of an accelerometer corresponds to the delay between the mechanical input and the electrical output. The relationship between the phase response and the amplitude is shown

in Fig. 2.11 [2-16]. At the resonance frequency, phase shift between the applied acceleration and the output signal is 90°.

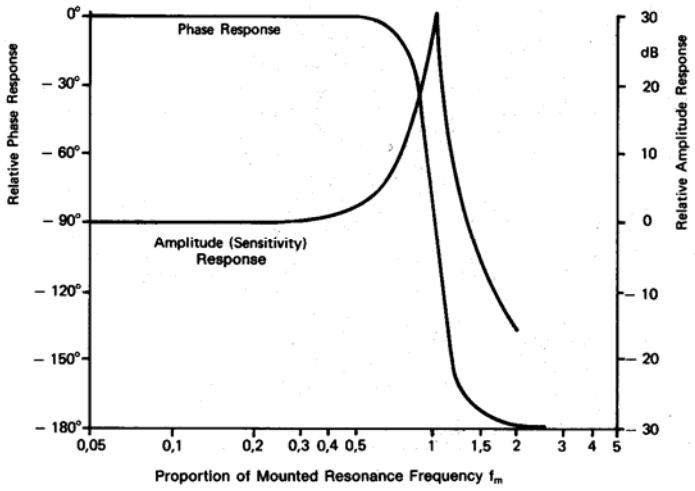

Fig. 2.11: Accelerometer amplitude and phase response.

From an application point of view, we want to increase the transverse resonance frequency to avoid the ring effect. From a design point of view, we should increase the stiffness of the part that holds the ceramic, we should keep the seismic assembly as low as possible.

If the phase is not constant at all frequencies in the operating range, the phase relationship between different frequency components of a vibration signal will be altered with respect to each other. It will result in an electrical output that is a distorted representation of the mechanical input. It is especially important when measuring transient vibrations and mechanical shocks. An undamped accelerometer measures acceleration without distortion of phase.

For the sinusoidal input of a particular frequency, the time delay is a phase angle ϕ, given by eqn. (2.36) [2-18]. $\phi/2\pi f$ is the number of seconds that the measurements lags behind the actual acceleration (if f is in Hz and ϕ is in radians).

$$\tan\phi = \frac{\left(2\lambda\frac{f}{f_n}\right)}{1-\left(\frac{f}{f_n}\right)^2} \tag{2.36}$$

where λ is the damping coefficient.

As can be recognized by comparing eqns. (2.16), (2.17) and (2.35), a high sensitivity results in a low resonance frequency. The resonance frequency limits the operational frequency range of the accelerometers. Therefore, the design must compromise between these contradictory tendencies.

2.4.9 Temperature range

All accelerometers are rated for a maximum and a minimum operating temperature limit. For the maximum temperature limit, the main reason is that the properties of the piezoelectric material, for example the capacitance and both the charge and voltage sensitivity, varies when the accelerometer is operated at temperature other than the usable range. Other components may also influence the temperature response, for example the thermal expansion of the components and the use of the weak materials such as rubber and the accelerometer connecting cable.

The properties of the ceramic material do not limit the minimum temperature limit.

The maximum temperature limit is much more important than the minimum one. From a design point of view, in order to increase the temperature range, we should pay most attention to the properties of the ceramic used. Almost all high-temperature accelerometers use Lithiumniobate or Tourmaline as sensing element. Another consideration is the material's consumption of oxygen from the ceramic. This deteriorates the insulation resistance of the ceramics. The way to solve the problem is to make a ventilation hole and/or make sure all metal components are oxidized at a temperature about the operating temperature of the accelerometer.

2.4.10 Temperature transient sensitivity

Piezoelectric accelerometers exhibit sensitivity to *temperature transients*. It is due to the pyroelectric effect and the non-uniform thermal expansion.

The pyroelectric effect is a phenomenon where piezoelectric crystals and ferroelectric materials become charged by temperature inequalities and temperature changes. In artificially polarized ceramics whose polarization is along the height direction, this charge is built up on the surfaces perpendicular to the polarization direction.

The non-uniform thermal expansion occurs when the parts of the accelerometer structure expand or contract at different rates or the accelerometer is subjected to a heat differential across its case. Both phenomenon cause stresses on the piezoelectric element and a resultant output.

The temperature transient sensitivity is of no great importance until low frequency, low level accelerations are being measured.

From a design point of view, in order to reduce the temperature transient sensitivity, a shear construction is much better than a compression construction. In a compression construction, when the vibration induced charge is picked up normal to the polarization direction, the pyroelectric charge is picked up at the same time and erroneous output results. In a shear construction, the vibration induced charge is picked up parallel to the polarization direction, therefore the pyroelectric charge will not be picked up. Another consideration is that the thermal expansion coefficient of the materials used for accelerometer components should not be very different from each other to avoid the non-uniform thermal expansion.

2.4.11 Base strain sensitivity

An accelerometer may generate a spurious output when its case is strained. Typically this occurs when the transducer mounting is not flat against the surface to which it is attached, or the surface bends much. This effect is called *base-bend sensitivity* or *strain sensitivity*.

An accelerometer with a sensing element which is tightly coupled to its base tends to exhibit large strain sensitivity. An error due to strain sensitivity is most likely to occur when the accelerometer is attached to a structure which is subject to large amounts of flexure. In such cases, it is advisable to select an accelerometer with low strain sensitivity.

From a design point of view, in order to reduce the base bending effect, the accelerometer structure should be balanced. Furthermore since a shear design construction is much more loosely coupled to its base than a compression design, the shear design has a much smaller base bending effect.

2.4.12 Maximum shock

Maximum shock is defined as the lowest shock in any axis which causes more than a 2% change in sensitivity. For sure, the bigger the shock limit, the better.

From a design point of view, the consideration has to be taken for the stiffness of the material used for the housing and the ceramic, and the linearity of the ceramic material. Take the configurations shown in Fig. 2.5 as an example, under shock the components of the shear configuration are much easier to lose connection with each other while the components of the compression configuration do not have the problem. Therefore the compression design can withstand much larger maximum shocks than other designs.

2.4.13 Humidity

Humidity may affect the characteristics of certain types of vibration instruments. The high impedance of the ceramic can be short-circuited by humidity, therefore the output goes down. Humidity can lead to an increasing noise as well. In general, a transducer which operates at a high electrical impedance is affected by humidity more than a transducer which operated at a low electrical impedance. It usually is impractical to correct the measured data for humidity effects.

From a design point of view, accelerometers that might otherwise be adversely affected by humidity can be sealed hermetically to protect them from the effects of moisture.

2.4.14 Acoustic sensitivity

High-intensity sound waves often accompany high-amplitude vibration. If the case of an accelerometer can be set into vibration by acoustic excitation, error signals may result. In general, a well-designed accelerometer will not produce a significant electrical response except at extremely high sound pressure levels. Under such circumstances, it is likely that vibration levels also will be very high, so that the error produced by the accelerometer's exposure to acoustic noise is usually not important.

From a design point of view, the effect can be reduced by making the whole structure as stiff as possible.

2.4.15 Magnetic sensitivity

When the accelerometer is used in the area with strong magnetic influence, the flux will be induced within any loop of the accelerometer structure, which results in erroneous results.
From a design point of view, we should avoid the loop, which is formed by the wire from the connector to the ground potential via the ceramic. Materials which conduct magnetic flux such as Covar should also be avoided.

2.4.16 Housing and base material

There are several materials that usually are used to make the housing and base, for example stainless steel, Beryllium, Titanium and aluminum. The key properties of the materials are shown in Table 2.4.

Table 2.4: The properties of the materials used for housing and base.

Material	Density (kg/m^3)	Young's modulus (10^{10} N/m^2)	Poisson's ratio	Relative price
Stainless steel	7860.	20.	0.30	30 DKr/kg
Beryllium	1870	30.9	0.05	1.8×10^5 DKr/kg
Titanium	4500.	9.0	0.32	300 DKr/kg
Aluminum	2700	7.1	0.32	20 DKr/kg

From a design point of view, if we want to increase the stiffness of the structure, the stainless steel is a good choice though the weight will be high. Aluminum is much lighter but does not have the stiffness. Generally speaking Titanium is a material whose properties are in the between of those of stainless steel and the aluminum. It is suitable for making the housing and base but has a higher cost. Beryllium has the best material properties with the highest stiffness and the lowest weight except it has a very high price. But it should be avoided because the dust is poisonous and difficult to work with.

2.4.17 Connector

There are top and side *connectors*. The function of the connector is to connect the output signal to the cable. It also makes it convenient to change the cable. The cable does add mass and can be a local resonator to the housing, both of which can adversely effect the performance of the accelerometer.

From a design point of view, the connector should be as small as possible, and be disconnectable by hand.

2.4.18 Mounting

There are different kinds of *mountings* used; Stud Mounting, Wax Mounting, Clip Mounting, Magnet Mounting, Self-Adhesive Mounting Discs, Adhesive Mounting and Probes and so forth. The selection of correct mounting can significantly affect the measurement accuracy and resonance frequency.

From a design point of view, we should make a flat, even mounting surface to increase the coupling between the bottom of the accelerometer and the tested object.

Table 2.5 shows the relationships between the specifications and the parameters described by eqns. (2.10), (2.16), (2.17) and (2.34). + means that the specification is proportional to the parameter. – means that the specification is inversely proportional to the parameter. The number denotes the order.

Table 2.5: The relationship between parameters.

	k	M_s	d_{15}
S	-1	+1	+1
f_{res}	+ ½	- ½	
Mass load		+ 1/2	

k is the stiffness of the whole system. It is determined by the detail structure, primarily by the stiffness of the piezoelectric material. Table 2.2 tells us that Pz27 has higher piezoelectric constant d_{15} than Pz23, Pz27 also has higher elastic compliance than Pz23. It means that when we choose piezoelectric material, we have to remember that a compromise must be made between the piezoelectric constant and the elastic compliance.

As for the seismic mass, Table 2.4 shows clearly that the bigger the seismic mass, the higher the sensitivity, the lower the resonance frequency, the more serious the mass loading effect.

In short, when a designer designs an accelerometer, no matter with which kind of sensing method, the considerations should be kept in mind. They are

(1) a right principle according to the requirement for the frequency range and the dynamic range
(2) a right axis number according to the application
(3) light weight and small size
(4) a carefully made compromise between the sensitivity and the frequency range
(5) small transverse sensitivity by making the design more symmetric around the main axis
(6) large dynamic range by choosing right ceramic material
(7) right capacitance based on a carefully made compromise between the charge output and the noise
(8) large temperature range by choosing right ceramic material
(9) small temperature transient sensitivity by taking shear design and by using materials having similar expansion coefficient
(10) small base strain sensitivity by designing a balance structure having loose coupling to its base, such as shear design
(11) large maximum shock by designing a stiff structure
(12) small humidity effect by sealing hermetically the accelerometer
(13) small acoustic sensitivity by designing a stiff structure
(14) small magnetic sensitivity by avoiding the loop forming by the wire and by avoiding the use of material that conducts magnetic flux
(15) right material for the housing and the base according to the requirement, Titanium is recommended
(16) small and easy used connector
(17) a flat, even mounting surface to make the mounting easier

Some extremes of piezoelectric accelerometers are shown in Table 2.6 [2-36].

Table 2.6: Some piezoelectric accelerometers with extreme specifications.

Specification	Type	Note	
Weight & Size	22 *	Without amplifier	0.14 gm
	25B *	With amplifier	0.2 gm
Frequency	8309	High frequency	180 kHz
Shock	8309	Vibration	150 kg
		Mechanical	1000 kg
Sensitivity	8318	680 pC/g	
Temperature	6240M10 *	760 °C	

Note: * denotes that the product is from Endevco. The others are from B&K.

2.5 Piezoelectric accelerometer design

Based on the different piezoelectric element configurations discussed in section 2.2, piezoelectric accelerometers can be classified as follows and studied one by one.

2.5.1 Flexural mode

Flexural mode design, shown in Fig. 2.12, utilizes beam shaped piezoelectric elements, which are supported to create stress on the piezoelectric element when accelerated. It has narrow frequency range and low over-shock survivability, the design offers a low profile, lightweight, excellent thermal stability and an economical price. It is also insensitive to transverse motion. Generally, this design is well suited for low frequency, low *g* level applications during structural testing [2-12].

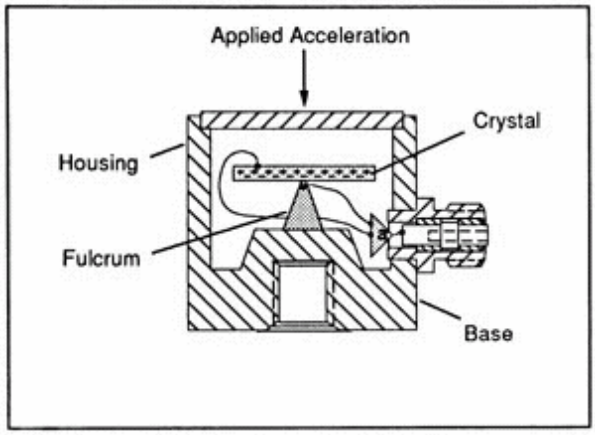

Fig. 2.12: Flexural mode design.

2.5.2 Compression mode

Compression mode accelerometers are widely used because of the simple structure, high rigidity and historical availability. There are basically three types of compression designs, which are upright, inverted and isolated designs.

Upright compression design, Fig. 2.13 [2-12], is a traditional and simple construction. It gives a moderately high sensitivity-to-mass ratio. The piezoelectric element-spring-mass system is mounted on a cylindrical center post attached to the base of the accelerometer. The design is very stable, but even with careful design the influence from unwanted parameters is higher than for the other construction types. Because the base and center post effectively act as a spring in parallel with the PZ elements, any dynamic changes in the base, such as bending or thermal expansions, can cause stresses in the piezoelectric elements and hence erroneous outputs.

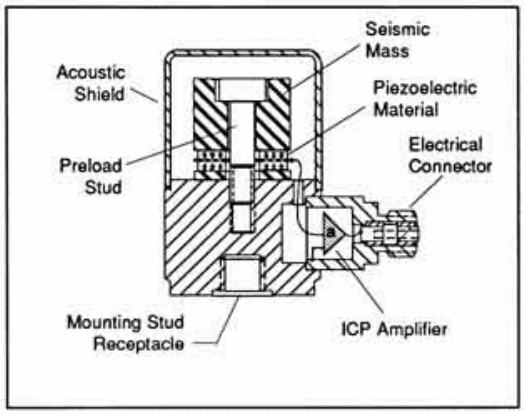

Fig. 2.13: Upright Compression design.

Inverted compression design, Fig. 2.14, isolates the piezoelectric element from the mounting base therefor reduces base bending effects and minimizes effects of a thermally unstable test structure. Reference standard calibration accelerometer utilizes this design, such as Brüel & Kjær accelerometer Type 8305 [2-12, 17].

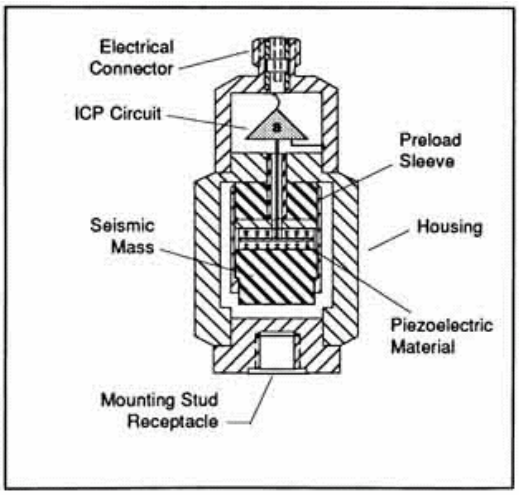

Fig. 2.14: Inverted compression design.

Isolated compression design, Fig. 2.15 [2-12], reduces erroneous outputs resulted from base strain and thermal transients because of mechanically isolating the piezoelectric elements

from the mounting base and utilizing a hollowed out seismic mass which acts as a thermal insulation barrier.

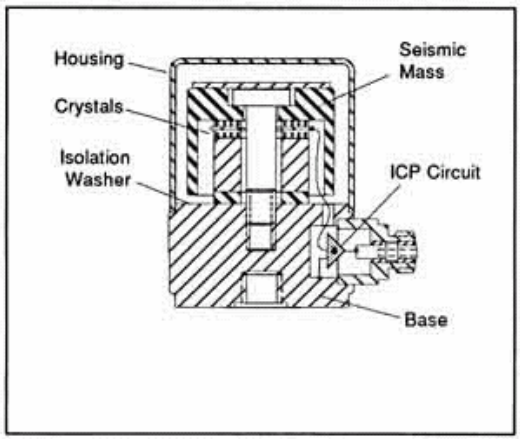

Fig. 2.15: Isolated compression design.

2.5.3 Shear mode

Shear mode design bonds or sandwiches the piezoelectric element between a centre post and seismic mass. Under acceleration, the mass causes a shear stress to be applied to the ceramic. Because of isolating the ceramic from the base and housing, shear accelerometers excel in rejecting thermal transient and base bending effects. Furthermore, the shear geometry itself results in a small size. Due to this combination of good characteristics, shear mode type accelerometers offer better performance [2-8, 16, 17] than the other two modes.

DeltaShear® design, Fig. 2.16, has three piezoelectric elements and three masses that are arranged in a triangular configuration around a triangular center post [2-8, 10, 16]. They are held in place using a high-tensile clamping-ring. Besides the feature of the shear principle, the DeltaShear® design gives a high sensitivity-to-mass ratio compared to other designs, and has a relatively high resonance frequency. No adhesives or bolts are required to hold the assembly together and this ensures optimum performance and reliability. The excellent overall characteristics of this design make it ideal for both general-purpose accelerometers and more specialized types.

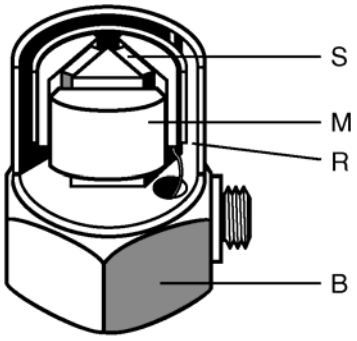

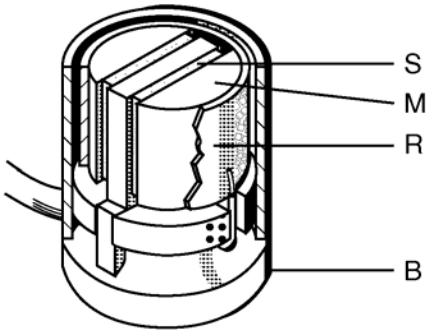

S: Sensing element M: Seismic mass R: Clamping ring B: Base

Fig. 2.16: DeltaShear® design. Fig. 2.17: Planar Shear design.

Planar Shear design has two rectangular slices of piezoelectric material that undergo shear deformation as in the DeltaShear® design. They are arranged on each side of a rectangular center post. Two mass are formed as shown in Fig. 2.17 and held in position using a high tensile clamping-ring that performs the same function as in the DeltaShear® design [2-10, 16].

Annular Shear design, Fig. 2.18, forms the piezoelectric element and the mass into rings and mounted around a center post. The elements are glued or soldered together [2-17].

Bolted Shear design, Fig. 2.19, is similar to Planar Shear design, the difference is that in Bolted Shear design a pre-load screw is used to hold seismic mass and quartz plate [2-8, 11] instead of using a clamping ring.

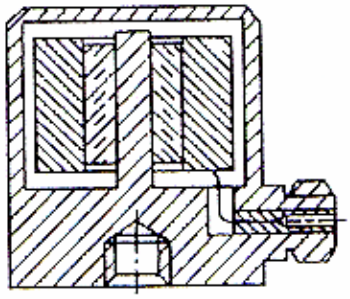

Fig. 2.18: Annular Shear design.

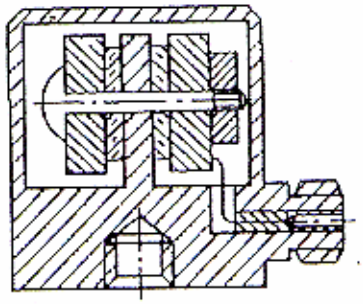

Fig. 2.19: Bolted Shear design.

ThetaShear® design, Fig. 2.20, has a simple construction [2-19].

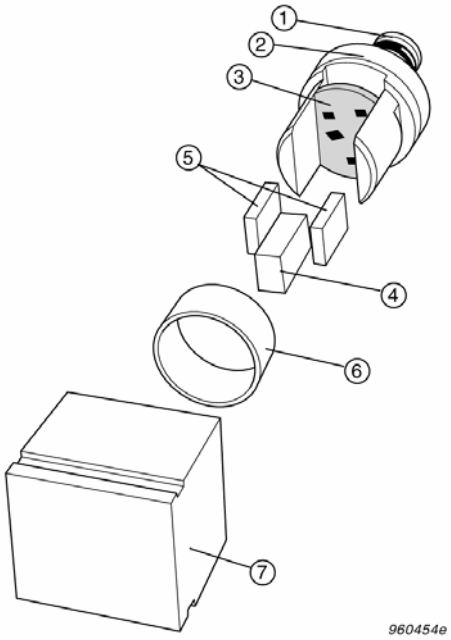

Fig. 2.20: ThetaShear® design.

The connector① is an integrated part of the top piece② that also contains the preamplifier③. The slotted cylindrical stanchion holds a central seismic mass④ The parts are firmly held together without use of any bonding agent other than friction. This assembly is hermetically welded to the housing⑦. This patented design of B&K combines the advantage of the shear principle, simplicity, and low mass-loading to provide low-cost, flexible and high-performance transducers.

Compared to other shear designs, the DeltaShear® and Planar Shear accelerometers use two or three mechanically de-coupled piezoelectric elements. This can be seen as an advantage. The Annular Shear accelerometers are a little more sensitive to base bending than the two designs in question due to the closed ring shape of their piezoelectric elements. Some Bolted Shear accelerometers are also sensitive to base bending, probably because the electrical insulation around the bolt holding the assembly together gives a too stiff coupling between the center post pin and the masses.

OrthoShear® design, shown in Fig. 2.21, is a new design used for triaxial accelerometers. The original triaxial accelerometer consisted of three individual accelerometers mounted in a single housing and positioned so that vibration can be measured in three mutually perpendicular directions. This limits the reduction of the size and also means that the three axes have different points of reference. OrthoShear® design does not have such problem. It is built around a common seismic mass. This unit-mass design enables a very compact triaxial accelerometer where all the axes have the same point of reference. In this design, the seismic mass⑥ is surrounded by a piezoelectric ring⑤ that is surrounded by four individually suspended curved plates④. The suspension pins③ mean that the different sections are exposed to shear forces for different directions of acceleration. The assembly is clamped together by the outer ring⑦. The preamplifier②, suspension pins③ and connector① constitute an integral part that is hermetically welded to the housing⑧ [2-10, 20, 21].

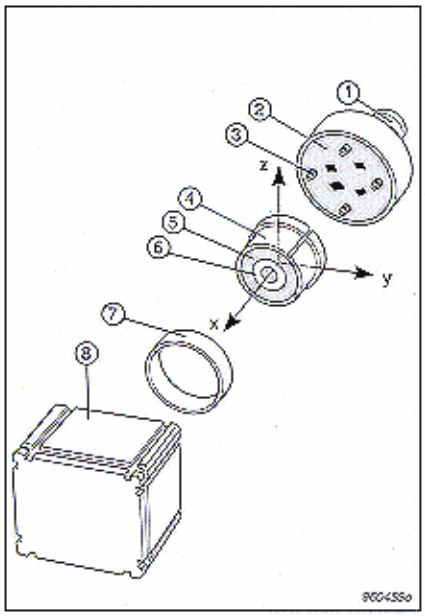

Fig. 2.21: OrthoShear®.

A comparison between the designs mentioned above is shown in Table 2.7. Based on the comparison, we can only have a rough overview. It is still very difficult to choose a design for certain requirements because of the fact that we do not have the objectives and detailed understanding for these designs, and they cannot be obtained experimentally. Therefore we need simulation methods to make models for the designs, compare the simulated results. It is the only possible way to understand the designs and the accelerometers.

Table 2.7. Comparison between different designs.

	Compression mode	Shear mode				
		Annular Shear	ThetaShear®	DeltaShear®	Planar Shear	OrthoShear®
Sensing elements	Quartz or ceramic layers	Piezoceramic ring	Piezoceramic disks	Piezoceramic disks	Piezoceramic or quartz disks	Peizoceramic ring
Resonance	High	High	Medium	High	High	Low
Thermal transient	High	Low	Low	Low	Low	Medium
Base-bending effects	High	Medium	Medium	Low	Low	Medium
Robust	High	High	High	High	High	Low
Cost	Low	Medium	Low	High	Medium	High

2.6 Conclusion

The chapter gives an overview of the piezoelectric accelerometer. General operating principles of the accelerometer are discussed. A comparison of the accelerometer characteristic is made. Based on the comparison, it can be seen that the piezoelectric accelerometer has very good performance, such as wide frequency range, accurate measurement, very robust and reasonably priced. But its weak point is that it cannot detect DC, which means the detection cannot go down to 0Hz.

Since the piezoelectric accelerometers make use of piezoelectricity, the piezoelectric materials are introduced afterwards. The section only scratches the surface of the theory.

Eighteen specifications are described in detail one by one in order to understand the design considerations. In short, choosing of the correct ceramic material is the key point. The piezoelectric accelerometer structure should be as stiff as possible, as small as possible, as light as possible. It should also be symmetric around the main axis as much as possible. Besides, compromises have to be made, such as between the sensitivity and the resonance frequency, between the charge output and the ceramic internal noise.

Finally detailed structures are presented for the flexural, compression and shear designs. A comparison shows that the DeltaShear design has the best properties. But the comparison is so rough that it is difficult to give a very objective understanding of each design. Therefore in the following chapters a new simulation method will be used to do this task.

References

2-1 Ilene J. Busch-Vishniac, “Mechanical Engineering Series, Electromechanical Sensors and Actuators”, Springer-Verlag New York, Inc., 1999

2-2 H.H. Bau, N.F. de Rooij, and B. Kloeck, “Sensors – A Comprehensive Survey, Volume 7, Mechanical Sensors”, VCH, pp. 331-358

2-3 Ljubisa Ristic, “Sensor technology and devices”, Artech House, 1994

2-4 Torben R. Licht, Patrik R. Scheeper, “Historical Perspective of accelerometer Technologies”, Trans. Of the Institute of electrical engineers of Japan, Part E, Vol.166-E, No. 7, 1996, pp. 256-267

2-5 R. Lauer, “Accelerometers using piezoelectric ceramic sensors”, Electronic Applications Bulletin, 1978, Vol. 35, Issue 2, pp. 105-116

2-6 Patrick L. Walter, “The History of the Accelerometer”, Sound and Vibration, March 1997, pp. 16-22

2-7 T. Meydan, “Recent trends in linear and angular accelerometers”, Sensors and Actuators A 59(1997), pp. 43-50

2-8 Torben R. Licht, et al., “Recent Developments in Accelerometer Design”, Brüel & Kjær, Technical Review, No.2, 1987, pp. 1-22

2-9 Harry N. Norton, “Sensor and analyzer Handbook”, Prentice Hall, Inc. Englewood Cliffs, 1982

2-10 “Acceleration Vibration & Shock”, January, 1997

2-11 J.R. Gilbert and S.F. Bart, “Enabling the Design and Use of MEMS Sensors”, Sensors Magazine, April 1998

2-12 PCB, “TechSupport”, http://www.pcb.com/tech_accel.html
2-13 “A New Method of Evaluating the Acoustic Response of Piezoelectric Accelerometers”, Endevco Technical Paper TP 232
2-14 Robert G. Seippel, “Transducers, Sensors, and Detectors”, Reston Pubishing Company, Inc., 1983
2-15 Brüel & Kjær, “Master Catalogue Electronic Instruments”, Denmark, 1989
2-16 Mark Serridge, Torben R. Licht, “Piezoelectric Accelerometer and Vibration Preamplifier Handbook”, 1987
2-17 Brüel & Kjær, “Transducer & Conditioning Catalogue 1997”, Denmark
2-18 Robert D. Sill, “Minimizing Measurement Uncertainty in Calibration and Use of Accelerometers”, Endevco Technical Paper TP 299
2-19 Brüel & Kjær, “Product Data, Miniature DeltaTron® Accelerometer – Types 4507 and 4508”, Denmark
2-20 Knud Styhr Hansen, “A New Design Principle for Triaxial Piezoelectric Accelerometers”, Technical Review, Brüel & Kjær, No.1, 1997
2-21 Knud Styhr Hansen, Patent, WO97/1496997.4.24
2-22 Peter Hauptmann, “Sensors Principles & Application”, Prentice Hall, 1991
2-23 James R. Carstens, “Electrical Sensors and Transducers”, Prentice Hall, 1993
2-24 Bernard Jaffe and William R. Cook, “Piezoelectric Ceramics”, Academic Press, 1971
2-25 J. Zelenka, “Piezoelectric Resonators and Their Applications”, Elsevier, 1986
2-26 Zhang Fuxue, Sun Kang, “Piezoelectricity”, September, 1984
2-27 Ferroperm, “Ferroperm Piezoelectric Materials”
2-28 APC International Ltd., “Piezoelectric Ceramic & Application Notes”, http://www.apc.thomasregister.com/olc/apc/notes.htm
2-29 Kistler Instrument Corporation, “Kistler – Piezoelectric Theory”, http://www.designinfo.com/kistler/ref/tech_theory_text.htm
2-30 “Definition & terms”, http://www.sensortech.ca/definitions.html
2-31 Fuhong Zhou, “Acoustic Transducers and Arrays”, Harbin Engineering University, 1984, in Chinese
2-32 R.C. Weast and M.J. Astle, “Handbook of Chemistry and Physics”, CRC Press, Inc., 1983
2-33 PCB, “Structure of Piezoelectric Accelerometers”
2-34 Walter Guyton Cady, “Piezoelectricity”, Dover Publications, Inc., 1964
2-35 B.A. Auld, “Acoustic Fields and Waves in Solids”, Krieger Publishing Company, 1990
2-36 A. Garcia-Valenzuela and M. Tabib-Azar, “Comparative study of piezoelectric, piezoresistive, electrostatic, magnetic, and optical sensors”, SPIE Vol.2291, 1994, p.125-142
2-37 B. Jaffe et al., “Piezoelectric properties of lead zirconate-lead titanate solid-solution ceramics”, J. Appl. Phys. 25, 1954, p.809-810
2-38 O.E. Mattiat, “Ultrasonic Transducer Materials”, Plenum Press, New York, 1971
2-39 “Handbook of Measurement Technology, Volume 5”, China Measurement Publishing House, in Chinese
2-40 R. Bogue and S. Doe, “Understanding the frequency response of piezoelectric accelerometers”, Noise & Vibration Control Worldwide, Vol. 14, Issue. 3, 1983, p.71-74
2-41 George Stathopoulos, “Effects of Mounting on Accelerometer Response”, Endevco Technical Paper TP 218

2-42 T.B. Gabrielson, “Mechanical-Thermal Noise in Micromachined Acoustic and Vibration Sensors”, IEEE Transactions on electron devices, Vol.40, No.5, May 1993, p.903-909
2-43 C. Kittel, “Elementary Solid State Physics”, Hohn Wiley & Sons, 1962

3
Development Methods for Piezoelectric Accelerometers

3.1 Introduction

For about half a century, the piezoelectric accelerometers have been designed by using modeling methods, such as the Simple Model method or the Advanced Model method. Usually these traditional methods use analytical and combined analytical-experimental methods, which means that the accelerometer is simplified to an equivalent circuit. As a one-dimension method, the equivalent circuit model has limited accuracy and cannot be used for two- or three-dimension analysis because it normally ignores the coupling effect between different modes. In other words, an equivalent circuit is only valid at the resonance of each mode. The parameters at one mode are calculated by neglecting the influences from other modes. Therefore, an equivalent circuit will never accurately represent the effects of the coupled factors from other modes.

With the advent of inexpensive and fast computers, numerical techniques have been rapidly applied to the solution of different complicated physical problems. Nowadays, in design areas, one of the most commonly used numerical techniques is the Finite Element Method (FEM). Generally speaking, FE simulated results are more accurate than the simulated results obtained by using traditional methods. Furthermore the FEM can estimate specifications which traditional methods cannot, and show results visually.

This chapter introduces the traditional development methods first, then moves to the FEM. At the end, a comparison between the methods described is given to show why we need the FEM and what can be expected from it.

3.2 Traditional methods

3.2.1 Simple model

As mentioned in Section 2.4, the charge sensitivity and the mounted resonance frequency can be expressed as:

$$S_q = d_{15} \cdot m_s \text{ (for Shear mode)} \tag{3.1}$$

$$S_q = d_{33} \cdot m_s \text{ (for Compression mode)} \tag{3.2}$$

$$f_m = \frac{1}{2\pi}\sqrt{k \cdot \frac{1}{m_s}} \tag{3.3}$$

In eqn. (3.3) k is the spring stiffness of the sensing system, m is the seismic mass. [3-11] says "Usually the results were disappointing due to their gross inaccuracy". The reason is that several components within a piezoelectric accelerometer have spring stiffnesses comparable to that of the sensing element itself. Therefore the k should be replaced by k_T, which is the total system spring stiffness.

The example in [3-11] shows that by changing the stiffness from k to k_T, the error in the resonance frequency is dropped from 228% down to 159%.

The study mentioned above is all based on the assumption that the accelerometer is a one degree of freedom system. Apparently it is not true. We should consider it as a multiple degrees of freedom system. But it is not at all simple to solve the equations for a multiple degrees of freedom system.

For a system with n degrees of freedom, i.e. n masses, there will be n simultaneous equations in ω^2, where $\omega = 2\pi f_0$. The more practicable solution is to apply a matrix technique, in this case the stiffness matrix is as shown below.

$$\begin{matrix} M_1\omega^2 - k_{11} & k_{12} & k_{13} & \cdots & k_{1n} \\ k_{21} & M_2\omega^2 - k_{22} & k_{23} & \cdots & k_{2n} \\ \vdots & \vdots & \vdots & \vdots & \vdots \\ k_{n1} & k_{n2} & k_{n3} & \cdots & M_n\omega^2 - k_{nn} \end{matrix} \tag{3.4}$$

where M_i is the mass of element i (i=1, …, n), k_{jj} is the sum of the stiffness acting directly upon mass element M_i, due to mass element j.

With equating eqn. (3.4), the error of the resonance frequency of the example used in [3-11] is reduced dramatically from 159% down to 57%.

3.2.2 Improved model - Transfer Function

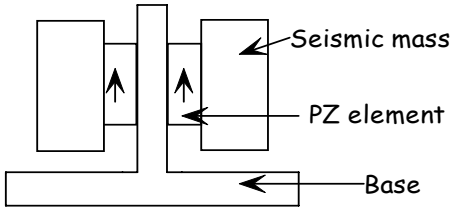

Fig. 3.1: Schematic structure of a Shear Design piezoelectric accelerometer.

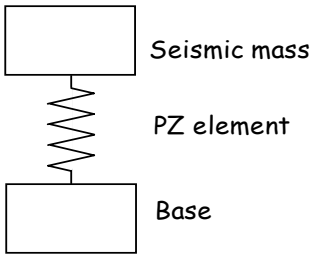

Fig. 3.2: Spring-mass system of the accelerometer.

Fig. 3.1 shows the schematic structure of a Shear Design piezoelectric accelerometer. The piezoelectric disc is fixed on one side of the base mounted on the object under test. The other side is attached to a freely moving mass, which is regarded as an ideal rigid body and is called

the seismic mass. The arrow denotes the poled direction of the piezoelectric disc. This structure can be treated as a spring-mass system shown in Fig. 3.2.

According to the Transformation Regulation [3-1], each element can be transferred from a mechanical system to an electrical circuit. Take the PZ element as an example. It can be expressed as mechanical components including a mass m_p, a compliance C_p and a loss resistance r_p. According to Admittance Analogy [3-1], it can be re-expressed as electrical components including a capacitance corresponding to the mass, an inductance corresponding to the compliance and a conductance corresponding to the lost resistance. They are shown in Fig. 3.3.

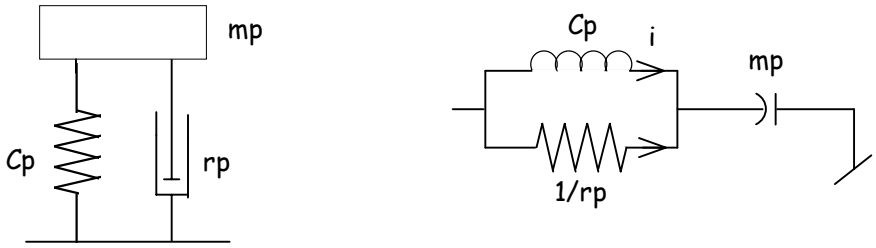

Fig. 3.3: PZ element expressed as mechanical and electrical components.

There are two methods to obtain the transfer function, the Discrete Element method and the Distribution Element method. Detailed information can be found from many good handbooks, such as [3-1, 2, 3]. It will not be repeated here.

(1) Discrete Element method
Based on the electrical circuit derived from the mechanical system, the transfer function describing the relationship between the output voltage and the input acceleration can be obtained either with MathCad or with Pspice, which are two commercial code packages.

(2) Distribution Element method, also called Transmission Line Model
The main idea is to model each component of an accelerometer as a transmission line, then add them together as connecting cables in series. We calculate the compliance per meter for each element of the electrical circuit. The compliance per meter means the compliance along the thickness of each component compared to the length of the cable.

3.2.3 Experience

Since accelerometers have been developed for more than half a century, there is not much space for developing the design theory. Experience is the most important tool for development engineers, especially for experienced designers. With experience, designers can point out what kind of influence on the specifications may be made by changing different components. They can modify existing products and make totally new designs by using the experiences and the traditional methods. But the experiences and the traditional development methods cannot predict results accurately. It means that they must work together with the trial-and-error method. Making, measuring and modifying prototype at workshop have to be done many times before the final prototype is finished.

Another consideration is that experience is tacit knowledge, which is stored in someone's mind instead of presented by textbooks or other media. Therefore it takes long time for designers to completely understand the fundamentals, especially for young engineers.

3.3 The Finite Element Method (FEM)

The FEM is a computerized method for predicting how a component/assembly will react to environmental factors such as forces, heat, vibration and so forth. It can be flexibly used to model any arbitrary geometry and characterize any given property of the material. In the product design cycle it is used as a "virtual prototyping" tool to predict what is going to happen when the product is used.

Generally speaking, the FEM works by breaking a real object down into a large number of elements. The behavior of each little element, which is regular in shape, is readily predicted by a set of mathematical equations. The summation of the individual element behaviors produces the expected behavior of the actual object. Huge amounts of handbooks deal with the whole theory [3-4, 5, 6, 7, 8, 9, 10].

Engineering problems are continuum problems in most cases, which means that all bodies of interest are continuous at all points in space. In general, the solution of such continuum problems using the FEM follows a general step-by-step procedure.

(1) Discretize the domain
The first step is to discretize the domain or solution region into elements. According to the type of the problem or the accuracy required, a variety of element shapes may be selected. As expected, the accuracy of the solution depends on the size or the number of the elements very much.

(2) Select the shape functions
Based on the shape of the elements used to discretize the domain, the shape functions of the elements can be selected for interpolation of the nodal values to obtain the variation of the field variable over the element. The principle of selecting the shape functions is that the field variable or its derivatives are continuous across the adjoining element boundaries.

(3) Formulate the element equations
Once the elements and their shape functions have been selected, the matrix equations expressing the properties of the individual elements can be determined.

(4) Assemble the element equations to obtain the system equations
In order to find the properties of the overall domain represented by the system of elements, the element equations must be assembled. After the assemblage of the element equations expressing the properties of the elements, the matrix equations expressing the properties of the entire system are formed. The principle of the assemblage is that the nodal value of the field variable at a node where the elements are interconnected should be the same for all elements sharing this node.

(5) Impose the boundary conditions
Before solving the system equations, they must be modified to include the boundary conditions of the problem.

(6) Solve the system equations
After assembly of the element equations and inclusion of the boundary conditions, a system of matrix equations are obtained to solve the unknown nodal values of the domain. The system equations are generally in the following form

$$\overset{n\times n}{[K]}\overset{n\times 1}{\{u\}} = \overset{n\times 1}{\{F\}} \tag{3.5}$$

where $[K]$ is called the *stiffness matrix*, $\{u\}$ is the vector of the unknown field variable and $\{F\}$ is called the *load vector*. The system of these matrix equations can be linear or non-linear. If they are non-linear equations, a linearization procedure will be applied to transform the non-linear equation into linear equation system in order to apply the ordinary solution techniques.

(7) Post-process the solution
In many problems post-processing of the solution is necessary to obtain additional variables such as stress and strain in mechanical problems and current density in electrical problems. To demonstrate the solutions, post-processors for graphical display of the results often are needed.

A very good description about the FEM theory for piezoelectric transducers simulation can be found in [3-12]. It includes the introduction of an axisymmetrical 8-node isoparametric rectangular element to model the volume and an axisymmetrical 3-node isoparametric line element to model couplings and external loadings. Then the mesh generator and the matrix assembly program are introduced briefly. The theory of analysis including Static Analysis, Modal Analysis, Harmonic Analysis and Transient Analysis are described as well. This thesis does not need to repeat them again.

Before the project was started, ANSYS® had been selected. Therefore, any other FEM code package will not be considered in this project.

3.4 The FEM based piezoelectric transducers study

In the field of piezoelectric solid mechanic modeling, Alik and Hughes [3-13, 14] were the first to derive the finite element model for piezoelectric solid mechanic coupling by applying the principle of virtual work at the beginning of 1970's. Since then, the FEM has been extensively used for piezoelectric device design.

A lot of work had been done to study the basic piezoelectric structures used by piezoelectric transducers. Some examples are the thin piezoceramic rings [3-18], the piezoelectric multilayer ceramics [3-19], the quartz plates [3-15], the piezoelectric or electrostrictive circular rod of finite length [3-16], and the axially symmetric piezoelectric ceramic disks [3-17].

The FEM based piezoelectric transducer design, at the beginning, focused on the vibration analysis [3-14, 20, 21]. As the FEM technique and the computation technique improve, much more analysis can be done. 1988 Lerch described the FEM based analysis of piezoelectric transducers used for ultrasonic imagine [3-22]. In the paper he proved that 1-D modeling (traditional methods) is not good enough for transducer design. A comparison between 2-D and 3-D modeling was given. As expected 3-D modeling can obtain more accurate results than 2-D modeling, meanwhile it takes more computation time than 2-D modeling. In the paper, Lerch simulated the mechanical strains and stresses, electrical fields and displacements, and various integral properties, such as the electrical input impedance or the electromechanical coupling coefficient.

1997 Cao presented the 2-2, 1-3 composite transducer simulation using FEM [3-23]. 1998 Mohammed et al. presented the modeling and simulation of piezoelectric ultrasonic transducer systems [3-24]. The thesis is not going to name all what had been done.

So far based on the publicly presented papers, the following things can be done by using the FEM for piezoelectric transducers. They are:

(1) Calculate eigen frequencies
(2) Analyze vibration modes
(3) Predict complex amplitude
(4) Predict stress distribution
(5) Predict voltage distribution inside ceramics
(6) Determine the properties of material
(7) Predict the amplitude at all nodes
(8) Predict the impedance plot
(9) Predict electromechanical coupling coefficient
(10) Predict the responses of transmit and receive sensitivities
(11) Predict directivity patterns

Though the work mentioned above may not include everything, to our knowledge there is not any publicly presented work showing the complete study on piezoelectric accelerometers as what will be shown in this thesis.

3.5 Comparison between the methods described

(1) Accuracy

All publicly presented FEM based studies show that the simulation accuracy of the FEM is much higher than that of the traditional methods. During the design process of the Brüel & Kjær accelerometer Type 4511, both the Improved Model and the FE model were used to predict the specifications before making any physical prototype. The comparison in Table 3.1 shows that the FE simulated results are more accurate than those of the Simple Model.

The Improved Model has not been studied in detail. Brüel & Kjær's experienced designer Lars Munch Kofoed said that if the good parameters and good experiences were available, the estimation accuracy could be 30%. It is not as good as FE simulated results.

Table 3.1:Comparison between the Simple Model, the FEM and experimental results.

Specifications	The Simple Model	FE simulation	Experimental results
Charge sensitivity	1.49 pC/ms^{-2}	1.45 pC/ms^{-2}	1.4 pC/ms^{-2}
Mounted resonance frequency	100 kHz	43.3 kHz	41 kHz

Due to the special properties of the piezoelectric material, the sensitivity can be estimated by traditional methods quite well according to eqn. (3.1) or eqn. (3.2). But the traditional methods ignore the coupling effect between different modes therefore they cannot estimate the resonance frequency accurately.

(2) Simulated specifications

The last section gives a full list of what can be done by using the FEM. For this project, the assigned simulated specifications are listed in Table 3.2. It shows that FE simulation can predict many specifications that traditional methods cannot, such as transverse resonance frequency and base bending effect, and so forth. How to calculate these specifications by using the FEM will be described in detail in Chapter 4.

Table 3.2: Simulated specifications list.

Specification	Traditional methods	FEM
Sensitivity	Good	Accurate (sensitivity plot is available)
Mounted resonance frequency	Very rough	Accurate
Transverse resonance frequency	Not possible	Accurate
Base bending effect	Not possible	Fair
Cable influence	Not possible	Good
Phase response	Not possible	Possible, but no result so far
Temperature transient	Not possible	Not possible so far

(3) Visualized simulated results

Using traditional methods, we can obtain the digital number of simulated results. Using the FEM, we can not only obtain the number, but also obtain the visualized results. Post-process can give the animated pictures showing how the model works at different resonance frequencies, can give the stress distribution, strain distribution and voltage distribution, and so forth visually. It makes the study of accelerometers more objective and easier. All of these results will be shown in Chapter 4.

(4) Scientific understanding

As mentioned in (3), visualized simulated results make the study of accelerometers more objective and easier. We can study the accelerometer in detail by using a virtual prototype, which means we can change anything, either the materials or the construction, to obtain the accelerometer performances that had been unknown once upon a time. According to the information obtained from the virtual prototype, we can obtain much better scientific understanding of accelerometers than before. It will improve the future designs.

(5) Development time and the cost
Before, the accelerometer design is made by using experiences and traditional methods first. After theoretical analysis, a prototype is made in the workshop. Because the prototype may not be good enough, modifications have to be done in the workshop again. Usually making and modifying prototypes have to be done several times. It takes time and money.

With FE simulation, a virtual prototype is built by using computer. Based on the virtual prototype, designers can evaluate and optimize the design before making any actual prototypes in the workshop. It can not only reduce the development time and cost, but also give designers opportunity to display their creativity.

However it has to be stated that the FEM is not a panacea for any engineering problem. A discussion is made at the end of Chapter 4.

3.6 Conclusion

Based on what mentioned above, it could be concluded that the FEM is a very promising development method for the piezoelectric accelerometer design. Compared with the traditional design methods, what can be expected from the FEM are accurate simulated results, more specifications that cannot be predicted by using the traditional methods, visualized simulated results, better scientific understanding of piezoelectric accelerometers, less development time and less cost. The following chapters will substantiate this.

References

3-1 K. Rasmussen, “Analogier mellem Mekaniske, Akustriske og Electriske Systemer”, Polyteknisk Forlag, 1973, in Danish
3-2 R.W.P. King, “Transmission Line Theory”, Dover Publications, Inc., 1965
3-3 Christos Christopoulos, “The Transmission-Line Modeling Method TLM”, The Institute of Electrical and Electronics Engineers, Inc., 1995
3-4 J.T. Mottram and C.T. Shaw, “Using Finite Elements in Mechanical Design”, McGraw-Hill Book Company, 1996
3-5 Singiresu S. Rao, “The Finite Element Method in Engineering”, 3rd edition, Butterworth Heinemann, 1999
3-6 C.S. Desai and J.f. Abel, “Introduction to the Finite Element Method – A Numerical Method for Engineering Analysis”, Van Nostrand Reinhold, Company, 1972
3-7 Mark Donley, et al., “Validation of Finite Element Models for Noise/Vibration/Harshness Simulation”, Sound and Vibration, August 1996
3-8 Ping dong, “The Finite Element Method – the Basic Method and Applications”, 1979, in Chinese
3-9 B. Hamonic, “Application of the Finite Element Method to the Design of Power Piezoelectric Sonar Transducers”
3-10 The Engineering Zone, “Introduction to Finite Element Analysis”, http://www.flinthills.com/~ramsdale/EngZone/design.htm

3-11 R. Bogue and S. Doe, “Understanding the frequency response of piezoelectric accelerometers”, Noise & Vibration Control Worldwide, Vol. 14, Issue. 3, 1983, p.71-74

3-12 H.H. Hansen, “Optimization of an Ultrasonic Transducer”, Ph.D. thesis, Technical University of Denmark, June 1997

3-13 H. Allik and T. Hughes, “Finite Element Method for Piezoelectric Vibration”, Int. J. Numer. Method. Eng. 2, 1970, p.151-157

3-14 H. Allik and K.M. Webman, J.T. Hunt, “Vibrational Response of Sonar Transducers Using Piezoelectric Finite Elements”, J. Acoust. Soc. Am., Vol. 56, 1974, p.1782-1791

3-15 D.R. Cowdrey, J.R. Willis, “Application of the finite element method to the vibration of quartz plates”, J. Acoust. Soc. Am., vol. 56, No. 1, July 1974, p.94-98

3-16 Yukio Kagawa, Tatsuo Yamabuchi, “Finite Element Approach for a Piezoelectric Circular Rod”, IEEE Trans. on Sonics and Ultrasonics, Vol. SU-23, No.6, November 1976, p.379-384

3-17 H.A. Kunkel et al., ”Finite-Element Analysis of Vibrational Modes in Piezoelectric Ceramic Disks”, IEEE Trans. on Ultrasonics, Ferroelectrics, and Frequency control, vol. 37, No. 4, July 1990, p.316-328

3-18 Anotnio Iula et al., “A Model for the Theoretical Characterization of Thin Piezoceramic Rings”, IEEE Trans. on Ultrasonics, Ferroelectrics, and Frequency control, Vol. 43, No. 3, May 1996, p.370-375

3-19 Richard L. Goldberg, et al, “Modeling of Piezoelectric Multilayer Ceramics Using Finite Element Analysis”, IEEE Trans. on Ultrasonics, Ferroelectrics, and Frequency control, Vol. 44, No. 6, November 1997, p. 1204-1214

3-20 Y. Kagawa and G.M.L. Gladwell, “Finite Element Analysis of Flexure-Type Vibrators With Electrostrictive Transducers”, IEEE Transaction on Sonics Ultrasonics, Vol. SU-17, No.1, 1970, p.41-49

3-21 Y. Kagawa and T. Yamabuchi, “Finite Element Simulation of Two-Dimensional Electromechanical Resonators”, IEEE Transaction on Sonics Ultrasonics, Vol. SU-21, 1974, p.275-283

3-22 Reinhard Lerch, “Finite Element Analysis of Piezoelectric Transducers”, IEEE Ultrasonics Symposium 1988, p.643-654

3-23 Wenwu Cao, “Transducer design simulation using finite element method”, Proceedings of SPIE – The International Society for Optical Engineering”, Vol. 3037, 1997, p.103-110

3-24 Ebrahim M.A. Mohammed, Abderrahim Abbas, “Modeling and simulation of Piezoelectric Ultrasonic Transducer Systems”, Proceedings of the 17th IASTED International Conference Modeling, Identification and Control, February 1998, p.279-281

4
FEM Applied to Piezoelectric Accelerometers

4.1 Introduction

The comparison between the traditional development methods and the FEM shown in last chapter gives us many expectations on what the FEM can do. This chapter presents how to predict the specifications listed in Table 3.2 by using the FEM and what the results look like. A comparison between the measured and simulated results is made. At the end, a discussion about the comparison is given.

4.2 The FE simulation

In this section, the FE simulation procedure of an existing product is described in detail to illustrate how to simulate the specifications of a piezoelectric accelerometer.

OrthoShear® is the only design principle to achieve a triaxial piezoelectric accelerometer with a single seismic mass in the world [4-1, 2] while all other triaxial piezoelectric accelerometers are made by putting three units into one housing [4-3, 4, 5, 6]. Due to the uniqueness of the design, the OrthoShear® accelerometer, B & K Type 4506, is chosen as the sample to present the simulation procedure.

4.2.1 The FE model

The structure and the ceramic material are modeled with element SOLID45 and element SOLID5 defined by ANSYS® [4-7], respectively. Both elements have the same profile as shown in Fig. 4.1, where I, J, to P denote the node, ①, ② to ⑥ denote the surface.

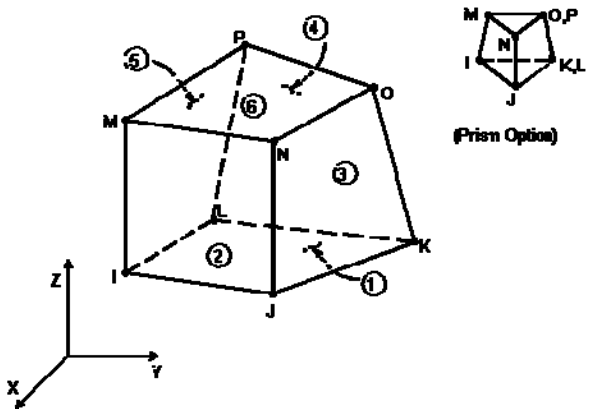

Fig. 4.1: Element profile.

SOLID5 is a 3-D coupled-field solid element used to model the ceramic. It has a 3-D magnetic, thermal, electric, piezoelectric, and structural field capability with limited coupling between the fields. It has eight nodes with up to six degrees of freedom at each node. The degrees of freedom are translations in nodal x, y and z direction, temperature, voltage and scalar magnetic potential.

SOLID45 is used for the 3-D modeling of solid structures. It is defined by eight nodes having three degrees of freedom at each node: translations in nodal x, y and z direction. The element has plasticity, creep, swelling, stress stiffening, large deflection, and large strain capabilities.

The piezoelectric material is poled in the upward direction in the height dimension. Its properties are given in Table 2.3. The structure is modeled as 3-D solid material. Table 4.1 shows the material properties normally used for the piezoelectric accelerometers.

Table 4.1: Material properties for the structure.

Material	Density (kg/m^3)	Young's modulus (10^{10} N/m^2)	Poisson's ratio
Tungsten	17500.	34.	0.27
Stainless steel	7860.	20.	0.30
Titanium	4500.	9.0	0.32
Inconel	8280.	19.5	0.31
Brass	8600.	10.4	0.37
Aluminum	2700.	9.0	0.32
Berylco	8746.	15.	0.30

The complete FE model, called virtual prototype as well, has totally 3976 elements. Fig. 4.2 shows the center part including red seismic mass, cyan PZ-ring, blue arm, magenta insulating ring, cyan blue clamping ring, orange hinges and green thick film substrate. The materials used are tungsten for central mass, Pz23 for piezoelectric ring, stainless steel for arms, inconel for clamping ring, brass for hinges, titanium for housing. It should be stated that the arm is divided into four segments, which means the charge is collected from four separated ceramic surfaces.

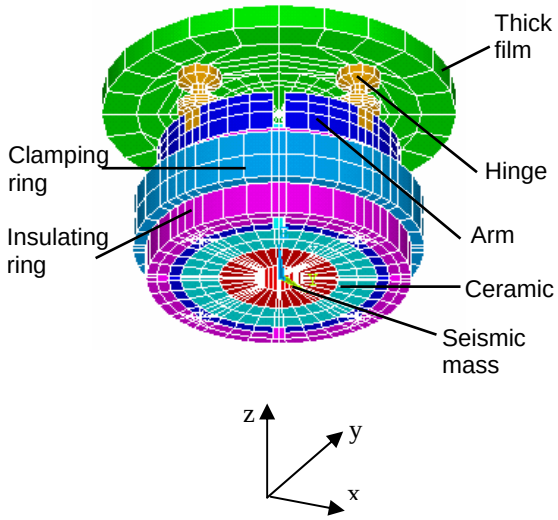

Fig. 4.2: FE model of Type 4506.

Since Type 4506 is a triaxial accelerometer, it is important to define the coordinate system first. We define that z-axis is longitudinal, x- and y-axis are parallel to the cross section of the accelerometer as shown in Fig. 4.2.

4.2.2 The FE simulated specifications

The method to simulate the specifications listed in Table 3.2 is described below, one specification at a time.

Frequency response

FE simulation can calculate the electrical charge in the piezoceramic parts, which is generated by the vibration loads of the FE model. Applying an acceleration on the mounted surface of the virtual prototype, by using Harmonic Analysis the *frequency response* can be simulated. The frequency response at 159.2 Hz is defined as the *charge sensitivity*.

If the entered material properties include the damping factor, the frequency response is a complex number as $a + jb$. $\sqrt{a^2 + b^2}$ is the charge output at a certain frequency, $tg^{-1}\left(\frac{b}{a}\right)$ is the corresponding phase response. If no damping factor is entered, the imaginary component is zero, which means the phase response cannot be achieved.

Since Type 4506 is a triaxial accelerometer, the boundary condition for different axis analysis should be applied differently as shown in Fig. 4.3. The cyan marks in the figures denote the mounting surface.

For Harmonic Analysis, the boundary condition is that the nodes on the mounting surface are fixed along the horizontal directions while a sinusoidal force perpendicular to the mounting surface is applied on these nodes. For example, when we calculate z-axis sensitivity, as shown in Fig. 4.3(a) the displacement of the nodes on the bottom of the computer model are fixed along x- and y-axis, meanwhile a sinusoidal force along z-axis is applied on these nodes.

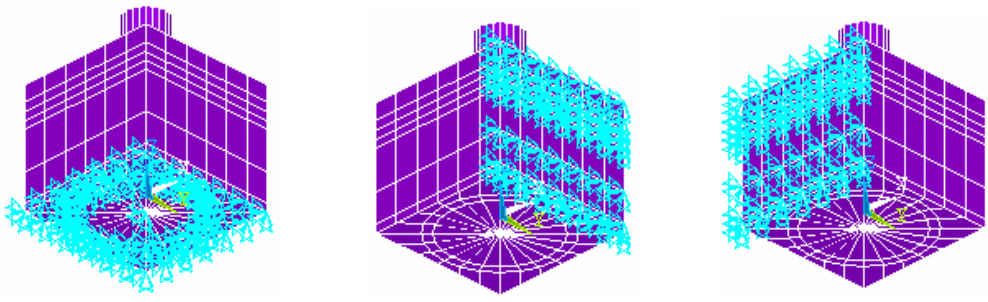

(a) z-axis (b) x-axis (c) y-axis

Fig. 4.3: Boundary condition.

The special charge-collecting theory of the OrthoShear® design is worthy of note [4-1]. Shown in Fig. 4.4, the center part is the seismic mass that is flanked by two PZ-elements

whose polarization direction is denoted by the arrow sign. The parts outside PZ-elements are the arms from which the signal is picked up.

The figure illustrates that when the excitation is applied along x-axis, the polarity of charges on PZ-element is in series. When the structure is vibrated along z-axis the polarity of charges on PZ-element is in parallel. It can also be seen that when the structure is vibrated along z-axis the voltage generated in the two PZ-elements will cancel each other seen from the charge amplifier. It also can be seen that when vibrated along x-axis, the signals generated in the PZ-elements will cancel each other and no signals are generated in the z-channel seen from the voltage amplifier. It means that cross-axis sensitivity can be avoided.

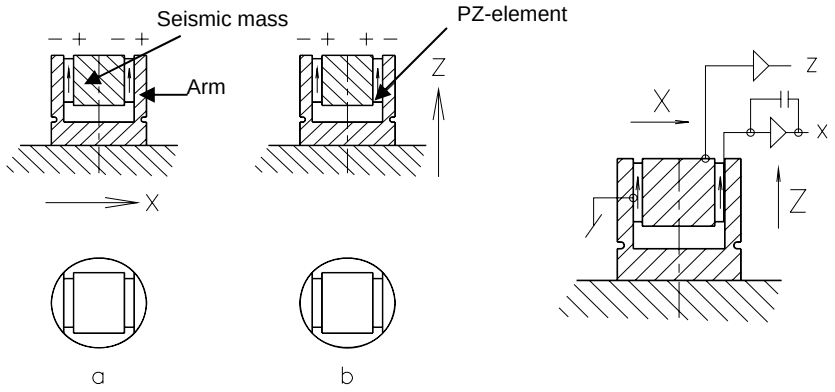

Fig. 4.4: Sketch of accelerometer with sensitivity in two directions.

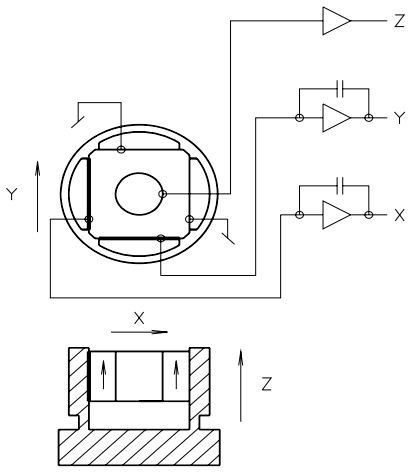

Fig. 4.5: Charge-collecting theory of the OrthoShear® Design.

The principle shown in Fig. 4.4 can be easily extended to the third direction, which is perpendicular to both the x- and z-axis. The sketches of a triaxial accelerometer are shown in Fig. 4.5. The z-axis works according to the “normal” shear accelerometer principle, whereas both the x- and y-axes work according to the principle shown in Figure 4.4. One advantage of

building a triaxial accelerometer according to this principle is that all three axes have the same center of gravity. The detailed description of the theory can be found from [4-1, 2].

Fig. 4.6 shows the frequency response with z-axis excitation in low frequency range. There is no traditionally estimated result for this. The slope in Fig. 4.6 is caused by the frequency-dependent piezoelectric constant due to the internal loss [4-9].

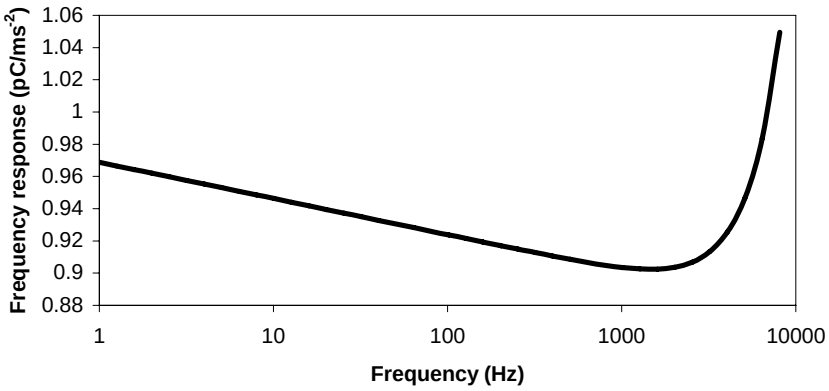

Fig. 4.6: The frequency response in low frequency range with z-axis excitation.

Applying the basic equations relating elastic strain *S* to stress *T*, i.e. $S = s \cdot T$ (where *s* is the elastic compliance) and electric displacement *D* to electrical field *E*, i.e. $D = \varepsilon \cdot E$ (where ε is the dielectric constant), to a piezoceramic block as described by Fig. 2.10, it can be said that piezoelectric constant is [4-10]

$$d_{15} = k_{15}\sqrt{\varepsilon_{11}^{T} \cdot s_{55}^{E}} \tag{4.1}$$

where k_{15} is the coupling coefficient, ε_{11}^{T} is the clamped dielectric constant and s_{55}^{E} is the elastic compliance at constant electrical field.

[4-11] studied the dependence of the piezoelectric coefficient on the frequency of the driving stress. The theory is beyond the scope of the project, but what we are interested in is that [4-11] proved ε_{11}^{T} in eqn. (4.1) does exhibit frequency dependence. The dependence varies from on batch of ceramic material to another batch. Based on the measurement done by B & K, ε_{11}^{T} decreases about 2.5% per decade of frequency to at least 20 MHz and increases 2.5% per decade of frequency below 1 kHz to at least 1 Hz. Therefore the slope should have a value of 2.5% per decade as shown in Fig. 4.6.

Fig. 4.7 shows the frequency response with z-axis excitation in full frequency range. The curve is very smooth and has only one peak existing at the z-axis mounted resonance frequency. Based on the definition defined in Section 2.4.8, we can say that the *usable frequency range* is 10 kHz.

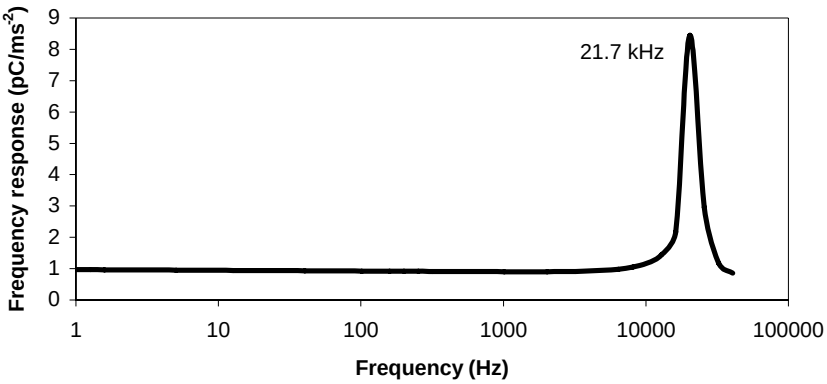

Fig. 4.7: The frequency response with z-axis excitation.

The amplitude of the resonant peak is primarily determined by the overall system damping, which is defined in terms of the mechanical quality factor Q_M. This FE model does not include damping. Therefore there should be a peak with infinite amplitude at the resonance. But the peak in Fig. 4.7 is not infinite. The reason is that due to the frequency step used within calculation iteration, the curve misses the charge output at resonance frequency. The calculation substantiates that the output at resonance frequency is nearly infinite compared to the output at other frequencies.

Another point that should be stated is as the mechanical and electrical losses are not easy to specify, they are not included in the simulation. Furthermore, the losses are significant around the resonance frequency. Therefore, at the resonance frequency, the difference between the simulated and the measured values becomes bigger as the frequency increases.

Based on what mentioned above, it can be concluded that the simulation cannot give accurate charge output at the resonance frequency.

The comparison of the charge sensitivities is shown in Table 4.2. 1 to 4 in the third column of the table denotes the number of each sensing element illustrated with Fig. 4.8. Fig. 4.9 illustrates the corresponding configuration of the ceramic, the arms and the hinges.

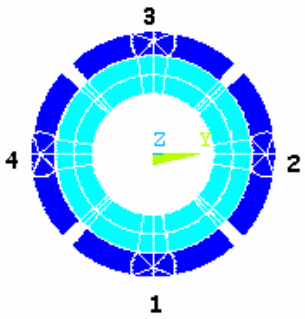

Fig. 4.8: The illustration of the number used for sensing elements.

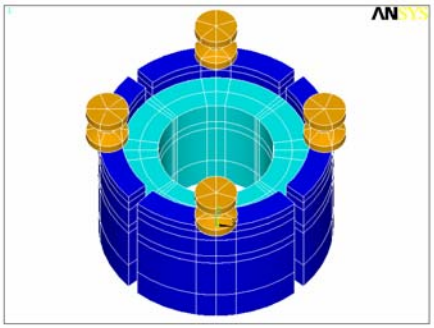

Fig. 4.9: The configuration of the sensing part of Type 4506.

It should be stated that piezoelectric constant d_{15} used for traditional estimations is 400 while it is 335 for FE simulation. The difference of d_{15} produces the difference of the sensitivities. Both d_{15} are given by the same supplier. Therefore, it is difficult to determine which d_{15} is more accurate.

Table 4.2: The charge sensitivities.

			Measured	FE simulated	Traditionally estimated
Charge sensitivity (pC/ms^{-2})	x-axis		1.4	**1.539799**	1.338
		1	-0.7	-0.755612	-0.669
		2		-0.0142925	
		3	0.7	0.784187	0.669
		4		-0.0142925	
	y-axis		1.4	**1.539799**	1.338
		1		-0.0142925	
		2	-0.7	-0.755612	-0.669
		3		-0.0142925	
		4	0.7	0.784187	0.669
	z-axis		1.0	**-0.91932**	
		1		-0.22983	
		2		-0.22983	
		3		-0.22983	
		4		-0.22983	

From the introduction in Section 4.1, we know that this special design uses shear stress to induce charge on ceramic, but there was no way to visualize the relationship between the shear stress and the induced charge before the advent of the FEM.

The shear stress XZ distribution with z-axis excitation is shown in Fig. 4.10. It can be seen that the stress at the hinges' position is the largest. It compiles to the design principle illustrated in Fig. 4.4. It can also be seen that the arm-gap areas have positive shear stress while the other areas have negative shear stress. The negative sign means that the shear stress is along the negative z-axis. The reason why we have positive and negative values at the same time is that when the components are excited, all stiff components will move accordingly, but

the soft ones will have a delayed movement compared to the stiff ones. The arm gap areas have the biggest stiffness change from stainless steel to the air. Therefore these areas have the positive stress distribution.

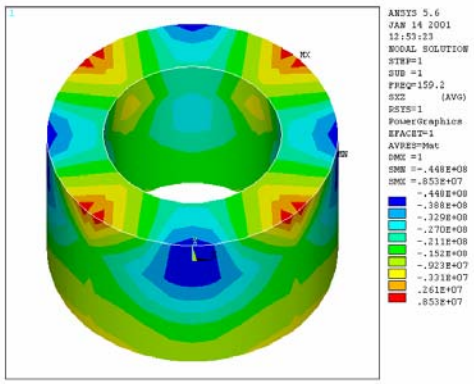

Fig. 4.10: The shear stress distribution in ceramic.

Fig. 4.11 shows the electric potential distribution when the ceramic is treated as an open circuit. Based on the theory about the ceramics, when charge is going to be measured on the surface of the ceramic, the ceramic should be treated as a short circuit; when voltage is going to be measured, the ceramic should be treated as an open circuit. It can be seen that the voltage distribution is even along the ceramic radius except the arm gap areas. This is due to the fact that the electrodes applied on the ceramic external surface only cover the areas connecting to the arms, which means the arm gap areas do not have the electrodes, is not grounded.

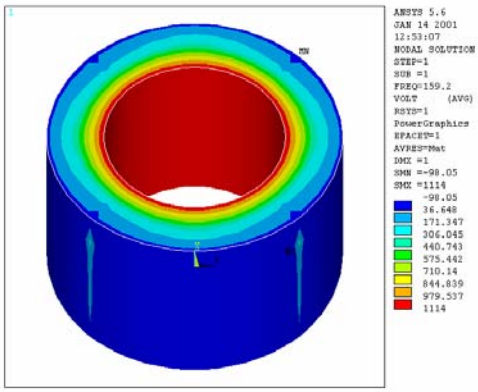

Fig. 4.11: The electric potential distribution in ceramic.

The voltage induced by the z-direction vibration can be read from Fig. 4.11. Since the charge output can be simulated as well, the capacitance can be obtained by $C = Q/V$. The simulated charge sensitivity is 0.92 pC/ms^{-2}, and the voltage sensitivity is 1.11 mv/ms^{-2}. Therefore the simulated capacitance is 830 pF.

From Section 2.4.7 we have already known that the smaller the capacitance, the smaller the noise produced by the ceramic. Therefore during design, the capacitance should be seriously considered.

Table 4.3: Capacitance.

	Measured	FE Simulated	Traditionally estimated
Capacitance	800 pF	830 pF	800 pF

Transverse sensitivity

As mentioned in Section 2.4.5, *transverse sensitivity* should be zero for an ideal accelerometer, but in practice it is not. Since a computer model has a perfect structure, it can be treated as an ideal accelerometer. Therefore the simulated transverse sensitivity is expected to be zero.

X- or y-axis excitation is applied on the bottom of the computer model as shown in Fig. 4.3(a). The charge output at 30 Hz is the transverse sensitivity.

The simulated and measured transverse sensitivities are shown in Table 4.4. We can see that they are zero.

Table 4.4: The transverse sensitivities.

			Measured	FE Simulated	Traditionally estimated
Transverse sensitivity (pC/ms^{-2})	x-axis Excitation		<0.05	**-0.340725E-6**	0
		1		-7.83336	
		2		-0.382835E-6	
		3		7.83336	
		4		0.202906E-6	
	y-axis Excitation		<0.05	**-0.340725E-6**	0
		1		0.202906E-6	
		2		-7.83336	
		3		-0.382835E-6	
		4		7.83336	

Unless there is a method to find out in practice what is the source causing the transverse sensitivity, the computer model cannot do much for this.

Resonance frequency

The mounted resonance frequency and *the transverse resonance frequency* are calculated by using Modal Analysis. The boundary condition is that the accelerometer is mounted on an infinite rigid surface, which means the displacements of the nodes on the mounting surface along x-, y- and z-axis are all fixed. Based on the simulation, it can be said that usually the first resonant mode is activated at the transverse resonance frequency.

When the model is mounted as shown in Fig. 4.3(a), the up-down mode is activated at the mounted resonance frequency of z-axis, which is 21.7 kHz. The resonance frequencies of x- and y-axis both are 10.4 kHz at which the transverse modes are activated. The symmetric structure is the reason why they are the same.

When the model is mounted on one side as shown in Fig. 4.2(b), the up-down mode is activated at the mounted resonance frequency of x-axis, which is 10.4 kHz. The resonance frequency of y-axis is 10.4 kHz. The resonance frequency of z-axis is 17.5 kHz.

We can see that 17.5 kHz is very different from 21.5 kHz. This is because that if the structure were completely rigid, with only the seismic mass being elastically restrained in one direction (a 1-DOF system), no matter which way the structure is turned and mounted, the resonance frequency would be the same. However, the accelerometer structure is not completely rigid, it is able to deform elastically. Therefore if it is mounted in any other way, the elastic deformations will be different, and so will all the mode shapes and resonance frequencies.

The FE simulation obtains good accuracy for predicting the mounted resonance frequencies. Table 4.5 shows the measured, FE simulated and traditionally estimated results.

Table 4.5: The mounted resonance frequency.

Mounted resonance frequency	Measured	FE simulated	Traditionally estimated
x-axis	10.0 kHz	10.4 kHz	Not available
y-axis	10.0 kHz	10.4 kHz	Not available
z-axis	19.0 kHz	21.7 kHz	Not available

The first disadvantage of using traditional methods to estimate resonance frequency is that the estimation is not accurate. This is the reason why there are not estimations for this product. Another disadvantage is that even though we do not care the accuracy, all what we can obtain are the numbers. With these numbers, we do not have any visual impression.

With the FE simulation, how the accelerometer operates at different frequencies can be studied visually. The simulated results with z-axis excitation are shown in Fig. 4.12 to 4.16. In the figures, the arrows denote the direction of the accelerometer movement; the colors denote the amplitude of the displacement; the “FREQ” denotes the frequency at which the mode is activated.

The simulation results when the virtual prototype is mounted on the bottom are presented in the following figures. Fig. 4.12 shows the first resonant mode. It is activated at 10.4 kHz. The figure shows that this frequency is the resonance frequency of y-axis. Fig. 4.13 shows the second resonant mode, which is the resonance mode of x-axis at 10.4 kHz. Fig. 4.14 shows the torsional mode, which is the third resonant mode of the model. The corresponding resonance frequency is 17.7 kHz. The forth mode shown in Fig. 4.15 is the resonant mode of z-axis at 21.7 kHz. Since the model is mounted on the bottom, it can be said that 21.7 kHz is the z-axis mounted resonance frequency.

Generally the four modes mentioned above exist for every accelerometer. Other resonant modes are very different from one accelerometer to another. These “other” modes can be activated at any frequencies. For this accelerometer, the “other” modes are activated at frequencies higher than the z-axis mounted resonance frequency. Fig. 4.16 shows one of these “other” modes.

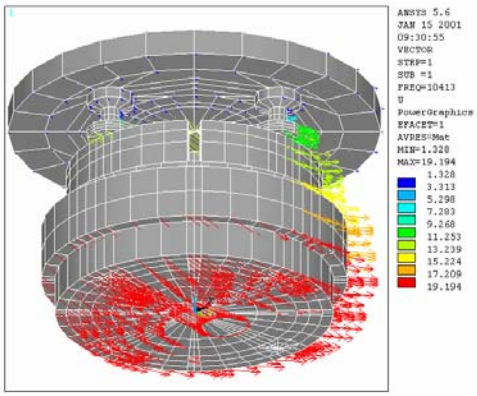

Fig. 4.12: The resonant mode of y-axis.

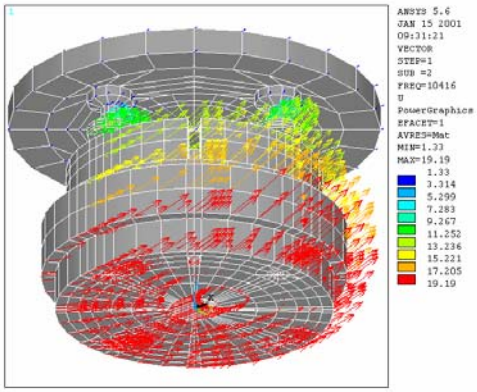

Fig. 4.13: The resonant mode of x-axis.

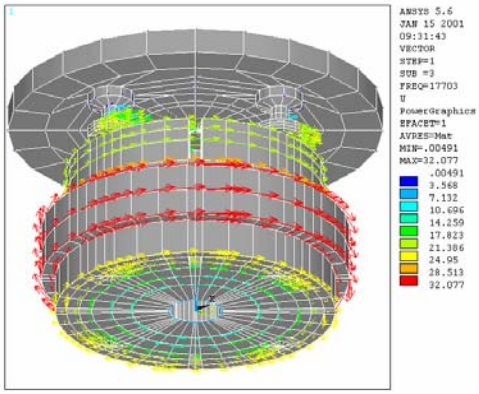

Fig. 4.14: The torsional mode.

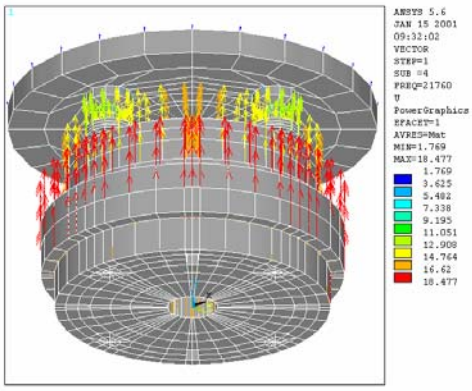

Fig. 4.15: The resonant mode of z-axis.

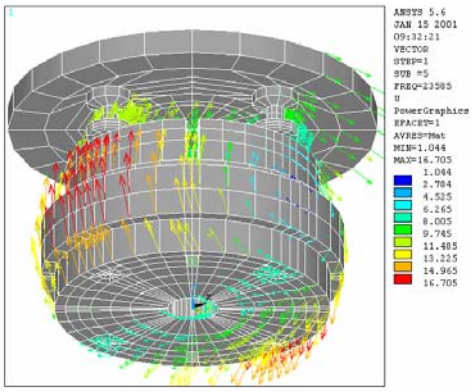

Fig. 4.16: One of the “other” modes.

The hinges of Type 4506 are important components because they act as springs. At the same time they are finer than other components. Therefore how the stress is distributed in the hinge is a very interesting topic. There are not measured and traditionally estimated results for this. Fig. 4.17 shows the FE simulated z-axis stress intensity distribution in one hinge when the model is subject to a z-axis excitation. The red color denotes the largest stress. The blue color denotes the smallest one.

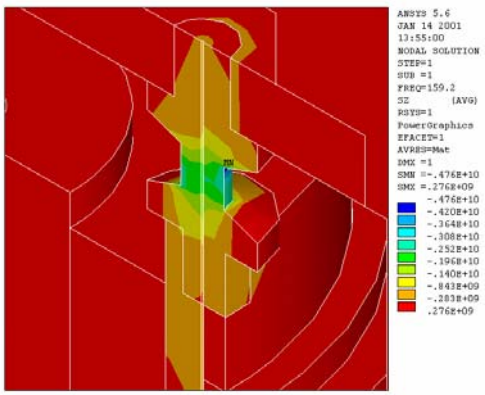

Fig. 4.17: The z-axis stress intensity distribution in one hinge with z-axis excitation.

We can see that the handle of the hinge has the largest stress distribution. On one hand, it means that the hinge does act as a spring; on the other hand, it means the hinge is easier to be damaged than other components, especially the curved area. Shock analysis can predict how strong the hinges. But the work has not yet been done.

Base bending effect

Fig. 4.18 shows the FE model for calculating the *base bending effect*. Experimentally the base bending sensitivity is measured by mounting the accelerometer near the fixed end of a heavy steel cantilever beam. Strain gauges are attached to the beam around the accelerometer. A displacement is applied at the free end of the beam, which stresses the accelerometer base. When the strain sensed by the strain gauges falls to a level of $250\,\mu\varepsilon$ the accelerometer output is measured and the acceleration required to produce an equivalent output is calculated. This acceleration is divided by the strain and the base strain sensitivity is obtained [4-8].

In the FE simulation, the FE model of the accelerometer is mounted on the fixed end of a heavy cantilever beam that is a part of the whole FE model as shown in Fig. 4.18. A force based on the beam dimension and the strain level $250\,\mu\varepsilon$ is applied at the free end of the beam illustrated by red arrows. Fig. 4.18 shows the z-axis displacement distribution.

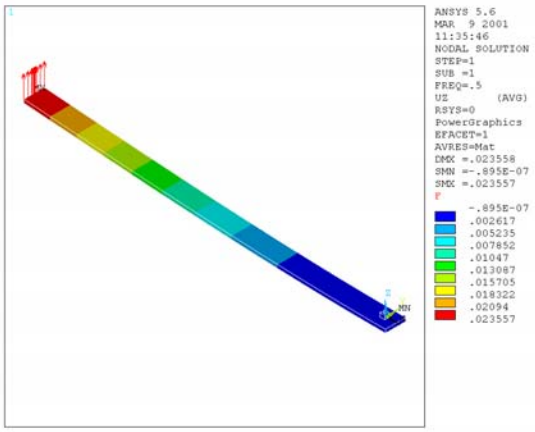

Fig. 4.18: The FE model for base bending effect.

The base bending effect of Type 4506 predicted by the FE simulation 0.14 $ms^{-2}/\mu\varepsilon$ is much bigger than the measured result, which is 0.03 $ms^{-2}/\mu\varepsilon$. It is due to the fact that during measuring the accelerometer is mounted on mounting clip or on adhesive tape 0.09 mm thick. The mounting clip and the adhesive tape act as damping factor so that the base bending effect is reduced.

Cable influence

From a practical point of view, the cable is always recommended to fix in order to avoid the *cable influence*. But it is very difficult to experimentally explain how the cable operates to make the influence. Now based on the FE model shown in Fig. 4.19, the cable influence can be simulated and visualized. Especially with the animated pictures, the results are very impressive and convincing. Unfortunately these pictures cannot be shown in the thesis.

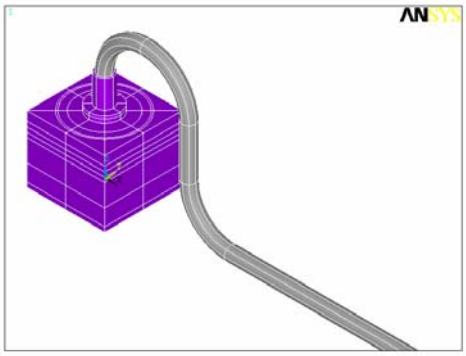

Fig. 4.19: The FE model for cable influence.

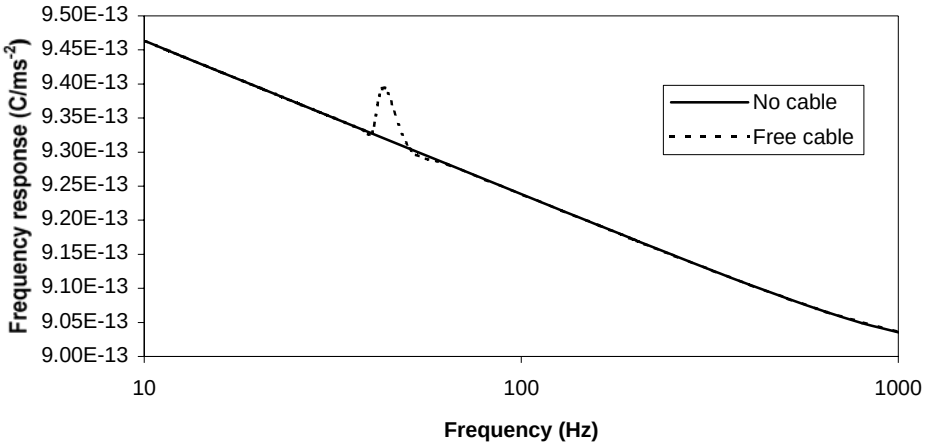

Fig. 4.20: Frequency response with the influence of the cable.

The frequency response in Fig. 4.20 shows that a free cable can induce an undesirable peak within usable frequency range. The influence of the cable on the frequency response can be minimized if the cable is fixed as shown in Fig. 4.21.

Fig. 4.21: The fixed cable.

Thermal analysis

Thermal analysis is very difficult to perform. Until now all work which had been done is based on a very simple model instead of an accelerometer model. Both steady-state thermal analysis and transient analysis are successful now if only the temperature distribution is concerned.

There are two ways to make Thermal analysis by using ANSYS® [4-7]. First, take the Electro-Magneto-Thermo-Structural Analysis, which means that four DOFs, displacement *u*, temperature *T*, voltage *V* and magnetic scalar potential ϕ are coupled together as described by eqn. (4.2).

$$\begin{bmatrix} [M] & [0] & [0] & [0] \\ [0] & [0] & [0] & [0] \\ [0] & [0] & [0] & [0] \\ [0] & [0] & [0] & [0] \end{bmatrix} \begin{Bmatrix} \{\ddot{u}\} \\ \{\ddot{T}\} \\ \{\ddot{V}\} \\ \{\ddot{\phi}\} \end{Bmatrix} + \begin{bmatrix} [C] & [0] & [0] & [0] \\ [0] & [C^t] & [0] & [0] \\ [0] & [0] & [0] & [0] \\ [0] & [0] & [0] & [0] \end{bmatrix} \begin{Bmatrix} \{\dot{u}\} \\ \{\dot{T}\} \\ \{\dot{V}\} \\ \{\dot{\phi}\} \end{Bmatrix}$$
$$+ \begin{bmatrix} [K] & [0] & [0] & [0] \\ [0] & [K^t] & [0] & [0] \\ [0] & [0] & [K^V] & [0] \\ [0] & [0] & [0] & [K^m] \end{bmatrix} \begin{Bmatrix} \{u\} \\ \{T\} \\ \{V\} \\ \{\phi\} \end{Bmatrix} = \begin{Bmatrix} \{F\} \\ \{Q\} \\ \{I\} \\ \{J_f\} \end{Bmatrix} \tag{4.2}$$

$[K^t]$ includes the thermal conductivity matrix of the material and thermal conductivity matrix of convection surface. $\{F\}$ includes applied nodal force vector, thermal strain force vector, force vector due to acceleration effects, Lorentz force vector, pressure load vector and Maxwell force vector. $\{Q\}$ includes applied nodal heat flow rate vector, heat generation rate vector for causes other than Joule heating, heat generation rate vector for Joule heating and convection surface vector. $\{I\}$ includes applied total current vector. $\{J_f\}$ includes applied nodal flux vector, source vector and coercive force (permanent magnet) vector.

In our case, we simply need to assume scalar magnetic potential coefficient matrix $[K^m]$, magnetic scalar potential vector $\{\phi\}$ and applied nodal flux vector $\{J_f\}$ to be zero. But it is unfortunately that the ANSYS® package used by the author does not have this function.

Another way is to make Thermal-Structure Analysis first, then make Electro-Structural Analysis afterwards. By making Thermal-Structural Analysis, we can simulate the temperature influence on the structure first. Then the piezoelectric effect can be simulated afterwards by making Electro-Structural Analysis.

So far, the calculation is not convergent. The reason is unknown. More work has to be done in the future.

4.3 Comparison between the simulated and measured results

The simulation had been made for at least one accelerometer for each design. B & K accelerometers are chosen. The comparison between the measured and simulated results is shown in Table 4.6.

Table 4.6: Comparison between the measured and simulated results.

	Specification	Measured results	Simulated results
Compression Design (Type 8305)	Mounted resonance frequency	38 kHz	38.5 kHz
	Transverse resonance frequency		8.7 kHz
	Sensitivity	0.12 pC/ms^{-2}	0.125 pC/ms^{-2}
Annular shear Design (Type 8325)	Mounted resonance frequency	27 kHz	27.5 kHz
	Transverse resonance frequency		6.1 kHz
	Sensitivity	5.0 pC/ms^{-2}	5.37 pC/ms^{-2}
DeltaShear® Design (Type 4384)	Mounted resonance frequency	42 kHz	47.6 kHz
	Transverse resonance frequency	15 kHz	15.1 kHz
	Sensitivity	1.0 pC/ms^{-2}	1.03 pC/ms^{-2}
Planar shear Design (Type 4374)	Mounted resonance frequency	85 kHz	86.5 kHz
	Transverse resonance frequency	21 kHz	16.7 kHz
	Sensitivity	0.11 pC/ms^{-2}	0.15 pC/ms^{-2}
ThetaShear® Design (Type 4508)	Mounted resonance frequency	34 kHz	36 kHz
	Transverse resonance frequency		16.2 kHz
	Sensitivity	0.50 pC/ms^{-2}	0.52 pC/ms^{-2}

4.4 Discussion

Table 4.2, 4.3, 4.4 and 4.6 show that compared to the measured results, the simulated results are good for Compression, Annular shear and ThetaShear® designs, fair for DeltaShear®, Planner shear and OrthoShear® designs. The accuracy is accepted by the main designer, Knud Styhr Hansen, of B & K for existing accelerometers' modification.

The reasons for the deviations are as following.

(1) The FEM is a numerical method to analyze complicated engineering problems. As the same as any other numerical methods, the FE simulation has truncation error and rounding error. It can never give absolutely correct results. The error also arises from the discrete size of each element in the mesh and the underlying interpolation scheme. What we can say is that the FE simulation is more accurate than the simulation made by using traditional development methods.

(2) The FE model is not the same as the physical product. The components in physical products cannot be perfectly manufactured and assembled, but the FE model is perfect from every point of view. Therefore, there is an essential distinction between a FE model and a physical product, especially if the design has a complicated structure as DeltaShear® design.When we perform the simulation, the complete sets of piezoelectric material characteristics are not available. These material properties are given by supplier, but not identical to those of the materials actually used in transducer fabrication. It means that the material properties used can never be 100 percent correct. Since the piezoelectric elements act as a spring, their properties are much more important compared to those of the other materials used, especially the piezoelectric constant d_{15} for shear design and d_{33}

for compression design, which are given by suppliers. In fact suppliers calculate d_{15} based on measured constant d_{33} instead of measuring it directly in laboratory. This introduces even more uncertainty. As for the other materials used, we cannot obtain the exact properties either.

(3) The density of the FE mesh influences the simulation accuracy significantly. Even the shape of element used influences the results much. As recommended by ANSYS®, an initial analysis should be performed. Then reanalyze the problem using twice as many elements in critical regions, and compare the two solutions. If the two meshes give nearly the same results, then the mesh is probably adequate. If the two meshes yield substantially different results, then further mesh refinement might be required. The mesh should be kept refining until nearly identical results for succeeding meshes are obtained. But a fine mesh might not be accepted from a commercial point of view for us. The computer used to make the simulation behind the thesis is a personal computer, which has 128MB RAM (changed to 384MB RAM recently), 300MHz processor. Therefore a compromise between the simulation accuracy and the simulation time has to be made. Some papers presented the computation power which were used to make simulation. [4-12, 13] used SPAR-10 Sun workstation, [4-14] used Sun Sparc 5 workstation and [4-15] used HP9000 series 735 workstation.

(4) All simulations are made based on the very original information of existing products. The results shown have not been adjusted according to the measured results though they would be more accurate if we changed material properties or dimensions of the computer model. The reason why we did not do it is that we want to use the FEM as a design tool to design new product, therefore, we want reliable results instead of adjusted accurate results. For example, we can change material properties to achieve more accurate simulation results for any existing products. But the material properties might be different from stock to stock. It is impossible to predict the accurate properties advanced. Therefore it is not necessary to change material properties just in order to achieve “accurate” simulated results.

4.5 Conclusion

A complete simulation procedure for a piezoelectric accelerometer was presented in this chapter. The simulation of the frequency response, resonance frequency, base bending effect, cable influence, and thermal analysis (not finished yet) are described in detail. It can be seen that with the aid of the FE simulation we have the opportunity to predict the specifications of a piezoelectric accelerometer by using a computer model, so called virtual prototype, instead of any physical prototype. The whole procedure not only comes up with the digital numbers but also with the visualized results to improve our scientific understanding of piezoelectric accelerometers.

A comparison between the simulated and the measured results for typical designs shows that good agreement can be achieved. The deviation, which is acceptable, is the result of the numerical error, the difference between the physical product and the computer model, the uncertainty of the material properties, the computing power, and so forth.

The difference between the simulated and the measured results can be reduced by "post-processing", which is changing the material properties or mechanical dimension after the computer model is finished. But in practice the uncertainty of the material properties and the dimension (due to the tolerance) cannot be avoided, the most meaningful conclusion to us is that we are able to obtain reliable simulated results by using the FEM for piezoelectric accelerometers.

The next chapter is going to present what we can do with virtual prototypes for the future design.

References

4-1 Hansen, Knud Styhr, "A New Design Principle for Triaxial Piezoelectric Accelerometers", Technical Review, Bruel & Kjaer, No. 1, 1997

4-2 Hansen, Knud Styhr, Patent, WO97/1496997.4.24

4-3 Bruel & Kjaer, "Transducer & Conditioning Catalogue 1997", Denmark

4-4 http://www.endevco.com

4-5 http://www.kistler.com

4-6 http://www.pcb.com

4-7 "ANSYS Manual"

4-8 Mark SMark Serridge, Torben R. Licht, "Piezoelectric Accelerometer and Vibration Preamplifier Handbook", Bruel & Kjaer, 1987, Denmark

4-9 R. Bogue and S. Doe, "Understanding the frequency response of piezoelectric accelerometers", Noise & Vibration Control Worldwide, Vol. 14, Issue. 3, 1983, p.71-74

4-10 Ferroperm, "Ferroperm Piezoelectric Materials"

4-11 Dragan Damjanovic, "Stress and frequency dependence of the direct piezoelectric effect in ferroelectric ceramics", J. Appl. Phys. 82(4), August 1997, p.1788-1797

4-12 James F. Tressler et al., "Finite Element Analysis of the Cymbal-Type Flextansional Transducer", IEEE Transactions on Ultrasonics, Ferroelectrics, and Frequency Control, Vol. 45, No. 5, September 1998, p.1363-1369

4-13 Richard L. Goldberg et al., "Modeling of Piezoelectric Multilayer Ceramics Using Finite Element Analysis", IEEE Transactions on Ultrasonics, Ferroelectrics, and Frequency Control, Vol. 44, No. 6, November 1997, p.1204-1214

4-14 J.C. Adamowski et al., "Combination of analytical and finite element methods to obtain acoustic fields in complex structures driven by piezoelectric multilayer transducers", IEEE Ultrasonics Symposium 1997, p.955-958

4-15 Ebrahim M.A. Mohammed et al., "Modeling and Simulation of Piezoelectric Ultrasonic Transducer Systems", Proceedings of the 17th IASTED International Conference Modeling, Identification and Control, February 1998, p.279-281

5
Improved Scientific Understanding of Piezoelectric Accelerometers

5.1 Introduction

Different piezoelectric accelerometer designs described in Chapter 2 have been used for many years. Though designers have already known the advantages and disadvantages of each design, they might still cannot answer the questions about details before making phyasical prototype at workshop, such as “How big is the influence of changing seismic mass material on the mounted resonance frequency?”, “If we move the ceramic position a little upper, how big is the influence on the mounted resonance frequency and the sensitivity?”. It is not practical to analyze the physical prototype to answer the questions one by one. The alternative is answering the question with virtual prototypes. With virtual prototypes, we can not only answer the questions, but also improve scientific understanding of piezoelectric accelerometers, which is useful for the future design. All these are going to be presented in this chapter.

We use “virtual prototype” instead of “FE model” in this chapter because we are not going to mention the FEM, the simulation accuracy, and so forth anymore. What we are going to do is to make a detailed analysis on each design mentioned in Section 4.2.3 (except the Flexural mode design) with virtual prototypes.

5.2 Detailed analyses on piezoelectric accelerometer designs

In order to make the analyses general and simple, most virtual prototypes analyzed in this section only consist of key components, such as ceramic, seismic mass, center post and clamping ring if there is a clamping ring. When the influence of the housing is to be studied, a complete virtual prototype is used.

5.2.1 Compression design

Fig. 5.1 shows a compression design. The red seismic mass is put on the top of the cyan sensing elements. Since the base acts as a spring parallel to the sensing elements, it plays a very important role in the design. Therefore the base is included in the analysis. The blue holder is to isolate the sensing element from the base effect.

Material

The material used for each component can be changed for a certain purpose. For example, a more sensitive sensing material may increase the sensitivity, a stiffer material may increase the resonance frequency, a lighter material may reduce the weight, and so forth.

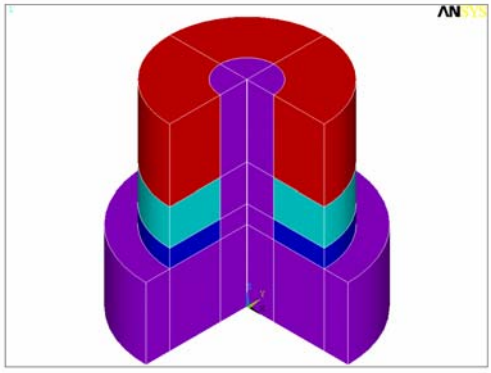

Fig. 5.1: A compression design.

Table 5.1 shows the material influence on the specifications. The material properties used are listed in Table 4.1. In order to get general information, all results are normalized according to the results obtained by using Pz23, Tungsten seismic mass and stainless steel center post & base, which is the most commonly used configuration. Superscript 1, 2, and 3 denotes that the results in the certain row are the mounted resonance frequency by using Pz23, the sensitivity by using Pz23, and the sensitivity by using Pz27, respectively. It will not be announced later.

Table 5.1: The influence of material on the specifications.

			Center post & Base			
			Stainless Steel	Titanium	Aluminum	Tungsten
Seismic mass	Stainless Steel	[1]	1.32	1.11	1.06	1.37
		[2]	0.5	0.54	0.53	0.52
		[3]	0.66	0.71	0.7	0.69
	Tungsten	[1]	1 #	0.84	0.79	1.07
		[2]	1 #	1.1	1.11	0.97
		[3]	1.32	1.45	1.47	1.28

[1]: The mounted resonance frequency with Pz23.
[2]: The sensitivity with Pz23.
[3]: The sensitivity with Pz27.
#: The reference.

(1) Ceramic
Pz27 produces a slightly higher mounted resonance frequency than Pz23. But the difference is so small that it can be neglected.

The sensitivity with different sensing element is different. The ratio between the sensitivities produced by Pz27 and Pz23 is 1.32, which is higher than the ratio between d_{33} of Pz27 and Pz23, 1.29. The reason is that the sensitivity of a compression design does not only determined by d_{33} and the seismic mass, but also determined by the stress acting on the ceramic.

(2) Seismic mass
The stainless steel seismic mass produces 0.5 times sensitivity and 1.32 times mounted resonance frequency of the tungsten seismic mass.

It has to be stated that the sensitivity is not decreased according to the density ratio between stainless steel and tungsten, which is 0.45. This is due to the fact that the m_s in eqn. (5.1) is not only contributed by the seismic mass $V \cdot \rho$, but also contributed by the other components m_1 including half ceramic, part of the center post.

$$S_q = d_{33} \cdot m_s = d_{33} \cdot (m_1 + V \cdot \rho) \tag{5.1}$$

(3) Center post & base
Table 5.1 shows that the sensitivity is determined not only by the seismic mass, but also by the center post & base. This is due to the operation principle of a compression design. The tungsten center post is stiffer than the stainless steel one, therefore it occupies more stress, consequently the ceramic gets less stress resulting smaller sensitivity.

Taking the stainless steel center post & base as a reference, the titanium center post & base produces 1.1 times sensitivity, the aluminum one produces 1.11 times sensitivity.

As for the mounted resonance frequency, the stiffer the center post & base, the stiffer the whole structure, the higher the resonance frequency. Taking the stainless steel center post & base as reference again, the mounted resonance frequency with titanium center post is 0.84 times, the aluminum one 0.79 times, the tungsten one 1.07 times.

According to Table 5.1, if the usable frequency range is the most important request, the stainless steel seismic mass and center post & base are the right choice. If the sensitivity is also an important requirement, the stainless steel center post & base and tungsten seismic mass are a good selection.

Structure
(1) Sensing element thickness
In a compression design, each component acts as a spring working parallel. The change of the sensing element thickness changes the stiffness of the whole structure.

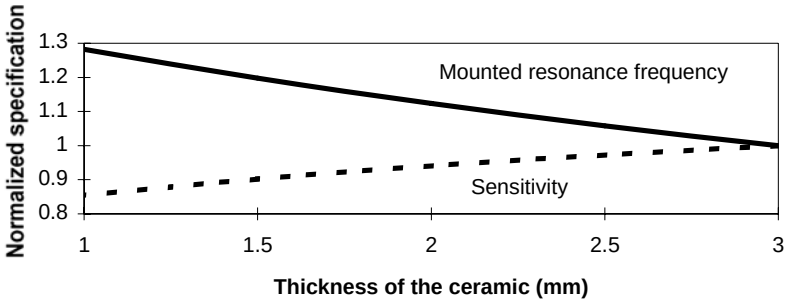

Fig. 5.2: The influence of the ceramic thickness.

The normalized resonance frequency and the sensitivity are shown in Fig. 5.2. It can be seen that as the sensing element thickness decreases, the resonance frequency increases, the sensitivity decreases. The increase of the resonance frequency is faster than the decrease of the sensitivity. But it does not mean that the ceramic thickness can be reduced unlimitedly to

increase the resonance frequency because the thinner the ceramic, the higher the capacitance, the higher the noise.

(2) Seismic mass
Chapter 2 has already mentioned that the center of gravity should be as low as possible. Therefore in this part only the influence of the seismic mass diameter is studied. The height of the seismic mass is kept constant.

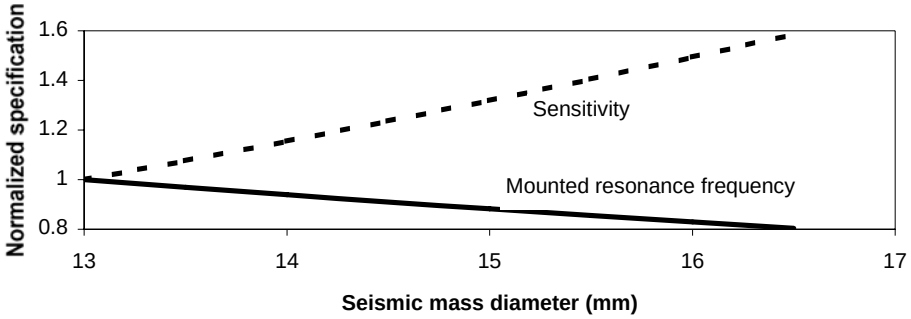

Fig. 5.3: The influence of the seismic mass.

Fig. 5.3 shows the normalized resonance frequency and the sensitivity. It can be seen that as the diameter increases the resonance frequency decreases, the sensitivity increases. The figure can be used to roughly determine the seismic mass dimension according to the resonance frequency and the sensitivity requirements.

(3) Holder thickness
There is a Beryllium holder between the sensing element and the base. It is used to isolate the base influence.

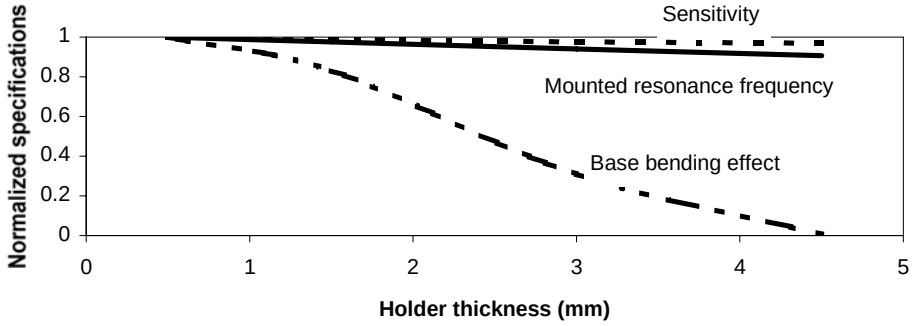

Fig. 5.4: The influence of the holder.

Fig. 5.4 shows that as the holder thickness increases, both the sensitivity and the mounted resonance frequency decrease slightly. It also shows that the thicker the holder, the less the base bending effect. Therefore the thickness of the holder is mainly determined by how much the base bending effect can be accepted.

A full structure

In a practice, the sensing elements of a compression design are thin cyan ceramic disks that are piled on top of the other in order to get high sensitivity. As illustrated with Fig. 5.5, there are totally 9 quartz discs. They are polarized in opposite direction. Therefore, the total output is 9 times the output of one disc.

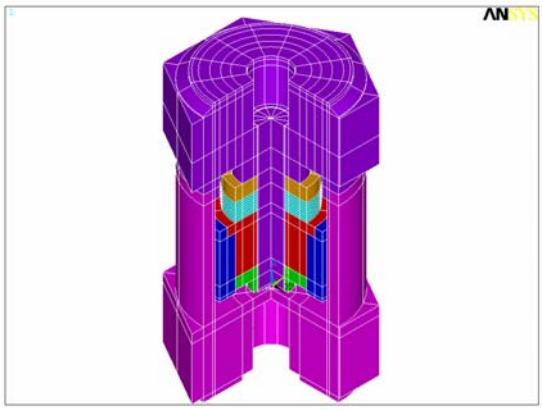

Fig. 5.5: An inverted compression design.

The structure in Fig. 5.5 is an inverted compression design. When it is mounted on the top of the structure, it becomes an upright compression design. Table 5.2 shows the comparison between the two designs.

Table 5.2: The upright and inverted compression design.

	Inverted compression design	Upright compression design
Mounted resonance frequency	22.1 kHz	38.5 kHz
Transverse resonance frequency	7.7 kHz	8.7 kHz
Charge sensitivity	0.125 pC/ms^{-2}	0.125 pC/ms^{-2}
Base bending	0.00003 ms^{-2} / $\mu\varepsilon$	0.01 ms^{-2} / $\mu\varepsilon$

It can be seen that the inverted compression design is subjected to much less base bending effect while the upright compression design has higher mounted resonance frequency.

5.2.2 Annular Shear design

Fig. 5.6 shows an Annular Shear design. The red seismic mass is fixed outside of the cyan ceramic elements. The purple part is the center post & base. There are two ways to fix the structure, using a clamping ring or soldering the seismic mass and the ceramic together. The analysis takes the soldering method.

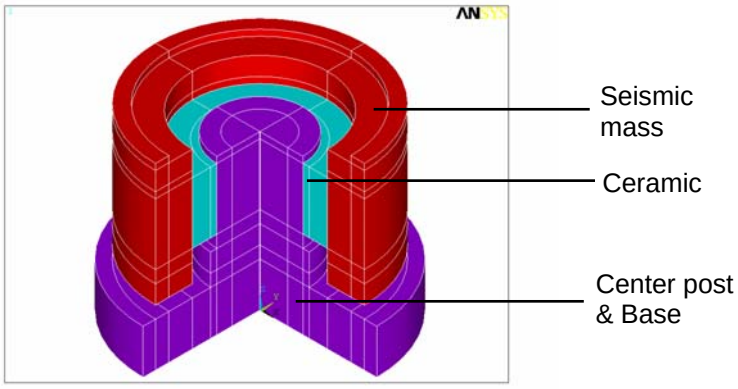

Fig. 5.6: An Annular Shear design.

Material

Table 5.3: The influence of material on the specifications.

			Center post & Base			
			Stainless Steel	Titanium	Aluminum	Tungsten
Seismic mass	Stainless Steel	[1]	1.41	1.12	1.04	1.55
		[2]	0.45	0.45	0.45	0.45
		[3]	0.65	0.65	0.65	0.65
	Tungsten	[1]	1 #	0.8	0.74	1.11
		[2]	1 #	1	1	1
		[3]	1.46	1.46	1.46	1.46

[1]: The mounted resonance frequency with Pz23.
[2]: The sensitivity with Pz23.
[3]: The sensitivity with Pz27.
#: The reference.

(1) Ceramic

Pz23 and Pz27 produce same mounted resonance frequency and same weight. It is different from the results of a compression design, in which Pz23 produces a slightly lower resonance frequency than Pz27. It is due to the totally different design principle. The sensing element of a shear design is subjected to the shear stress while the sensing element of a compression design is subjected to the compression stress.

By only changing the ceramic from Pz23 to Pz27, the sensitivity is increased to 1.46 times, which equals to the ratio between d_{15} of Pz27 and Pz23.

(2) Seismic mass

When the seismic mass is changed from tungsten to stainless steel, the mounted resonance frequency can be increased to about 1.4 times. Meanwhile, the sensitivity is reduced to 0.45 times no matter which material is used for the center post & base.

(3) Center post & Base

The center post material does not influence the sensitivity at all. It is totally different from the case of a compression design that the stiffer the center post, the lower sensitivity. It

substantiates that the shear design can hardly be influenced by the base effect because the design has already isolated the sensing element from the base efficiently.

But the center post & base influences the mounted resonance frequency very much. Taking the resonance frequency produced by stainless steel center post & base as a reference, the titanium center post & base produces 0.8 times, the aluminum one 0.74 times, and the tungsten one 1.1 times. It shows that the stiffer the center post & base, the higher the mounted resonance frequency.

According to Table 5.3, if the weight and sensitivity are not critical requirements, tungsten center post and stainless steel seismic mass can present the highest mounted resonance frequency. If both the sensitivity and the mounted resonance frequency are important, the tungsten center post and the tungsten seismic mass is the right selection.

Structure

Fig. 5.7 illustrates the component position. The position of both ceramic and seismic mass is always lower than the 0 position. Fig. 5.8 and 5.9 show the mounted resonance frequency and the sensitivity according to the ceramic position and the seismic mass position, respectively.

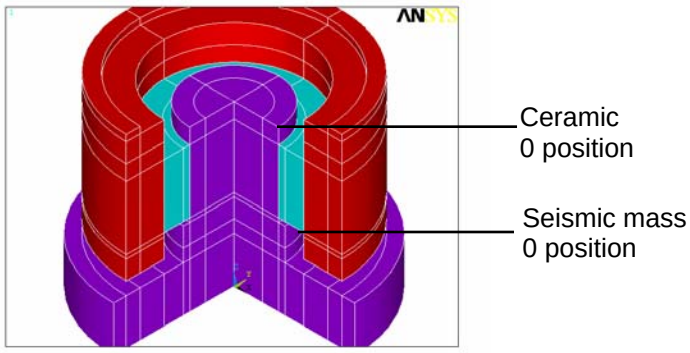

Fig. 5.7: The illustration of the component position.

In Fig. 5.8, the “ceramic position” means the distance from the 0 position. It can be seen that the lower the ceramic position, the higher the mounted resonance frequency. The ceramic position does not influence the sensitivity.

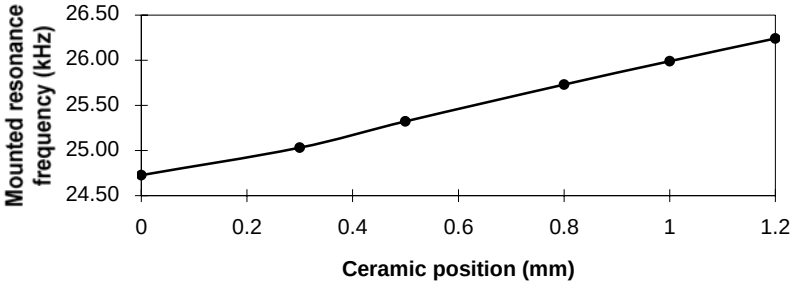

Fig. 5.8: The mounted resonance frequency as a function of ceramic position.

Fig. 5.9 shows that when the seismic mass position is higher than a certain point, the mounted resonance frequency can be improved. But the improvement is considerably small. Therefore generally the seismic mass is positioned symmetrically to the center of the ceramic height.

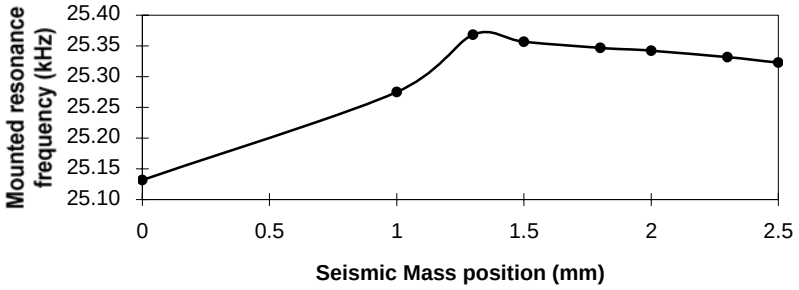

Fig.5.9: The mounted resonance frequency as a function of seismic mass position.

The mounted resonance frequency can be influenced by the thickness of the ceramic as well. Keeping the weight of the seismic mass, the thicker the ceramic, the lower the resonance frequency. It is due to the fact that the ceramic is softer than stainless steel and tungsten, which are the normal used materials for the center post and the seismic mass, respectively.

The sensitivity is not influenced by the ceramic thickness. But it does not mean that the ceramic should be made as a thin film because the thinner the ceramic, the bigger the capacitance, the higher the noise.

Table 5.4: The thickness of the ceramic.

Thickness of the ceramic	Mounted resonance frequency
0.9 mm	1.06 kHz
1 mm	1.0 kHz
1.1 mm	0.95 kHz

A full structure

There are many accelerometers designed with the Annular Shear principle. The thesis takes B & K Accelerometer Type 8325 as an example to show what kind of problem may be met.

The solid line in Fig. 5.12 shows the frequency response of the accelerometer. It can be seen that there is an undesirable peak at the frequency lower than the mounted resonance frequency. Though it is out of the usable frequency range, it will cause inaccuracy when the frequency response is calculated by the transfer function equation. Therefore the undesirable peak needs to be eliminated or moved to the upper frequency range.

After making modal analysis, it is found that the undesirable peak is induced by the resonance of the housing as shown in Fig. 5.10. Thus the solution should be to isolate the housing influence from the sensing part. Some modification analyses had been done, the detail information can be found from [5-9]. The final solution is to make a slot in the base and partly

remove mounting base as shown in Fig. 5.11. Fig. 5.12 presents the frequency response for each modification.

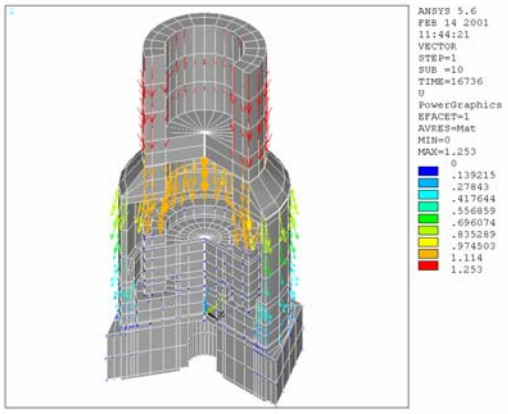

Fig. 5.10: The mode at the undesirable peak frequency.

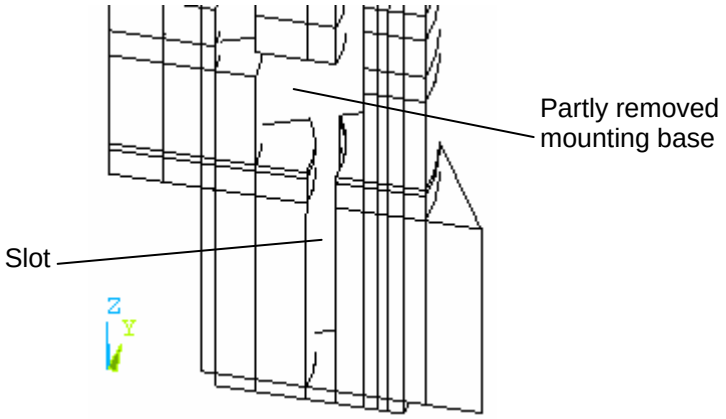

Fig. 5.11: The final solution.

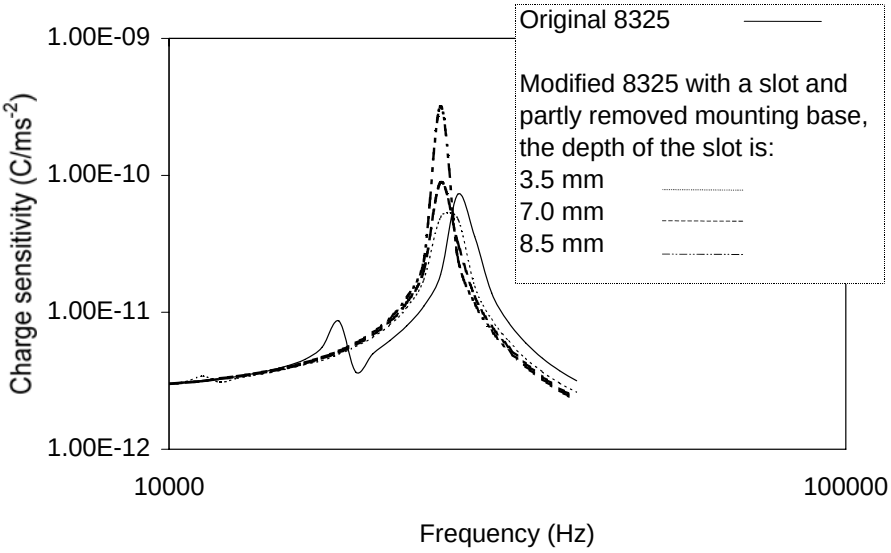

Fig. 5.12: The frequency response of each modification.

It cannot be concluded that each Annular Shear accelerometer has the same problem. But the study gives us an idea about how to solve the problem if the problem comes up.

5.2.3 DeltaShear Design

Fig. 5.13 shows a DeltaShear design. The blue clamping ring fixes three pieces of red seismic mass and three pieces of cyan ceramic elements outside of the purple triangle center post. Since the shear design has very loose coupling between the sensing elements and the base proved by the Annular Shear study, the base is not included into this analysis.

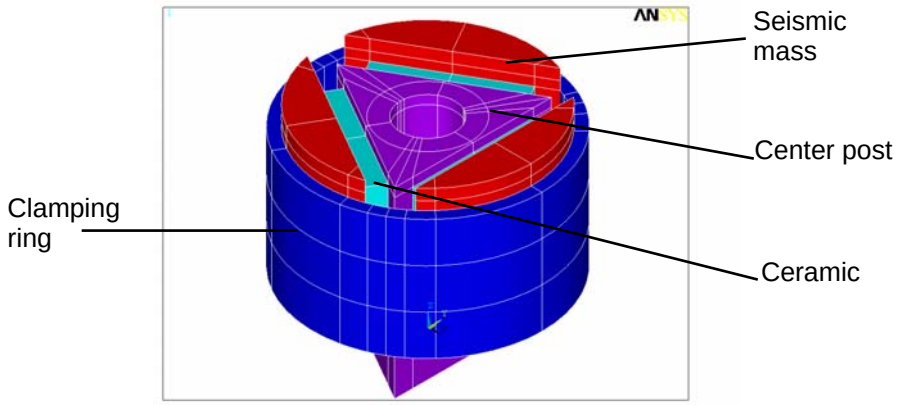

Fig. 5.13: A DeltaShear design.

Material

Table 5.5: The influence of material on the specifications.

			Center post & Base			
			Stainless Steel	Titanium	Aluminum	Tungsten
Seismic mass	Stainless Steel	[1]	1.25	0.99	0.93	1.37
		[2]	0.24	0.24	0.24	0.24
		[3]	0.36	0.36	0.36	0.36
	Tungsten	[1]	1 #	0.79	0.74	1.11
		[2]	1 #	1	1	1
		[3]	1.46	1.46	1.46	1.46

[1]: The mounted resonance frequency with Pz23.
[2]: The sensitivity with Pz23.
[3]: The sensitivity with Pz27.
#: The reference.

(1) Ceramic

Pz27 and Pz23 produce same mounted resonance frequency and same weight. The ratio between the sensitivities produced by Pz27 and Pz23 is the ratio between d_{15} of Pz27 and Pz23, which is 1.46.

(2) Seismic mass

When the seismic mass is changed from Tungsten to Stainless steel, the mounted resonance frequency can be increased to 1.25 times, the sensitivity is reduced to 0.24 times.

(3) Center post
The center post material does not influence the sensitivity. But it influences the mounted resonance frequency. The softer the center post, the lower the mounted resonance frequency.

According to Table 5.5, if the weight and sensitivity are not critical requirements, tungsten center post and stainless steel seismic mass can present the highest mounted resonance frequency. If both the sensitivity and the mounted resonance frequency are important, the tungsten center post and the tungsten seismic mass are the right selection.

Structure
Fig. 5.14 illustrates the 0 position of ceramic and the seismic mass. Fig. 5.15 and 5.16 show the mounted resonance frequency change due to the ceramic position and the seismic mass position, respectively. The position used in Fig. 5.15 and 5.16 means how much the component is moved down from the 0 position.

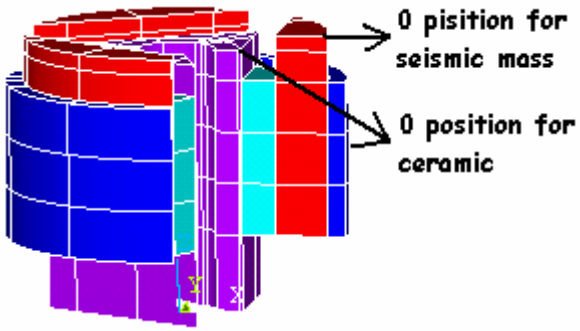

Fig. 5.14: The illustration of the ceramic position.

It can be seen from Fig. 5.15 that the lower the ceramic position, the higher the mounted resonance frequency, which is the same conclusion made for the Annular shear design.

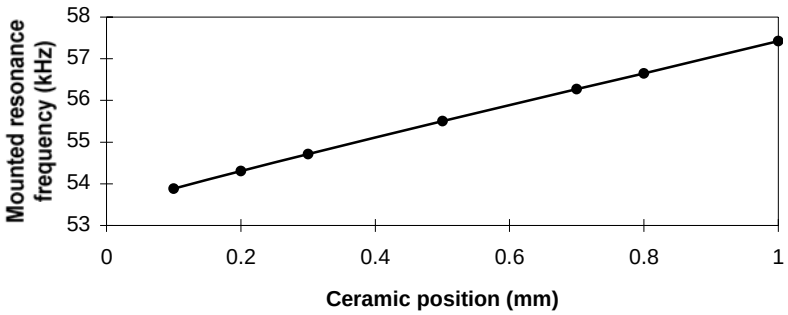

Fig. 5.15: The mounted resonance frequency as a function of ceramic position.

Fig. 5.16 shows that though the mounted resonance frequency cannot be changed much by the seismic mass position, there is a point above which the mounted resonance frequency is increased slightly. Generally the seismic mass is positioned symmetrically to the center of the ceramic height.

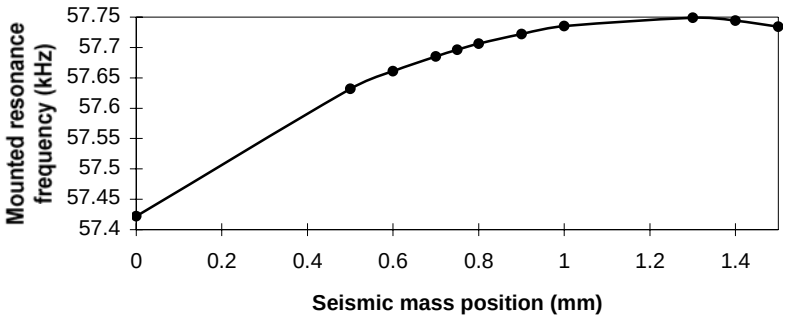

Fig.5.16: The mounted resonance frequency as a function of seismic mass position.

Keeping the weight of the seismic mass, the thinner the ceramic, the higher the resonance frequency, the bigger the noise.

Table 5.6: The thickness of the ceramic.

Thickness of the ceramic	Mounted resonance frequency
0.9 mm	1.04 kHz
1 mm	1 kHz
1.1 mm	0.96 kHz

A full structure

Since the DeltaShear is the most popular design for piezoelectric accelerometers, it is necessary to study the full structure including the influence of the housing material. B & K Accelerometer 4383 is chosen as an example. The results shown in Table 5.7 are normalized based on the existing product specifications (stainless steel housing).

Table 5.7: The housing material influence on specifications.

	Housing			
	Stainless Steel	Titanium	Aluminum	Beryllium
Mounted resonance frequency	1	0.8	0.74	1.1
Transverse resonance frequency	1	0.79	0.73	1.12
Sensitivity	1	1	1	1
Weight	1	0.7	0.56	0.49

It can be seen that the housing material does not influence the sensitivity. The titanium and aluminum housing contribute less to the weight, at the same time they produce lower mounted resonance frequency. If the price and the poisonous dust are not considered, Beryllium is the best material for the housing, which gives the highest mounted resonance frequency and the lowest weight among the common used housing material.

5.2.4 Planar Shear Design

Fig. 5.17 shows a Planar Shear design. The red seismic mass is fixed outside of the cyan ceramic elements by the blue clamping ring.

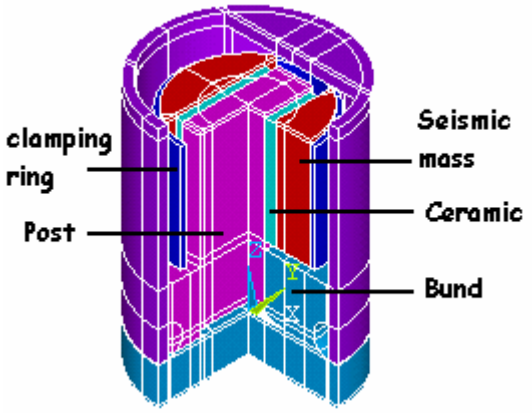

Fig. 5.17: A Planar Shear design.

Material

Table 5.8: The influence of material on the specifications.

			Center post & Base			
			Stainless Steel	Titanium	Aluminum	Tungsten
Seismic mass	Stainless Steel	[1]	1.25	0.96	0.9	1.39
		[2]	0.56	0.56	0.56	0.56
		[3]	0.81	0.81	0.81	0.81
	Tungsten	[1]	1 #	0.76	0.71	1.1
		[2]	1 #	1	1	1
		[3]	1.46	1.46	1.46	1.46

[1]: The mounted resonance frequency with Pz23.
[2]: The sensitivity with Pz23.
[3]: The sensitivity with Pz27.
#: The reference.

(1) Ceramic

Pz27 and Pz23 produce same mounted resonance frequency and same weight. The ratio between the sensitivities produced by Pz27 and Pz23 is the ratio between d_{15} of Pz27 and Pz23.

(2) Seismic mass

When the seismic mass is changed from Tungsten to stainless steel, the mounted resonance frequency can be increased to 1.25 times, the sensitivity is reduced to 0.56 times.

(3) Center post

The center post material does not influence the sensitivity. But it influences the mounted resonance frequency. The softer the center post, the lower the mounted resonance frequency.

According to Table 5.8, if the weight is not a critical requirement, tungsten center post is a good selection. With stainless steel seismic mass, it can present the highest mounted resonance frequency; with tungsten seismic mass, it can present the highest sensitivity.

A full structure

Planar Shear accelerometer has very serious contact problem. As shown in Fig. 5.18(a), the pink part is the stainless steel center post; the light blue one is the beryllium bottom. The housing is made by inconel, which is purple. The configuration of the structure is that the center post is inserted into the bottom first, then the bottom is clamped by the stiff housing.

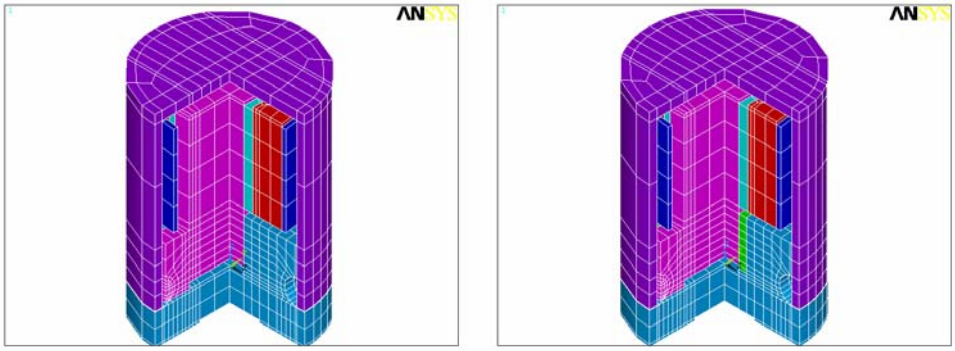

(a) (b)

Fig. 5.18: Contact consideration of Planar Shear accelerometers.

Practically the center post may not connect with the bottom very well because of every possible factor. The green part in Fig. 5.18(b) is an assumed material that is softer than the beryllium to present the not-good contact. The influence of the not-good contact on the specifications is shown in Table 5.9. It shows that the connection of the center post and the bottom is the dominating factor for the resonance frequency.

Table 5.9: The resonance frequency.

	Perfect contact	Not-good contact	Measured
Transverse resonance frequency	27.3 kHz	16.8 kHz	21 kHz
Mounted resonance frequency	128 kHz	86.6 kHz	85 kHz

Because there is only one existing Planar Shear accelerometer so far, based on the analysis made on it, we can say that the contact problem should be considered seriously. The solution might be soldering the central post and the bottom in order to achieve much better contact surface between the two components.

5.2.5 ThetaShear Design

Fig. 5.19 shows a ThetaShear design. The red seismic mass is fixed outside of the cyan ceramic elements.

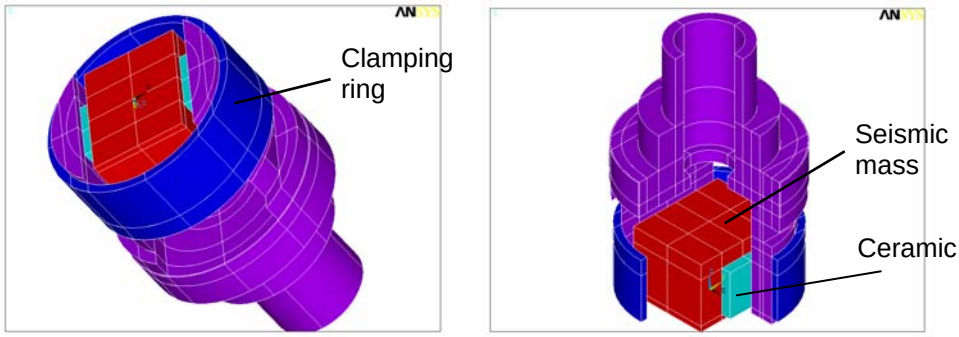

Fig. 5.19: A ThetaShear design.

Material

Table 5.10: The influence of the material on the specifications.

			Center post		
			Stainless steel	Titanium	Aluminum
Seismic mass	Stainless steel	[1]	1.43	1.19	1.12
		[2]	0.46	0.46	0.46
		[3]	0.67	0.67	0.67
	Tungsten	[1]	1 #	0.83	0.78
		[2]	1 #	1	1
		[3]	1.46	1.46	1.46

[1]: The mounted resonance frequency with Pz23.
[2]: The sensitivity with Pz23.
[3]: The sensitivity with Pz27.
#: The reference.

(1) Ceramic
Pz23 and Pz27 produce same mounted resonance frequency and same weight. The sensitivity produced by Pz27 is 1.46 times the sensitivity produced by Pz23.

(2) Seismic mass
When the seismic mass is changed from Tungsten to Stainless steel, the mounted resonance frequency can be increased to 1.43 times. The sensitivity is reduced to 0.46 times.

(3) Center post
The center post material does not influence the sensitivity at all. But it influences the mounted resonance frequency. The stiffer the center post, the higher the mounted resonance frequency.

It can be concluded that the stainless steel center post and seismic mass are good selection for high resonance frequency. Tungsten seismic mass and the stainless steel center post are a compromised choice for both mounted resonance frequency and sensitivity.

Structure

(1) Arm-cut

There is a cut in the arm as shown in Fig. 5.20 to make the structure more flexible. But how big the effect of the cut is has not been analyzed experimentally. With a virtual prototype, it can be seen that after filling up the cut, the resonance frequency is increased a little from 18.9 kHz to 20.1 kHz and from 36.1 kHz to 36.5 kHz for the transverse and mounted resonance frequency, respectively. The sensitivity stays the same.

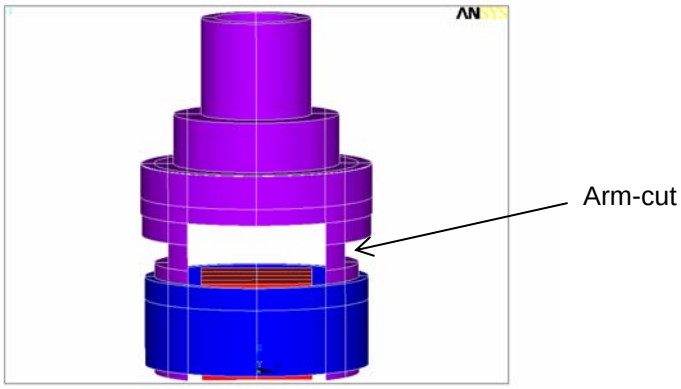

Fig. 5.20: The cut in the arm.

(2) Ceramic

The original ceramic is as shown in Fig. 5.21(a). Under the situation shown in Fig. 5.21(b), the resonance frequency is increased from 18.9 kHz to 21.6 kHz and from 36.1 kHz to 40.7 kHz for the transverse and mounted resonance frequency, respectively. Under the situation shown in Fig. 5.21(c), the resonance frequency is increased from 18.9 kHz to 21.8 kHz and from 36.1 kHz to 41.7 kHz for the transverse and mounted resonance frequency, respectively. The sensitivity stays the same.

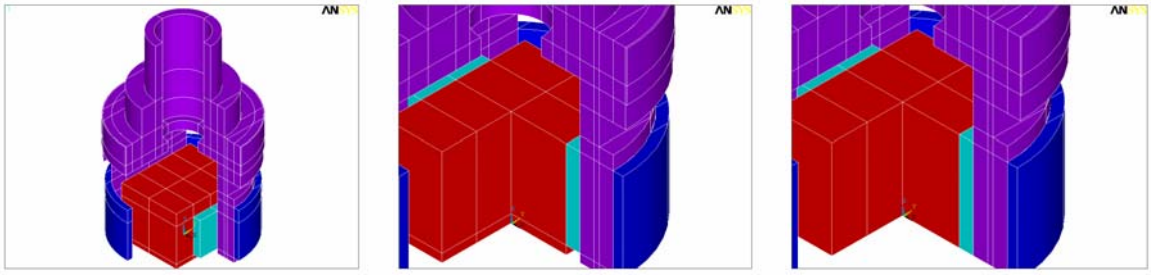

(a) (b) (c)

Fig. 5.21: The changed ceramic dimension.

The virtual prototype study shows that it is not necessary to keep the arm-cut, and the ceramic should be as high as the seismic mass in order to increase the usable frequency range.

A full structure

Cable influence cannot be avoided for any accelerometer. Chapter 4 had shown the cable influence on OrthoShear® accelerometer. The influence effects at the very low frequency

range, between 40 Hz to 50 Hz. The cable influence on ThetaShear accelerometer happens around 40 Hz. By using a clip to fix the cable, the influence can be minimized. As shown in Fig. 5.22, when the cable is fixed but further to the housing, the cable influence peak is moved up to the higher frequency range, when the cable is fixed and very close to the housing, the cable influence can be eliminated. In fact, the clip-method can be used to any accelerometer to avoid the cable influence as long as we make slots for the housing.

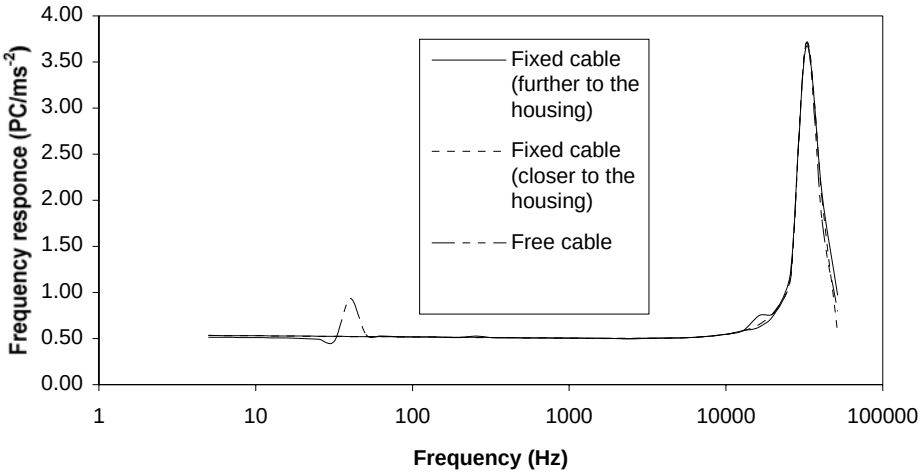

Fig. 5.22: The cable influence on the ThetaShear accelerometer.

5.2.6 OrthoShear® Design

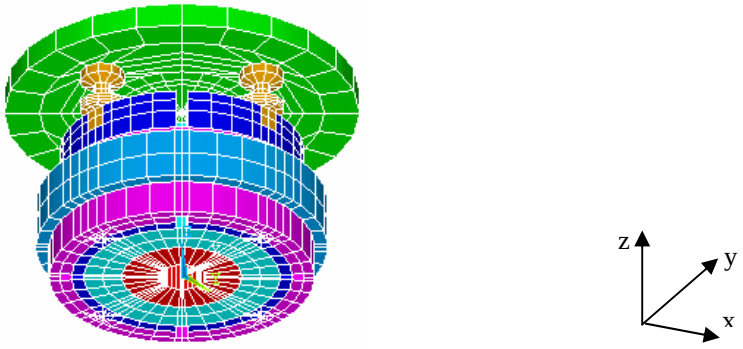

Fig. 5.23: An OrthoShear® design.

Fig. 5.23 shows an OrthoShear® design. A detailed description can be found in Section 4.2.1. The structure is so unique that a full virtual prototype of the only OrthoShear® accelerometer, B & K Type 4506, is analyzed.

Material

Before starting the analysis, let's list the original materials used first. They are Pz23 for ceramic, Tungsten for seismic mass, brass for hinges, and titanium for the housing. Table 5.11

shows the influence of the material on the specifications. During the analyzing, only the material of the certain component listed in the first column is changed.

Table 5.11: The influence of the material on the specifications.

Component	Material	Charge sensitivity (pC/ms^{-2})		Mounted resonance frequency (kHz)		Weight (gram)
		x-, y-axis	z-axis	x-, y-axis	z-axis	
Ceramic	PZ23 *	1.54	0.92	10.4	21.7	15.0
	PZ27	1.98	1.18	10.4	21.7	15.0
Seismic mass	Tungsten *	1.54	0.92	10.4	21.7	/
	Stainless steel	1.23	0.55	11.6	24.1	/
Hinges	Brass *	1.54	0.92	10.4	21.7	/
	Stainless steel	1.54	0.92	12.4	24.9	/
	Berylco	1.54	0.92	11.5	23.5	/
Housing	Titanium *	1.54	0.92	10.4	21.7	15.0
	Stainless steel	1.54	0.92	10.9	23.4	22.7
	Aluminum	1.54	0.92	10.3	21.4	10.9
	Beryllium	1.54	0.92	11.0	24.1	9.0

*: The original material used.

(1) Ceramic

Pz27 and Pz23 produce the same mounted resonance frequency and the same weight. The ratio between the d_{15} of Pz27 and Pz23 is 1.46. But the sensitivity produced by Pz27 is 1.28 times the one produced by Pz23. It means that the sensitivity of the OrthoShear® structure is not only determined by d_{15} and the seismic mass, but also determined by other components contributing to the active seismic mass.

(2) Seismic mass

The stainless steel seismic mass gives lower sensitivity and higher mounted resonance frequency. It can be seen that the z-axis sensitivity is decreased 41% while the x-, y-axis sensitivity is decreased 20%. The mounted resonance frequency is increased 11%.

(3) Hinges

The hinges are key components for the design because they act as the most flexible spring of the structure. The original hinges are made by brass and glued with the thick film. The hinges are liable to be damaged by being subject to large shock. In order to make the hinges more durable, nuts can be used to fix the hinges to the thick film. The usage of nuts requires the hinge material be able to stand with large yield stress.

The stress intensity distribution of the hinge with different material is shown in Fig. 5.24.

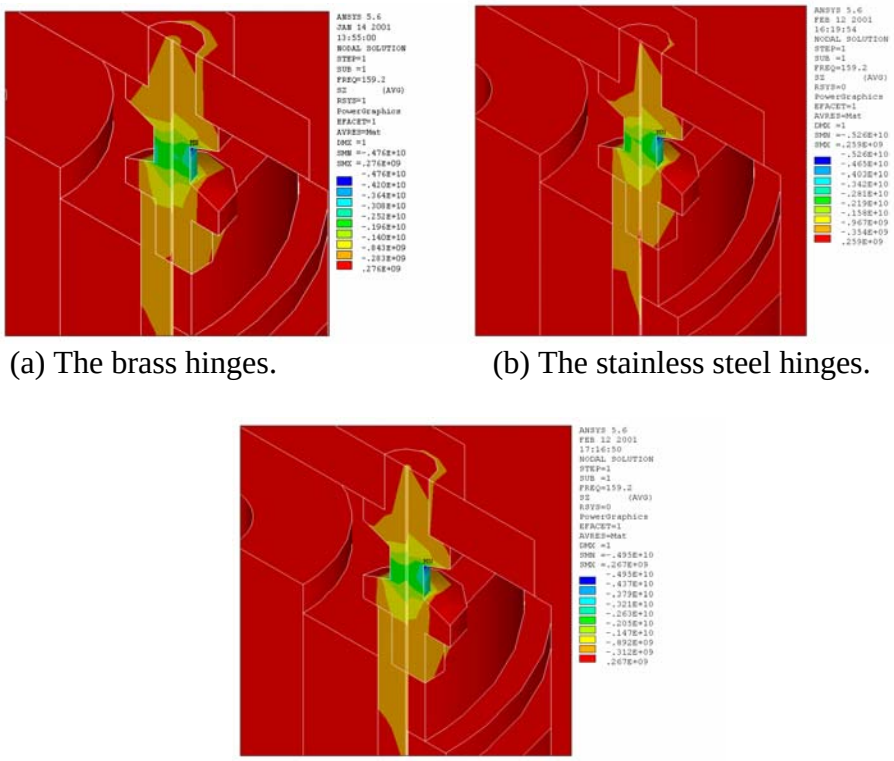

(a) The brass hinges. (b) The stainless steel hinges.

(c) The Berylco hinges.

Fig. 5.24: The stress intensity distribution with different hinge material.

The larger the stress distribution in the connection area of the hinge and the thick film, the easier the hinge falls apart from the thick film. Fig. 5.24 shows that the stainless steel hinge has the lowest stress distribution at the connection area, the brass hinge has the largest stress distribution. It shows that the structure with stainless steel hinges should be more durable than the one with brass or Berylco hinges. But due to the fact that the stainless steel can subject smaller yield stress than Berylco, Berylco is a better choice for the hinges than the stainless steel and the brass.

Because of the use of Berylco for the hinges, the system stiffness is increased. Therefore the mounted resonance frequencies are increased as well.

Compared to the actually used brass hinges, by using the stainless steel hinges the x-, y- and z-axis mounted resonance frequency increase 19% and 14.7%, respectively; by using the Berylco hinges the x-, y- and z-axis mounted resonance frequency increase 10.6% and 8.3%, respectively.

The material of the hinges does not change the sensitivity.

(4) Housing

The housing material does not influence the x-, y- and z-axis sensitivity. The influence on the mounted resonance frequency can be neglected as well. The main influence is acting on the weight. Compared to the actual used titanium housing, the weight is increased 51% by using

stainless steel housing, and decreased 27.3% and 40% by using Aluminum and Berylco housing, respectively.

Structure

Table 5.12: The influence of the structure change on the specifications.

Component		Charge sensitivity (pC/ms^{-2})		Mounted resonance frequency (kHz)	
		x-, y-axis	z-axis	x-, y-axis	z-axis
Clamping ring & insulating ring	With (actual)	1.54	0.92	10.4	21.7
	Without	1.39	0.92	11.	23.1
Seismic mass inner diameter	2 mm (actual)	1.54	0.92	10.4	21.7
	0 mm	1.66	1.05	10.1	21.
Arm gap	2°	1.55	0.92	10.4	21.7
	6° (actual)	1.54	0.92	10.4	21.7
	20°	1.49	0.93	10.5	22.
Thickness of the thick film	0.5 mm	1.54	0.92	10.	19.
	1.0 mm (actual)	1.54	0.92	10.4	21.7

(1) Clamping ring & insulating ring

The clamping ring is used to clamp the seismic mass, ceramic and the arm. The insulating ring is used to insulate the stainless steel arm from the inconel clamping ring. When the seismic mass, the ceramic and the arm are soldered in position, the z-axis charge sensitivity stays the same while the x-, y-axis sensitivity is decreased 10%. It is because that the clamping ring & insulating ring act as part of the active seismic mass for x-, y-axis sensitivity, but not for z-axis sensitivity. The resonance frequencies are increased because the mass is reduced.

(2) Seismic mass

The seismic mass dominates the sensitivity. In this part, the maximum sensitivity by using the biggest seismic mass is estimated. The corresponding resonance frequency is estimated as well, which is more important than the sensitivity estimation.

The actually used inner diameter of the seismic mass is 2 mm. When the hole of the seismic mass is filled, the resonance frequency is reduced 3% while the sensitivity is increased 7.8%, 7.8% and 14.1% for the x-, y- and z-axis, respectively.

Besides filling the hole of the seismic mass, increasing the height of the housing to add more seismic mass can increase the sensitivity as well. From this point of view, there is no sensitivity limitation at all. But from a practical point of view, it is not meaningful. Fig. 5.25 illustrates the idea.

(3) Arm gap

The arm is used to fix the hinges and collect the induced charges. The arm gap is illustrated with Fig. 5.26. It can be seen that the arm gap does not influence the resonance frequency very much. As for the sensitivity, the x-, y-axis sensitivity is reduced from 1.55 pC/ms^{-2} to 1.49 pC/ms^{-2} when the arm gap is increased from 2° to 20°. It is because the arm is part of the active seismic mass for x-, y-axis sensitivity, but not for z-axis sensitivity.

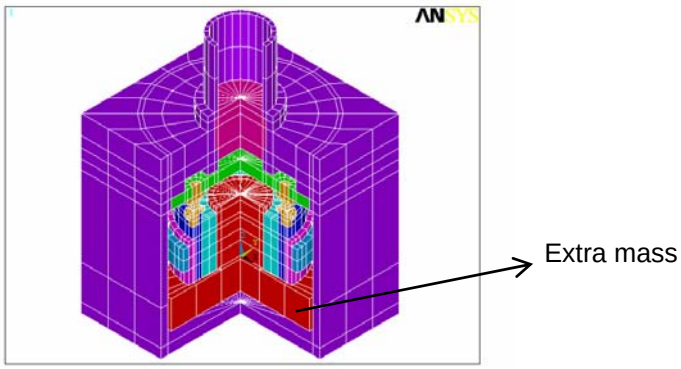

Fig. 5.25: The increased seismic mass.

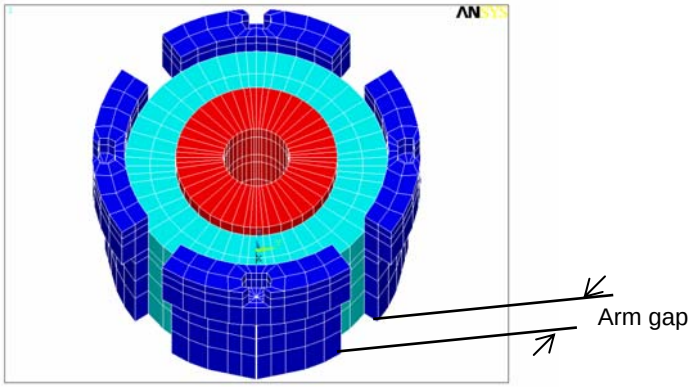

Fig. 5.26: The arm gap.

(4) Thickness of the thick film

The thickness of the thick film does not influence the sensitivity, but it does increase the resonance frequency when it is increased. This is due to the fact that the thicker the thick film, the stiffer the structure. But there is a problem with drilling holes through a thick film if its thickness is beyond a certain limitation. Therefore the conclusion is selecting the thickest thick film as long as the drilling problem does not come up.

Mounting glue influence

When we measure the mounted resonance frequency of Type 4506, a stainless steel adapter is used. The accelerometer under test is mounted on one side of the adapter, another one is mounted on the other side in order to balance the system as shown in Fig. 5.27.

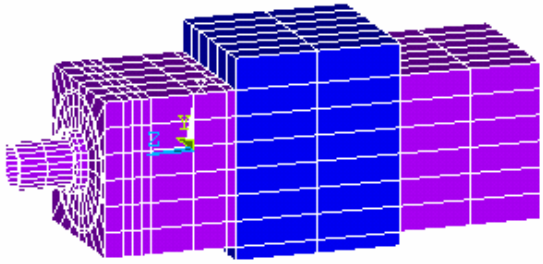

Fig. 5.27: The set-up for Type 4506 measurement.

The measured results can vary considerably because they depend heavily on the way to mount the accelerometer. The mounting glue acts as a spring connecting the adapter surface and the accelerometer surface. Therefore the stiffness of the glue is a key factor influencing the measured results. Though it is difficult to analyze the glue influence experimentally, the analysis can be done by using virtual prototype. The results are shown in Table 5.13. “Perfect mounted” means the accelerometer and the adapter are inherently connected without using any glue. “Thickness of the glue” means the thickness of the glue between the accelerometer and the adapter. Table 5.14 presents the properties of different types of glue.

Table 5.13: The mounting glue influence on the mounted resonance frequency.

Thickness of the glue		Mounted resonance frequency x-, y-axis	Mounted resonance frequency z-axis
Perfect Mounted		10.4 kHz	21.5 kHz
Soft glue	0.1 mm	3.4 kHz	11.8 kHz
	0.2 mm	2.5 kHz	10.9 kHz
Stiff glue	0.1 mm	9.8 kHz	21.4 kHz
	0.2 mm	9.9 kHz	20.8 kHz

Table 5.14: The properties of different kinds of glue.

	Density (kg/m^3)	Young’s modulus (N/m^2)	Poisson’s ratio
Soft glue	1080	0.9×10^7	0.49
Stiff glue	1610	6.86×10^9	0.32

Table 5.13 shows that both the glue stiffness and the glue thickness influence the z-axis properties much less than the x-, y-axis properties. The reason is that when z-axis properties are calculated, the glue acts as a spring in series with other components, when x-, y-axis properties are considered, the glue acts as a spring parallel to other components. Therefore the glue influence on the x-, y-axis properties is bigger than that on the z-axis properties.

The results show that we should choose stiff glue and make the glue layer as thin as possible. In fact, the conclusion is well known. But before we can only make qualitative analysis, now we can make both qualitative and quantitative analysis.

5.3 Comparison between designs

All properties discussed in this section are common properties for each design. Any particular properties are not concerned.

5.3.1 Material

According to the results presented in Section 5.2, a small conclusion can be made about the material influence on the specifications for each design.

By only changing ceramic from Pz23 to Pz27, the resonance frequency and the weight does not change for each design. The sensitivity for all shear designs is increased to 1.46 times. It

can be explained that with the same m_s, according to $S_q = d_{15} \cdot m_s$, the sensitivity is determined by the d_{15} of ceramic. The ration between the d_{15} of Pz27 and Pz23 is 1.46. For a compression design, the sensitivity is supposed to be increased to 1.29 times according to $S_q = d_{33} \cdot m_s$. But the fact is that the sensitivity is increase to 1.32 times. This is due to that fact that the sensitivity of a compression design does not only determined by the d_{33} and the seismic mass, but also determined by the stress acting on the ceramic.

By changing seismic mass from tungsten to stainless steel, the mounted resonance frequency of the Compression design is increased to 1.32 times, the Annular shear design to 1.41 times, the DeltaShear design to 1.25 times, the Planar Shear design to 1.25 times, and the ThetaShear design to 1.43 times. The reason for the resonance frequency increasing is that the mass is reduced because of the use of the light material for seismic mass.

By changing seismic mass from tungsten to stainless steel, the sensitivity is 0.5 times for the Compression design, 0.45 times for the Annular shear design, 0.24 times for the DeltaShear design, 0.56 times for the Planar shear design, 0.46 times for the ThetaShear design. The reason for the sensitivity decreasing is that the seismic mass is reduced.

5.3.2 Structure

Though the reducing of the ceramic thickness can increase the mounted resonance frequency without influencing the sensitivity for both Compression and shear designs, it does not mean that the thickness should be unlimitedly thin because the thinner the ceramic, the bigger the capacitance, the bigger the noise.

For shear design, the seismic mass could increase the mounted resonance frequency by being positioned higher. But since the center gravity of the whole structure has to be as low as possible, the seismic mass is suggested to be positioned symmetrically to the center of the ceramic height.

5.3.3 Comparable comparison

So far it is still unfair to conclude which design has the highest sensitivity or the highest mounted resonance frequency because the seismic mass of each design does not have the same weight, which means the designs analyzed in last section are not comparable. In this section, we are going to scale the virtual prototypes in order to let them have the same seismic mass. ThetaShear accelerometer 4508 is regarded as the reference.

Full structures are used. Materials used by each physical product are used for the virtual prototype. It means that the material of the same component may not be same for different designs.

Charge sensitivity

The seismic mass had been scaled to have same weight. Based on $S_q = d_{15} \cdot m_s$, the charge sensitivity should be 0.41 pC/ms^{-2}. But Table 5.15 shows that no sensitivity is the same as the theoretical value. It is because in different designs the m_s does not only consist of the seismic mass, but also consist of other components.

Table 5.15: Comparison between the scaled virtual prototypes.

		Charge sensitivity	Mounted resonance frequency	Base bending effect	Weight
Compression design (8305)	Upright	0.07 pC/ms^{-2}	46.5 kHz	0.01 $ms^{-2}/\mu\varepsilon$	23.5 gram
	Inverted	0.07 pC/ms^{-2}	26.7 kHz	0.0003 $ms^{-2}/\mu\varepsilon$	23.5 gram
Annular Shear design (8325)		0.58 pC/ms^{-2}	58 kHz	0.0005 $ms^{-2}/\mu\varepsilon$	13.4 gram
DeltaShear design (4384)		0.9 pC/ms^{-2}	52.4 kHz	0.01 $ms^{-2}/\mu\varepsilon$	10.1 gram
Planar Shear design (4374)		0.6 pC/ms^{-2}	51 kHz	0.002 $ms^{-2}/\mu\varepsilon$	3.8 gram
ThetaShear design (4508)		0.52 pC/ms^{-2}	36 kHz	0.002 $ms^{-2}/\mu\varepsilon$	4.8 gram

For the ThetaShear design shown in Fig. 5.19, the m_s consists of the seismic mass and half ceramic. For the Annular shear design, the m_s has the seismic mass, the thick film (preamplifier) and half ceramic. For a Planar Shear design, the m_s has the seismic mass, the clamping ring and half ceramic. For a DeltaShear design, the m_s consists of the seismic mass, the clamping ring and half ceramic. This is why the DeltaShear design has the highest sensitivity after the seismic mass is normalized.

Mounted resonance frequency
After normalizing the seismic mass, the Annular shear design has the highest mounted resonance frequency, which can be up to 58 kHz. ThetaShear design has the lowest mounted resonance frequency as 36 kHz.

Base bending effect
After normalizing the seismic mass, the Upright compression design and the DeltaShear design has the biggest base bending effect while the Annular shear design and the Inverted compression design have the smallest one. The conclusion that the DeltaShear design has the biggest base bending effect can be a surprise. Further analysis needs to be done.

Weight
The Planar shear design is the lightest, 3.8gram. Compression design is 23.5gram, which is the heaviest.

5.4 Conclusion

The work described in this chapter gives us insights into piezoelectric accelerometer designs. With detailed analysis of each design, the influence of the material and structure change on the specifications are quantified.

The results obtained with virtual prototypes show that with same seismic mass: (1) DeltaShear design has the highest sensitivity due to the contribution from the other components to the active seismic mass; (2) Annular Shear design has the highest mounted resonance frequency;

(3) the Upright compression design has the biggest base bending effect; (4) the Planar shear design is the lightest.

The next chapter will present how the virtual prototypes work together with the improved scientific understanding to make new designs.

References

5-1 Hansen, Knud Styhr, "A New Design Principle for Triaxial Piezoelectric Accelerometers", Technical Review, Bruel & Kjaer, No. 1, 1997

5-2 Hansen, Knud Styhr, Patent, WO97/1496997.4.24

5-3 Bruel & Kjaer, "Transducer & Conditioning Catalogue 1997", Denmark

5-4 http://www.endevco.com

5-5 http://www.kistler.com

5-6 http://www.pcb.com

5-7 "ANSYS Manual"

5-8 Mark SMark Serridge, Torben R. Licht, "Piezoelectric Accelerometer and Vibration Preamplifier Handbook", Bruel & Kjaer, 1987, Denmark

5-9 B. Liu, B. Kriegbaum, " Piezoelectric Accelerometers Modification Based on the Finite Element Method", International Journal of Acoustics and Vibration, Feb. 2000, Volume 5, Number 3

6
New Designs of The Piezoelectric Accelerometer

6.1 Introduction

Traditionally when a new design is going to be made, an analytical model is needed first to get a rough estimation on the specifications. Afterwards a physical prototype was made at workshop. The first prototype usually could not hit the requirements. Therefore, a modified one has to be made. In general at least three versions of physical prototype are needed.

This chapter is going to present a more advanced method to make new designs. The method is to use virtual prototypes with the aid of the information presented in Chapter 5.

Two new designs are presented in this chapter. The first one is based on Annular Shear design. The second one is based on OrthoShear® design. For each design, the requirements, design procedure, experimental verification and detailed analysis are presented step by step.

6.2 Center-bolt Annular Shear accelerometer

6.2.1 Requirement

This accelerometer will be installed on the helicopter transmission Main Gear-Box as well as Intermediate Gear-Box and Tail Gear-Box, continuously sensing the gear box housing vibration. The output signal from the accelerometer should have a voltage proportional to the instantaneous transmission vibration. The sensitivity should be 10 $mV/g \pm 5\%$. Mounted resonance frequency should exceed 40 kHz, when measured with the accelerometer properly installed. In addition to these requirements, the new accelerometer should have a built-in DeltaTron® charge amplifier with IS and complies with IEEE-P1451.1 standard. The design of the amplifier is beyond the thesis.

In short, the following requirements must be fulfilled.
(1) The mounted resonance frequency should exceed 40 kHz.
(2) The sensitivity should be higher than 10 $mV/g \pm 5\%$.
(3) The weight should be less than 100 gram.
(4) The accelerometer should be able to work at all direction.
(5) The accelerometer should have a side-connector.

6.2.2 Design procedure

First, due to the application, one axial accelerometer is suitable. Second, since the accelerometer should be workable at all direction, and have a side-connector, Annular Shear with a center bolt can be the best selection regarding to mounting concern. This is the reason why the design is called Center-bolt Annular Shear design.

For normal Annular Shear Design, the piezoelectric element and the seismic mass are formed into rings and mounted around a center post. All elements are held in position using mechanical pre-loading. In this case, due to the commercial reason, the three elements are soldered together.

Another consideration is that the accelerometer will stay in a helicopter permanently. Therefore the accelerometer has to be able to protect itself from the influence of high and/or low frequency signals. The solution is that the accelerometer should have insulated and double-shielded case. Insulated case can break the ground loop while double-shielded case can prevent radiated electromagnetic interference (EMI) to disturb the vibration signal in the built-in charge amplifier. The housing can act as the outside case to shield against high frequencies (>100 kHz), usually radio frequencies. The inner case is needed to shield the accelerometer from low frequency, such as the 400 Hz electrical alternator frequency.

The detailed analysis of Annular Shear design presented in the last chapter shows that in order to obtain high mounted resonance frequency, the ceramic should be positioned as low as possible. The position of the seismic mass should be balanced according to the center of the ceramic height.

The detailed analysis also shows that:

(1) Pz27 has higher dielectric constant, higher charge coefficients and higher electromechanical coupling coefficients than Pz23. But it has lower temperature stability than Pz23. Since the accelerometer is going to stay in a helicopter permanently, the temperature stability is important. Therefore Pz23 is chosen as the sensing element.
(2) Stainless steel housing can make the structure stiff to against the environmental effects. It can give the highest resonance frequency as well.
(3) Tungsten seismic mass can produce the highest sensitivity.
(4) Tungsten center post can give the highest resonance frequency if the weight is not a critical requirement.

Based on what are recommended above, the materials used for the design are listed in Table 6.1.

Table 6.1: The materials used for the design.

Component	Material
Ceramic	Pz23
Seismic mass	Tungsten
Center post	Tungsten
Housing	Stainless steel
Inner shield	Brass

The first virtual prototype is shown in Fig. 6.1. It is used to estimate if the requirements of the mounted resonance frequency and the sensitivity can be fulfilled. Therefore the inner case is not included. The prototype has cyan sensing element, red seismic mass, pink housing, blue central post, and purple thick film.

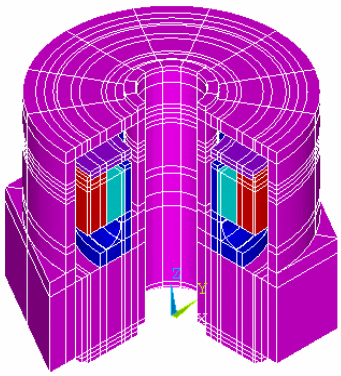

Fig. 6.1: The first virtual prototype.

The sensitivity of the first virtual prototype is 1.56 pC/ms^{-2}, the mounted resonance frequency is 49.5 kHz, and the transverse resonance frequency is 23.3 kHz. The weight is 58 gram. It can be seen that the design can fulfill the basic requirements, which means that both the design principle and the material selection are correct.

In order to prevent the accelerometer from the low frequency signal influence, an inner shield is needed. According to this concern, we came up with the second virtual prototype shown in Fig. 6.2. This prototype has an orange component made by brass acting as the inner shield. The shape of the mechanical unit is changed to cylinder in order to make the installation easier.

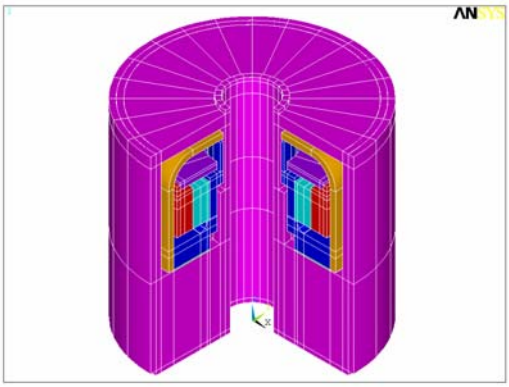

Fig. 6.2: The second virtual prototype.

From Fig. 6.2, it can be seen that the inner wall of the housing does not have even thickness. The reason to do so is that on one hand we want to keep the weight as low as possible, which means the inner wall should not be thick; on the other hand, a thin wall may not be able to stand under large stress. Therefore the un-even wall is a compromise. Consequently the shape of the center post is not regular as well. From a manufacture point of view, the two components will cause difficulties. In order to void the difficulties, the third virtual prototype as shown in Fig. 6.3 has a straight center post.

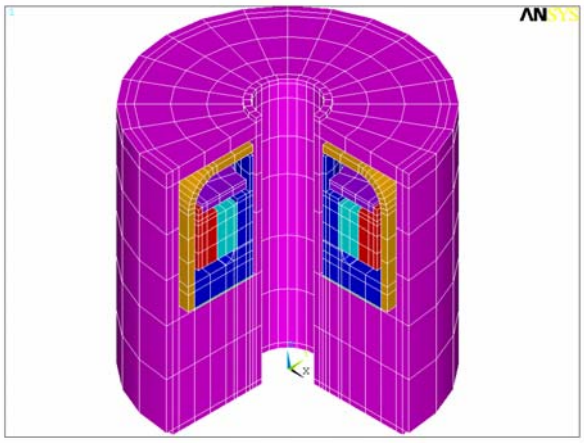

Fig. 6.3: The third virtual prototype.

The stress intensity distributions of the second and third prototype are shown in Fig. 6.4. It can be seen that for the second prototype, the inner wall of the housing has even stress intensity distribution; for the third prototype, the lower part of the inner wall of the housing has larger stress intensity distribution than the upper part. The figures on the right side of Fig. 6.4(a), (b) show that the thin housing inner wall is still workable.

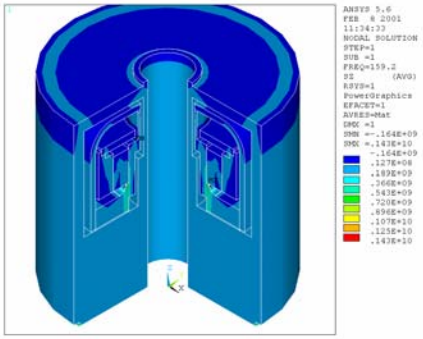

(a) The second prototype.

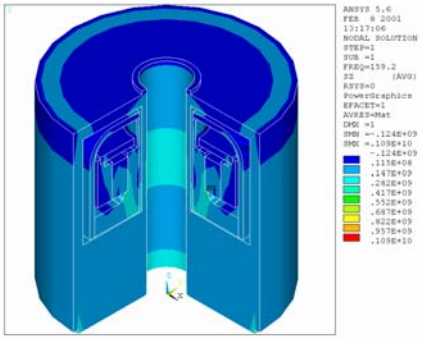

(b) The third prototype.

Fig. 6.4: Stress intensity distribution.

Since the accelerometer is going to use a center bolt, the analysis of the prototype with a center bolt cannot be omitted. Within the virtual prototype, the bolt connects the top of the housing while it does not connect the inner wall of the housing because in practice the thread of the bolt cannot provide a good connection. Calculation results listed in Table 6.2 shows that when the center bolt is used as shown in Fig. 6.5, the specifications do not change very much.

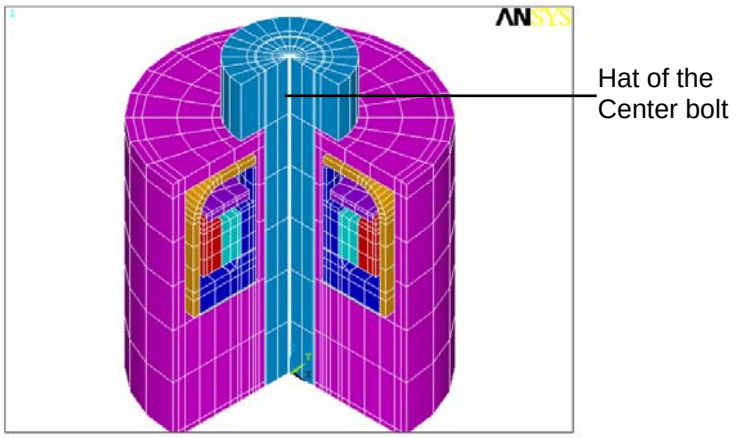

Fig. 6.5: The prototype with a center bolt.

Table 6.2: The specifications of the virtual prototypes.

	Mounted resonance frequency (kHz)	Transverse resonance frequency (kHz)	Charge sensitivity (pC/ms^{-2})	Size (mm)	Weight (gram)
Prototype 1	49.5	23.3	1.56	15.8 (height) 17 (diameter)	58
Prototype 2	42.7	24.9	1.56	18.5 (height) 19.1 (diameter)	36.
Prototype 3	43.4	25.2	1.45	18.4 (height) 19.1 (diameter)	37.1
Prototype 3 With center-bolt	43.8	24.8	1.45		

It can be seen that the mounted resonance frequency of the prototype 1 is the highest. It is because that in prototype 1 the thick film connects the seismic mass perfectly while in the prototype 2 and 3 the thick film is glued to the seismic mass. The glue influence will be described in Section 6.2.4.

6.2.3 Experimental verification

A comparison between the virtual and physical prototype is given in Table 6.3. It shows that the results match well.

Table 6.3: Comparison between the virtual and physical prototypes.

Specification	Virtual prototype	Physical prototype	Deviation
Charge sensitivity (pC/ms^{-2})	1.45	1.4	3.6%
Mounted resonance frequency (Hz)	43.4	41	5.9%

The sensitivity compared in Table 6.3 is charge sensitivity instead of voltage sensitivity. It is due to the fact that though both physical and virtual prototypes have built-in preamplifier, the virtual prototype treats it as a mechanical part instead of an electrical part, which means the output is charge. Therefore it is fair to compare the charge sensitivity.

6.2.4 Detailed analysis

Bolt influence

As shown in Fig. 6.5, a stainless steel bolt is used to mount the accelerometer. In practice the surfaces of the bolt and the housing may not contact perfectly because of dust or any other reasons. The mounted resonance frequencies under different conditions are shown in Table 6.4. "Loose connection with bolt" means that a soft material that is 0.01mm thick fills the gap between the bolt and the housing.

Table 6.4: The bolt influence on the resonance frequency.

	Mounted resonance frequency	Transverse resonance frequency
Without bolt	43.4 kHz	25.2 kHz
Perfect connection with bolt	43.8 kHz	24.8 kHz
Loose connection with bolt	43.7 kHz	24.1 kHz

It can be seen that the usage of the center bolt increases the resonance frequency slightly. It is because the bolt increases the stiffness of the whole structure. The loose connection reduces the transverse resonance frequency because the loose connection makes the structure less stiff along the transverse direction than when the connection is good.

Fig. 6.6 shows the influence of the hat of the bolt. The hat means the top part of the bolt illustrated in Fig. 6.5. It can be big or small. Fig. 6.6 presents that the hat does not change the frequency response within the usable frequency range.

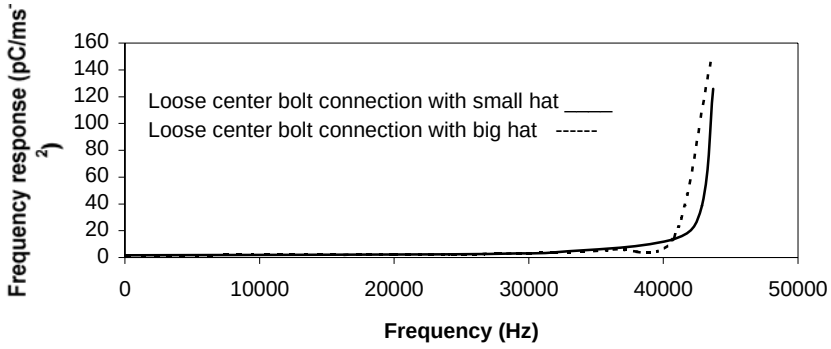

Fig. 6.6: The frequency response under different conditions.

Glue influence

The preamplifier (thick film) is glued to the seismic mass as illustrated in Fig. 6.7. Table 6.5 shows that with 0.05 mm thick glue (in practice this is the thinnest), the mounted resonance frequency is reduced from 47.6 kHz to 43.4 kHz while the transverse resonance frequency keeps constant.

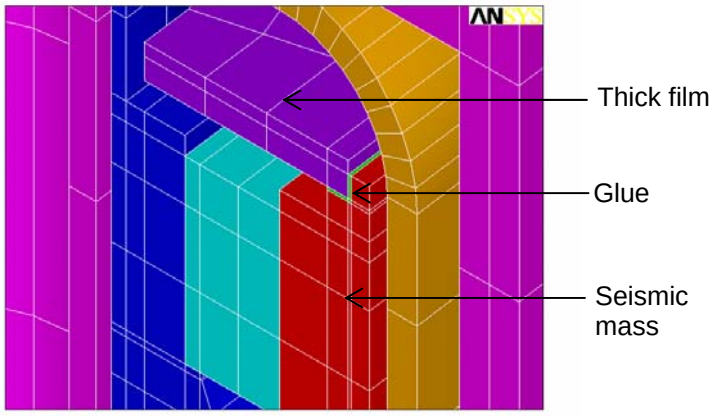

Fig. 6.7: The glue connecting the preamplifier and the seismic mass.

Table 6.5: The glue influence.

	Mounted resonance frequency	Transverse resonance frequency
No glue	47.6 kHz	25.2 kHz
With glue	43.4 kHz	25.2 kHz

Besides gluing the preamplifier and the seismic mass, the glue is used to glue the center post and the housing as well. Same conclusion can be made that the glue layer should be as thin as possible, as stiff as possible.

So far, it can be seen that a good agreement is achieved between the specifications of the physical and virtual prototypes. The whole design procedure and the detailed analysis improve our scientific understandings of Annular Shear design and the variants. We can say that a new Center-bolt Annular Shear design is finished successfully with the help of the virtual prototypes.

6.3 Improved OrthoShear® accelerometer

6.3.1 Requirement

In this section, the design of a new generation of OrthoShear® is described. It is called Improved OrthoShear®. Since there is no definite requirements for the design, the common requirements for piezoelectric accelerometer are taken.

(1) Small size and light weight.
(2) High resonance frequency (for normal application).
(3) Small base bending effect.

6.3.2 Design procedure

The final virtual prototype is as shown in Fig. 6.8. The red part is the seismic mass, the cyan part is the ceramic, the blue parts are the arms, the orange parts are the hinges, and the green part is the thick film (preamplifier). The material used for each component is shown in Table 6.6.

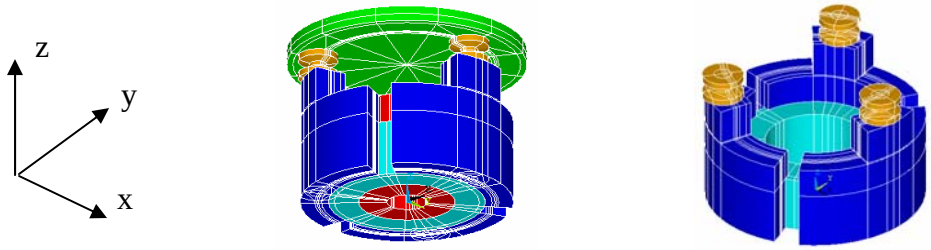

Figure 6.8: The Improved OrthoShear® design.

Table 6.6: The materials list.

Component	Material	
	OrthoShear®	Improved OrthoShear®
Ceramic	Pz23	Pz27
Seismic mass	Tungsten	Tungsten
Hinges	Brass	Berylco
Arms	Stainless steel	Tungsten
Insulating ring	Teflon	
Clamping ring	Inconel	
Nuts	Stainless steel	Stainless steel
Housing	Titanium	Titanium

In order to describe the design procedure easier, the boundary condition for each direction (3 directions totally) is shown in Fig. 6.9.

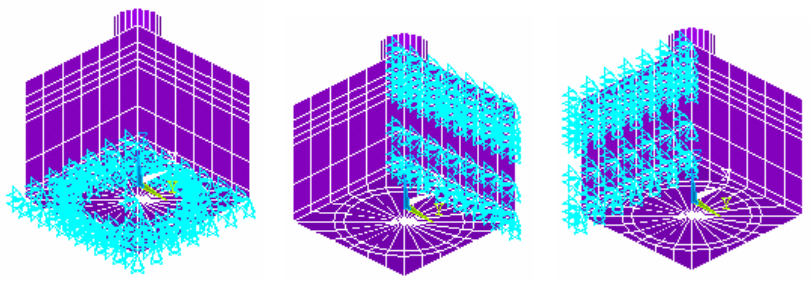

(a) z-axis (b) x-axis (c) y-axis

Figure 6.9: Boundary condition.

Size and weight

It can be seen from Table 6.6 that the Improved OrthoShear® design does not have Insulating ring and the Clamping ring because the components are soldered together instead of using mechanical preloading. It reduces the size and the weight.

Table 6.7: The weight and the size.

	OrthoShear®	Improved OrthoShear®
Size (H×W×L)	17 mm×17 mm×14.5 mm	10mm×10 mm×10 mm
Weight	15 gram	4.5 gram

Mounted resonance frequency

Based on the study described in Chapter 5, the material of the hinges is changed from brass to Berylco. The two materials properties are given in Table 6.8.

Table 6.8: The hinges' material properties.

	Brass	Berylco
Density (kg/m^3)	8600	8746
Young's Modulus (10^{10} N/m^2)	10.4	15
Poisson's ratio	0.37	0.30

It is clear that Berylco has bigger Young's Modulus than brass, which means that the Berylco hinges are stiffer than the brass ones. Therefore the resonance frequency should be increased.

Visualized resonant modes of the virtual prototype are shown in Fig. 6.10. It can be recognized from "TIME=" on the right side of each figure that the z-axis mounted resonance frequency is 24.7 kHz. The resonance frequency for x- and y-axis are 10 kHz and 10.2 kHz, respectively.

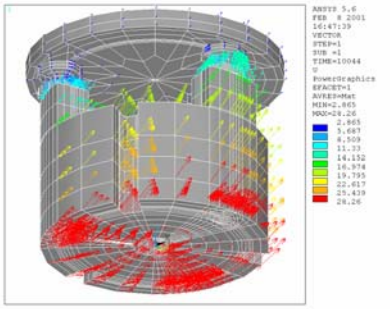

(a) The resonance mode of x-axis.

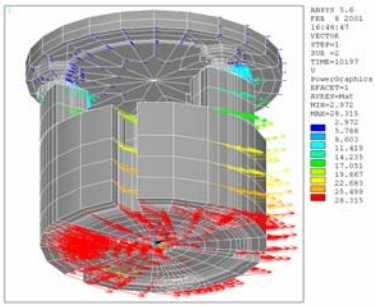

(b) The resonance mode of y-axis.

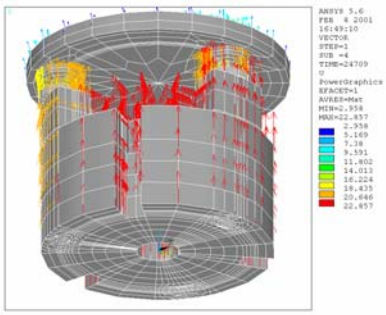

(c) The resonance mode of z-axis.

Fig. 6.10: The resonant modes of the virtual prototype.

The modal analysis results obtained by mounting the prototype on each of five mounting surfaces are given in Table 6.9. Fig. 6.11 illustrates the surface number. The bottom of the virtual prototype is Surface-5.

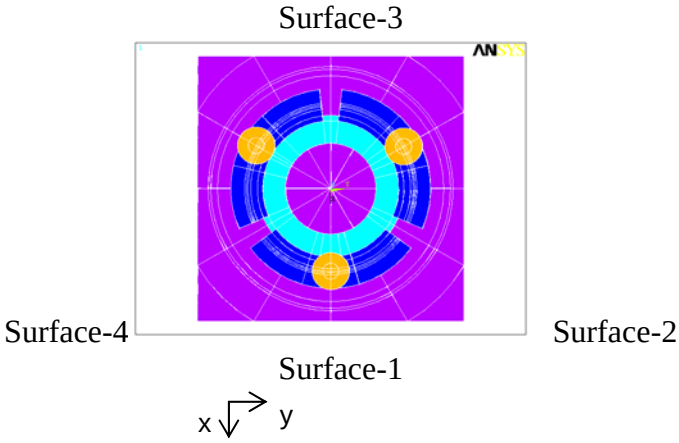

Fig. 6.11: Illustration of the face number.

Table 6.9: The resonance frequency of the virtual prototype.

Resonance frequency	Surface-1 mounted	Surface-2 mounted	Surface-3 mounted	Surface-4 mounted	Surface-5 mounted
X-axis	10.2 kHz	10.3 kHz	10.3 kHz	10.2 kHz	10.0 kHz
Y-axis	10.4 kHz	10.4 kHz	10.4 kHz	10.5 kHz	10.2 kHz
Z-axis	22.4 kHz	22.2 kHz	22.3 kHz	22.5 kHz	24.7 kHz

Table 6.9 shows that when the virtual prototype is mounted on Surface-1, -2, -3 and -4, the difference between the simulated results is not big. When the prototype is mounted on Surface-5, the results are different from those obtained when the prototype is mounted on the other faces. The explanation can be found from section 4.2.2.

The mounted resonance frequency comparison between the OrthoShear® and the Improved OrthoShear® designs is listed in Table 6.10. It shows that the mounted resonance frequency is improved.

Table 6.10: The mounted resonance frequency.

	OrthoShear®	Improved OrthoShear®
x-, y-axis	10.4 kHz	10 kHz
z-axis	21.7 kHz	24.7 kHz

Base bending effect

The number of hinges is reduced from 4 to 3 to lower the base bending effect. The reason is that it is much easier to get a balance surface with 3 hinges than with 4 hinges.

The base bending effect of the virtual prototype is 0.0022 $ms^{-2}/\mu\varepsilon$. It is only $\frac{1}{63}$ of the base bending effect of OrthoShear®, which is 0.14 $ms^{-2}/\mu\varepsilon$.

Sensitivity

Fig. 6.15 briefly presents the charge-collecting theory for Improved OrthoShear® design. The details can be found from [6-1, 2].

Since the preamplifier has not been made so far, we only have the output signal from the accelerometer mechanical unit. According to Fig. 6.15, the charge output for each axis can be expressed as following:

$$Q_Z = Q_A + Q_B + Q_C \tag{6.1}$$

$$Q_x = Q_A + Q_B - 2Q_C \tag{6.2}$$

$$Q_y = -Q_A + Q_B \tag{6.3}$$

where *A*, *B* and *C* denote the segments of the arm. The charge sensitivities are listed in Table 6.11.

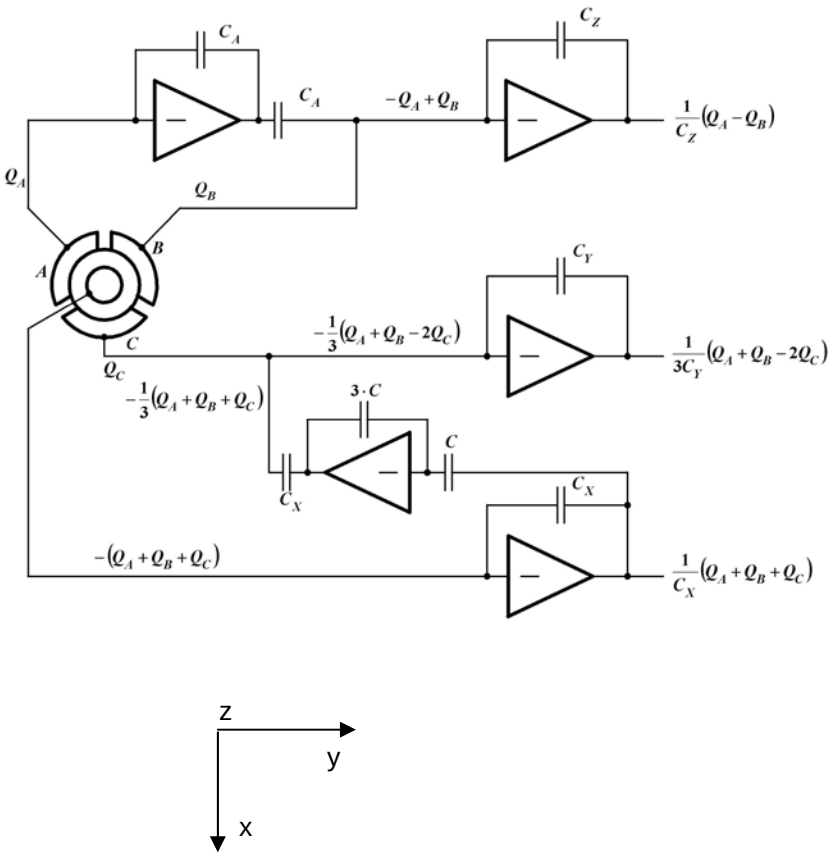

Fig. 6.15: The charge-collecting theory of the improved OrthoShear® design.

Table 6.11: Charge sensitivities.

	x-axis	y-axis	z-axis
	2.43 pC/ms^{-2}	**1.38** pC/ms^{-2}	**0.35** pC/ms^{-2}
A	0.41 pC/ms^{-2}	-0.69 pC/ms^{-2}	0.12 pC/ms^{-2}
B	0.41 pC/ms^{-2}	0.69 pC/ms^{-2}	0.11 pC/ms^{-2}
C	-0.81 pC/ms^{-2}	0.005 pC/ms^{-2}	0.12 pC/ms^{-2}

When the virtual prototype is mounted on the bottom, the transverse sensitivities are shown in Table 6.12, which can be considered as zero.

Table 6.12: The transverse sensitivities (pC/ms^{-2}).

	x-axis excitation	y-axis excitation
	0.0015 pC/ms^{-2}	**0.0007** pC/ms^{-2}
A	0.41 pC/ms^{-2}	-0.69 pC/ms^{-2}
B	0.4 pC/ms^{-2}	0.69 pC/ms^{-2}
C	-0.81 pC/ms^{-2}	0.005 pC/ms^{-2}

Figure 6.16 shows the frequency response of the virtual prototype with z-, x- and y-axis excitation within the full frequency range, respectively.

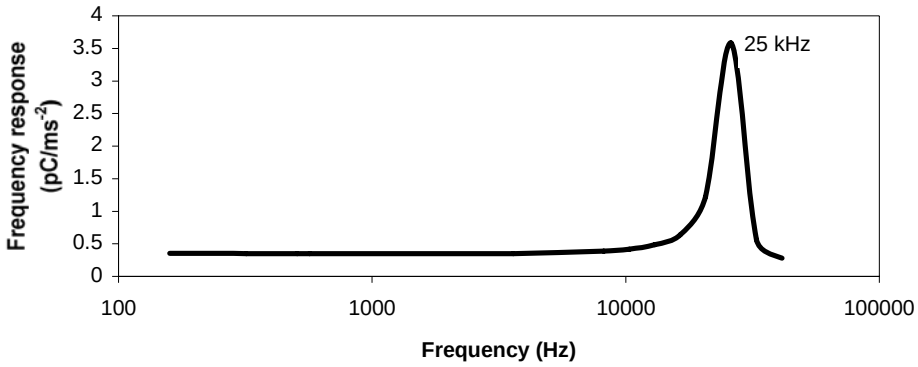

(a) Frequency response with z-axis excitation.

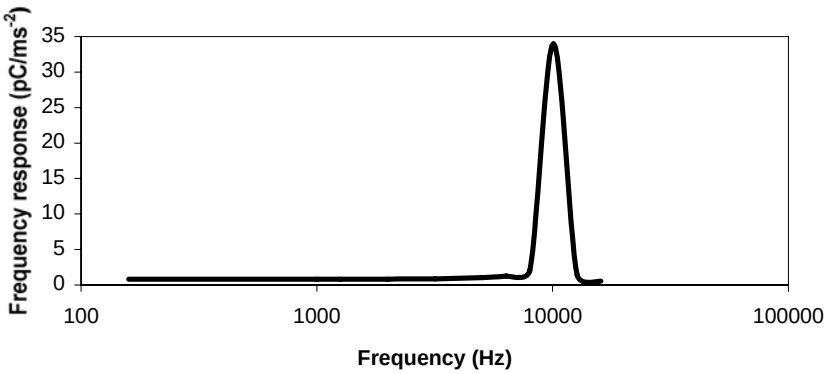

(b) Frequency response with x-axis excitation.

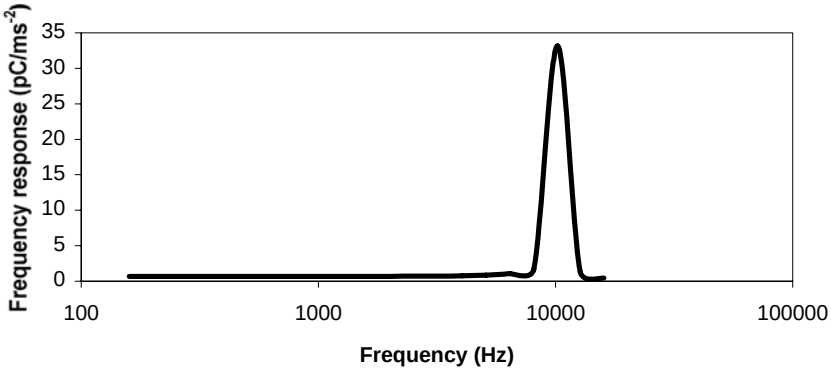

(c) Frequency response with y-axis excitation.

Fig. 6.16: The frequency response of the virtual prototype.

The shear stress induces the charge on the surface of the ceramic. The XZ shear stress distribution in the ceramic ring with z-axis excitation is shown in Fig. 6.18. It can be seen that with z-axis excitation, the stress distribution is partly symmetric according to the hinges' position. The areas subjecting the largest stress are the ones where the hinges sit as shown in Fig. 6.17.

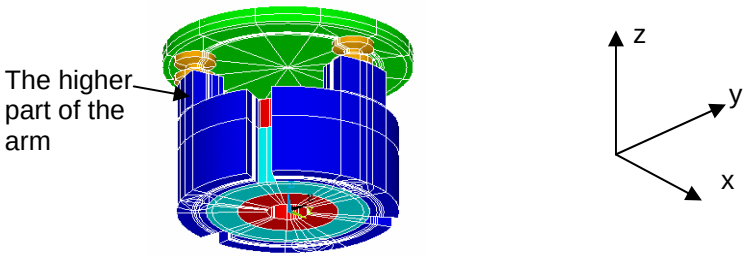

Fig. 6.17: The configuration of the structure.

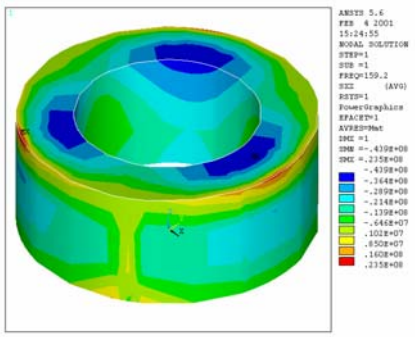

Fig. 6.18: The XZ shear stress distribution in the ceramic.

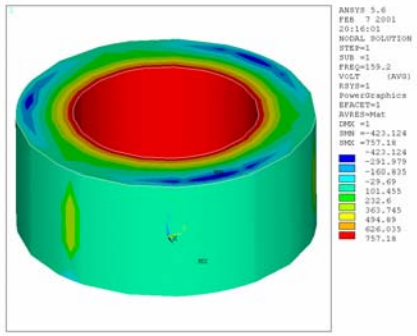

Fig. 6.19: The voltage distribution in the ceramic.

Fig. 6.19 shows the voltage distribution within the ceramic ring with z-axis excitation. The voltage sensitivity is 0.757 mV/ms^{-2}. It can be seen that the voltage distribution is radially even except the hinge areas and the arm gap areas. This is due to the fact that the external surface of the ceramic is grounded except the arm gap areas.

Based on $C = Q/V$, the capacitance can be estimated, which is 466 pF.

6.3.3 Experimental verification

Table 6.13: The mounted resonance frequency.

	Physical prototype	Virtual prototype	Traditionally Calculated
x-axis	9.65 kHz	10. kHz	Not available
y-axis	9.65 kHz	10.2 kHz	Not available
z-axis	22.15 kHz	24.7 kHz	Not available

Table 6.14: The charge sensitivity.

	Physical prototype	Virtual prototype	Calculated
x-axis	2.38 pC/ms^{-2}	2.43 pC/ms^{-2}	2.41 pC/ms^{-2}
y-axis	1.38 pC/ms^{-2}	1.38 pC/ms^{-2}	1.39 pC/ms^{-2}
z-axis	0.328 pC/ms^{-2}	0.353 pC/ms^{-2}	0.327 pC/ms^{-2}

6.3.4 Detailed analysis

Thickness of the thick film (preamplifier)

As shown in Fig. 6.5, the thick film is glued to the housing. In this part, we consider the influence of the thickness of the thick film on the specifications.

As what had studied in Chapter 5, the thickness of the thick film does not influence the charge sensitivity, but it influences the mounted resonance frequency. Table 6.15 shows the results.

Table 6.15: The influence of the thickness of the thick film.

Thickness (mm)	z-axis charge sensitivity (pC/ms^{-2})	Mounted resonance frequency (kHz)		
		x-axis	y-axis	z-axis
1.0	0.357	10.1	10.2	26.1
0.63	0.353	10.	10.2	24.7
0.5	0.35	9.9	10.1	23.5

It can be seen that the thicker the thick film, the higher the z-axis mounted resonance frequency. But as described in Chapter 5, there is a problem with drilling holes through a thick film if its thickness is beyond a certain limitation, therefore the solution should be selecting the thickest thick film as long as the drilling problem does not come up.

Soldering influence

When the hinges are soldered to the arms, it is not easy to control where the tin will stay between the hinges and the arm. Fig. 6.20 illustrates two situations. The left one describes the situation without considering the tin effect, in other words, it is a perfect soldering. The right one describes that the magenta tin fills all available space. The influenced resonance frequencies are shown in Table 6.16. It can be seen that the soldering decreases the resonance frequencies. This is due to the fact that the material used for soldering is softer than Berylco and Tungsten used for the hinges and the arms, respectively. Therefore the stiffness of the whole structure is decreased.

Table 6.16: The tin influence on the resonance frequency.

	Perfect contact	Filled with tin
x-axis	10.7 kHz	10. kHz
y-axis	10.9 kHz	10.2 kHz
z-axis	26.3 kHz	24.7 kHz

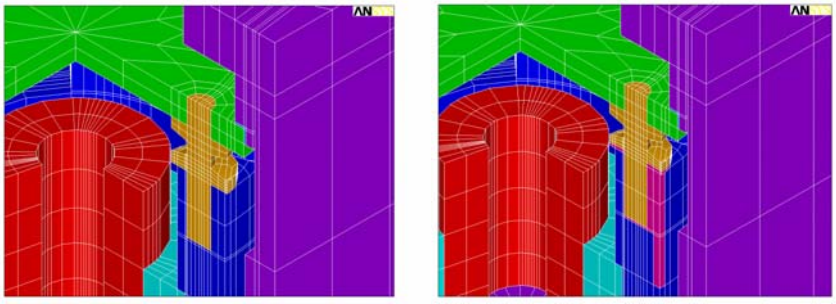

Fig. 6.20: The tin influence.

During designing, there are three prototype versions. The one described above is Version 3. The difference between Version 1 and 2 is the arms' shape. The difference between the Version 1 and 3 is the hinges' shape.

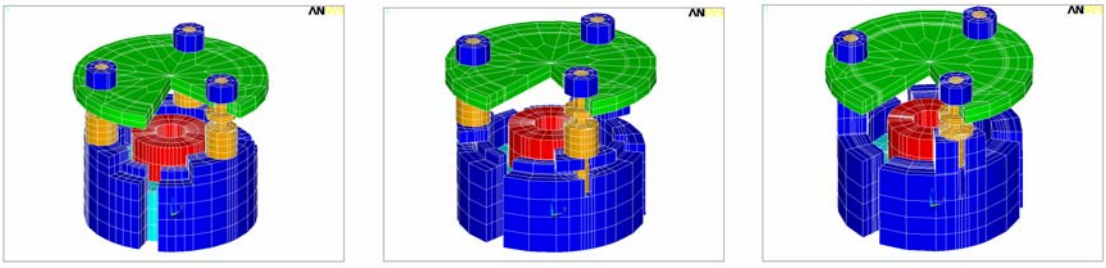

(a) Version 1. (b) Version 2. (c) Version 3.

Fig. 6.21: Virtual prototypes.

Sensitivity limitation

The seismic mass of the virtual prototypes is a cylinder with a center hole. The hole is used to adjust the sensitivity. We can fill the hole to obtain the highest sensitivity. But at the same time the mounted resonance frequency will be reduced. According to eqn. (2.28), the change of the charge sensitivity can be estimated easily. But it is difficult to estimate how big the influence on the mounted resonance frequency is by using any analytical model.

By using the virtual prototype, the influence on both the sensitivity and the mounted resonance frequency can be obtained. The results shown in Table 6.17 are based on the virtual prototype Version 1. It can be seen that the x-, y- and z-axis sensitivities are increased 5%, 5% and 17%, respectively. The x-, y- and z-axis mounted resonance frequencies are decreased 1.9%, 1.9% and 3.8%, respectively. The weight is 0.43 gram heavier.

Table 6.17: The specifications with different seismic mass inner radius.

Inner radius of the seismic mass (mm)	Charge sensitivity (pC/ms^{-2})			Mounted resonance frequency (kHz)		
	x-axis	y-axis	z-axis	x-axis	y-axis	z-axis
1.4 (actual)	2.38	1.38	0.349	10.4	10.4	26.2
0	2.51	1.45	0.409	10.2	10.2	25.2

Arm shape

Version 1 and 2 are analyzed to estimate the influence of the arm shape on specificationsIt has to be stated that the glue influence described earlier is not considered.

Table 6.18: The arm shape influence on the specifications.

	Charge sensitivity (pC/ms^{-2})			Mounted resonance frequency (kHz)		
	x-axis	y-axis	z-axis	x-axis	y-axis	z-axis
Version 1	2.38	1.38	0.349	10.4	10.4	26.2
Version 2	2.19	1.33	0.345	10.	10.2	26.2

It can be seen that the arm shape does not influence the specifications very much. The reason why the arm shape shown in Fig. 6.20 (b) had been used is that we had thought to use a clip to fix the lower handle of the hinges. Afterwards we decided to solder the hinges and the arm, therefore the clip idea is given up.

Arm gap

Fig. 6.22 illustrates the definition of the arm gap. Table 6.19 shows the specifications of the virtual prototype Version 1 with different arm gaps. It has to be stated that the glue influence described earlier is not considered.

It can be seen that as the arm gap angle increases the y-axis sensitivity is decreased while the z-axis sensitivity stays the same. The reason is that the arms act as part of the active seismic mass for x-, y-axis measurements, but not for z-axis measurement.

Table 6.19: The arm gap influence on the specifications.

Arm gap angle	Charge sensitivity (pC/ms^{-2})		Mounted resonance frequency (kHz)		
	y-axis	z-axis	x-axis	y-axis	z-axis
6°	1.4	0.348	10.3	10.3	25.8
13° (actual)	1.38	0.349	10.4	10.4	26.2
26°	1.29	0.35	10.6	10.6	27.0

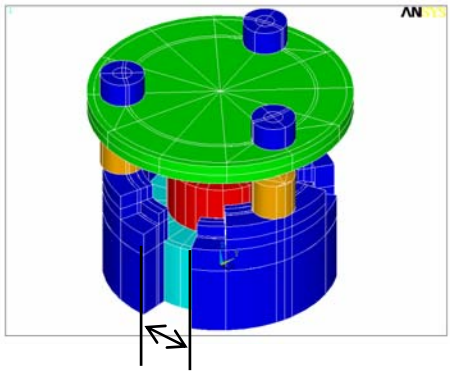

Fig. 6.22: Illustration of the arm gap.

The increase of the resonance frequency is due to the fact that the structure becomes stiffer because of the reduced arm.

Hinge shape

The hinges are the key points of the design. On one hand, the hinges should be as flexible as possible; on the other hand, the hinges should subject as less influence from the base as possible to reduce the base bending effect.

Version 1 has special hinges whose lower handle is two times thicker than the upper one. The reason to do so is that we want to keep the hinges away from the base as far as possible. Version 3 has normal hinges. The specifications with two different hinges are given in Table 6.20. It has to be stated that the glue influence described earlier is not considered.

Table 6.20: The hinge shape influence on the specifications.

Hinge shape	Charge sensitivity (pC/ms^{-2})			Mounted resonance frequency (kHz)		
	x-axis	y-axis	z-axis	x-axis	y-axis	z-axis
Special	2.38	1.38	0.349	10.4	10.4	26.2
Normal (actual)	2.49	1.4	0.353	10.7	10.9	26.3

It can be seen that the hinges' shape does not change the specifications much. It is because that when the special arms are used, the hinges are normal, when normal arms are used, the hinges are special. The effect caused by the special hinge shape is always cancelled by the effect caused by the normal arm shape.

In short, the Improved OrthoShear® has improved performances compared with OrthoShear®. The size is reduced from 17mm×17mm×10mm down to 10mm×10mm×10mm. The weight is reduced from 15 gram down to 4.5 gram. The z-axis mounted resonance frequency is increased from 21.7 kHz up to 24.7 kHz. The base bending effect is reduced down to 1/63 times that of the OrthoShear®.

6.4 Conclusion

The designs of two new piezoelectric accelerometers are described in this chapter.

The first one is a new Center-bolt Annular Shear design, which is based on normal Annular Shear design. The difference is that the new design has a center hole for mounting and uses soldering instead of clamping ring to form the ceramic and the mass in position. Detailed analysis shows that the accelerometer has a good tolerance with the center bolt used. In order to isolate the high and low frequency interference, a brass-made inner shield is used as shown in Fig. 6.2 and 6.3.

The second one is Improved OrthoShear® design, which is the new generation of OrthoShear® design. The main new properties of the new generation design are: (1) the three hinges are used instead of four hinges, (2) the clamping ring & insulating ring are absent to reduce the weight and size. Assigned improvements had been achieved, which are smaller size and lighter weight, higher resonance frequency, smaller base bending effect.

Physical prototypes were made for both designs. Comparisons between the virtual and physical prototypes present good agreements.

So far we can make such a conclusion for the accelerometer work that the virtual prototype and the detailed analysis presented in Chapter 5 have been experimentally verified to be able to make better and faster designs.

References

6-1 Hansen, Knud Styhr, “A New Design Principle for Triaxial Piezoelectric Accelerometers”, Technical Review, Bruel & Kjaer, No. 1, 2000

6-2 Hansen, Knud Styhr, “A New Design Principle for Triaxial Piezoelectric Accelerometers”, ICSV, 2001

7
Transducers for Sound

7.1 Introduction

A microphone can be considered as a transducer that converts an acoustic sound signal into an electrical signal. To meet the needs of a specific microphone application, the designer can choose between a number of different acoustic operation and transduction principles. Therefore there are many different types of microphones, such as the electromagnetic, the electrodynamic, the piezoelectric, the piezoresistive, the electrostatic or condenser microphone, the contact microphone and the optical microphone. A very good brief introduction of these microphones is given by [7-1].

Practically all precision measurement microphones are condenser microphones that use a constant electrical charge for conversion of the diaphragm displacement into an electrical signal. These microphones can be realized with the high quality and the predictable performance that is necessary for any type of measurement device [7-2].

In this chapter, the construction of condenser microphones including traditional and silicon ones is introduced first. Afterwards, the operation principle and specifications of condenser microphones are presented. Following the design trade-off, the design methods for condenser microphones are described. In short the goal of this chapter is to give a technical overview of condenser microphones.

7.2 Construction of condenser microphones

7.2.1 Traditional condenser microphone

A traditional measurement condenser microphone consists of a metal housing, a circular backplate, a circular diaphragm and an electrical insulator as shown in Fig. 7.1. The electrical insulator and the backplate are mounted inside the housing behind the diaphragm. The holes of the backplate act as a damping provider allowing the flow of air to or from the air gap.

Since the microphone is to be used for measurement, it must be stable over time and its properties should preferably not vary with variations in ambient temperature, pressure and humidity. The key parts are the diaphragm and the backplate that have to be clean, flat and parallel to each other.

The material selection and the manufacturing procedure are not going to be included in this thesis.

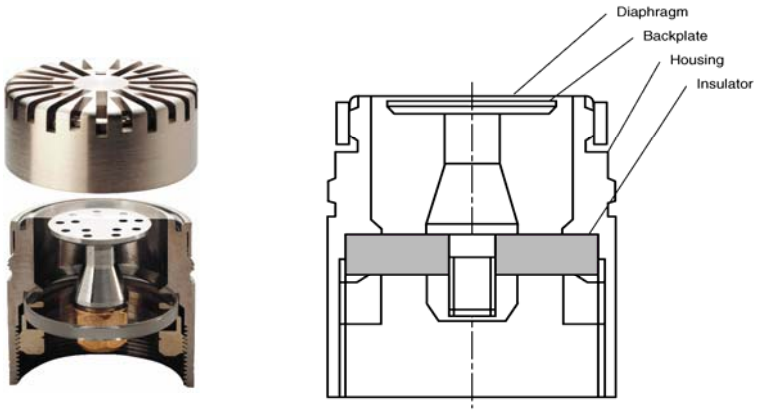

Fig. 7.1: A traditional condenser microphone.

7.2.2 Silicon condenser microphone

A silicon condenser microphone has similar mechanical structure as a traditional one. As shown in Fig. 7.1 and 7.2, they both consist of the diaphragm, backplate, housing and insulator. But they do have some fundamental differences. Table 7.1 lists the differences related with the work done in this thesis.

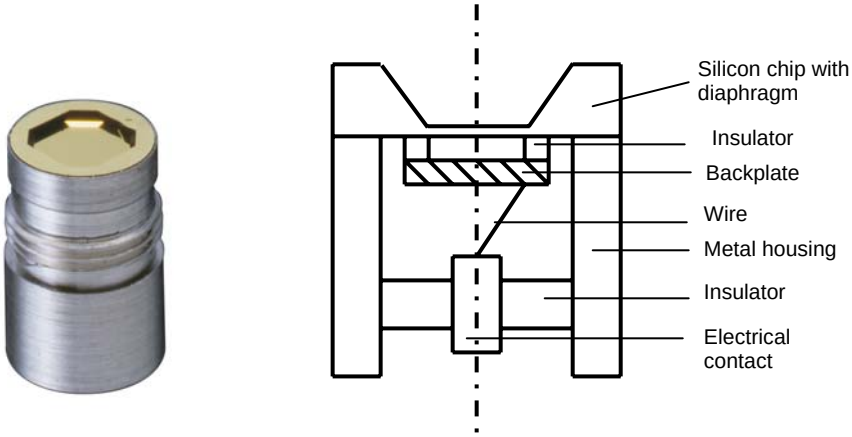

Fig. 7.2: A silicon condenser microphone.

Table 7.1: The main differences between a silicon and traditional condenser microphone related with this thesis.

	Silicon condenser microphone	Traditional condenser microphone
Diaphragm shape	Octagonal	Circular
Backplate shape	Square	Circular

7.3 Operation principle

A condenser microphone converts sound pressure into capacitance variations. The variations in capacitance then are converted into an electrical voltage. Usually we take advantage of a constant electrical charge to make the conversion. This charge can be obtained by two methods. One is to bias the diaphragm and the backplate with an external voltage source. The other one is to generate an electrical field with a charged dielectric layer on top of the backplate. In this thesis, only the condenser microphone with an external voltage source is considered. Its transduction principle is illustrated in Fig. 7.3.

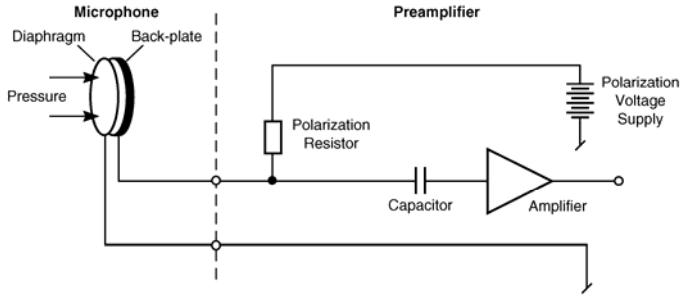

Fig. 7.3: Capacitance transduction principle.

The capacitor contributing the capacitance variations is formed by two plates, which are the diaphragm as a movable plate and the backplate as a stationary plate. The two plates are polarized by an external voltage source that supplies a charge via a bias resistor as shown in Fig. 7.3. The resistance of the resistor must be so high that it ensures a constant charge on the microphone when the microphone capacitance changes because of the sound pressure acting on the diaphragm.

Based on the constant charge assumption, when a sound pressure acts on the diaphragm, the diaphragm deflects. Therefore the distance between the diaphragm and the backplate changes. Consequently the capacitance between the two plates varies. The capacitance variation results in a corresponding AC voltage across the plates. Assuming that the diaphragm works as a piston and the input capacitance is negligible the output voltage *v* can be expressed as:

$$\left(V_0 + v\right)\cdot\frac{\varepsilon_0 \cdot A}{d_0 + d(0)} = Q_0 = V_0 \cdot \frac{\varepsilon \cdot A}{d_0} \tag{7.1}$$

$$v = V_0 \cdot \frac{d(0)}{d_0}$$

where V_0 is the voltage across the capacitance with diaphragm at rest position, v is a small change of the voltage across the capacitance, ε_0 is the permitivity, A is the acting area, d_0 is the air gap distance at rest, $d(0)$ is the center deflection, Q_0 is the constant charge stored on the plate capacitor.

It can be seen that the output voltage is proportional to the displacement of the diaphragm, which is proportional to the sound pressure.

7.4 Specifications

In this section, the specifications of condenser microphones are going to be described including the sensitivity, the fundamental resonance frequency and the collapse voltage followed by the design trade-off.

Since the derivation of the mathematics solution is beyond the project, in the following sections, some omissions are made.

Fig. 7.4 illustrates the definition of the symbols, which are to be used in this section and the next chapter.

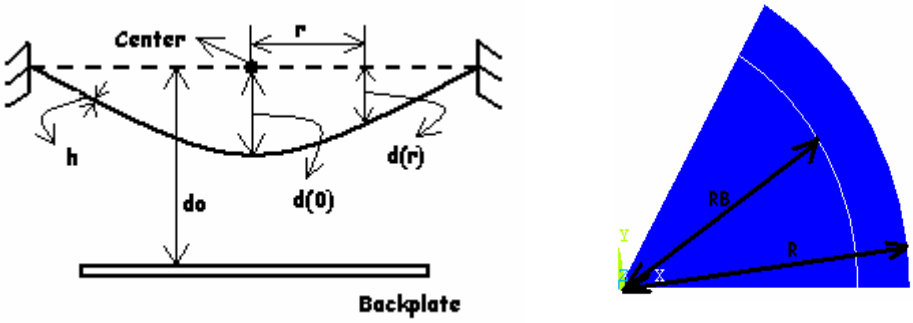

Fig. 7.4: The symbols' definition.

Center: the center of the diaphragm
r: the distance to the diaphragm center
h: the thickness of the diaphragm
d_0: the air gap distance at rest
d(0): the center deflection of the diaphragm
d(r): the deflection of the diaphragm
R_B: the radius of the backplate
R: the radius of the diaphragm

7.4.1 Sensitivity

Depending on the type of sound field where a microphone is used, there are three types of sensitivities for the same microphone, which are free-field sensitivity, diffuse-field sensitivity and pressure-field sensitivity [7-2]. A free-field means that the sound waves in the field can propagate freely. A diffuse-field means that the sound waves in the field can arrive simultaneously from all directions with equal probability and level. A pressure-field means that the sound pressure in the field has the same magnitude and phase at any position.

This project only studies the *open-circuit pressure-field sensitivity*, valid with an idealized preamplifier which does not load the microphone [7-1, 2, 3].

For a condenser microphone, the transduction from input sound pressure to output electrical signal usually is done in four steps [7-3]. First, the sound pressure mechanically deflects the diaphragm. Second, because of the constant charge across the diaphragm and the backplate, the voltage change arises between the capacitor plates. Third, the electrical signal is attenuated by the parasitic capacitance and by the input capacitance of the amplifier. Finally, the signal is amplified according to the impedance conversion. As we want the open-circuit sensitivity, only the first two steps and the attenuation done by the parasitic capacitance are considered.

In the first step, we have the mechanical sensitivity defined as [7-1, 3]

$$S_m = \frac{d}{dP}[d(0)] \tag{7.2}$$

where *dP* is a small change of the pressure acting on the diaphragm, *d[d(0)]* is the resulting small change of the diaphragm center deflection.

For a circular diaphragm modeled as a piston with a large initial tension *T*, the expression of the mechanical sensitivity is presented by Sessler [7-4] as

$$S_m = -\frac{A}{8\pi T} \tag{7.3}$$

The negative sign is due to the fact that the change in distance between the two plates is negative for a positive pressure.

Inserting $A = \pi R^2$ and $T = \sigma h$, where σ is the diaphragm tensile stress, into eqn. (7.3), we have

$$S_m = -\frac{R^2}{8\sigma h} \tag{7.4}$$

In the second step, we have the electrical sensitivity defined as [7-1, 3, 4]

$$S_e = \frac{dV}{d[d(0)]} \tag{7.5}$$

where *d[d(0)]* is a small change of the distance between the diaphragm and the backplate, *dV* is the resulting change of the voltage across the two plates.

For a condenser microphone with external voltage source V_0, eqn. (7.5) can be expressed as:

$$S_e = \frac{V_0}{d_0} \tag{7.6}$$

Combining the mechanical and electrical sensitivities, we can get the open-circuit sensitivity. It is defined as:

$$S_o = \frac{dV}{dP} = \frac{d[d(0)]}{dP} \cdot \frac{dV}{d[d(0)]} = S_m \cdot S_e = -\frac{R^2}{8\sigma h} \cdot \frac{V_0}{d_0} \tag{7.7}$$

It should be stated that eqn. (7.7) is obtained by using a piston model for the diaphragm. When the diaphragm deflection is modeled as a parabolic one the open-circuit sensitivity expression is still the same.

It can be seen that the sensitivity is determined by a mechanical and an electrical part that are assumed to be independent. The electrostatic forces are assumed not to influence the sensitivity of the diaphragm. The coupling effect is assumed to be negligible.

Eqn. (7.7) shows that

(1) the bigger the diaphragm radius, the higher the sensitivity
(2) the less stiffer the diaphragm, the higher the sensitivity
(3) the smaller the distance between the diaphragm and the backplate, the higher the sensitivity.

Eqn. (7.7) also shows that the open-circuit microphone output signal is proportional to the electrical field strength in the air gap. Therefore, increasing the bias voltage V_0 in the case of a condenser microphone results in an increased microphone output signal.

7.4.2 Resonance frequency

The motion of a rotational symmetric membrane without external forces can be described by the following differential equation [7-5]:

$$\sigma\left(\frac{\partial^2 \eta}{\partial r^2} + \frac{1}{r}\frac{\partial \eta}{\partial r}\right) = \chi \frac{\partial^2 \eta}{\partial t^2} \tag{7.8}$$

or

$$\frac{\partial^2 \eta}{\partial r^2} + \frac{1}{r}\frac{\partial \eta}{\partial r} + (k')^2 \eta = 0 \tag{7.9}$$

where σ is the tensile force of the membrane per unit length, η is the membrane deflection, r is the distance from the membrane center, χ is the mass per unit area, $(k')^2 = \omega^2 \frac{\rho}{\sigma}$ where ρ is the diaphragm density.

[7-5] derived the solution to the above equations. The fundamental resonance frequency of the membrane is expressed as:

$$f_1 = 0.383 \frac{1}{R}\sqrt{\frac{\sigma}{\rho}} \tag{7.10}$$

7.4.3 Collapse voltage

We know that an increased bias voltage can increase the sensitivity as shown in eqn. (7.7). But the bias voltage cannot be increased unlimitedly because the electrical field caused by the bias voltage results in an electrostatic force, which depends on the distance between the diaphragm and the backplate. The force causes the diaphragm to deflect towards the backplate.

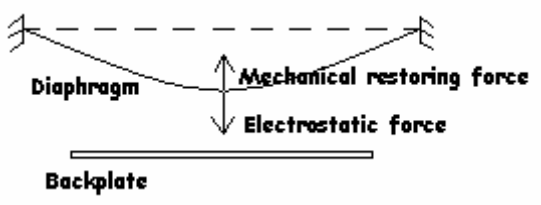

Fig. 7.5: The forces acting on the diaphragm.

If the microphone is stable and at rest (no sound pressure), the mechanical restoring force, due to the tension in the diaphragm, balances the electrostatic force. Fig. 7.5 describes the relationship between the forces. But if the bias voltage is too high, the deflection of the diaphragm will continue to increase until physical contact is made with the diaphragm and the backplate. For a given diaphragm, the minimum voltage where this collapse occurs is the *collapse voltage*.

So far, we can see that the higher the bias voltage, the higher the sensitivity, at the same time, the closer the microphone comes to instability. Practically in order to keep the microphone stable the bias voltage used usually is lower than 80% of the collapse voltage. Therefore it is very important for designers to know the collapse voltage to optimize the microphone sensitivity.

For a circular symmetric thin stretched diaphragm, the deflection of each point of the diaphragm is given by [7-6] as

$$\frac{T}{r}\frac{d}{dr}\left(r\frac{d}{dr}d(r)\right) = -F_{el} \tag{7.11}$$

where T is the tensile stress, r is the distance from the diaphragm center, $d(r)$ is the deflection, F_{el} is the electrostatic force per unit area.

In our case the thickness of the diaphragm is much smaller than its radius. Eqn. (7.11) can be used to describe the position of the diaphragm, which is determined by the electrostatic force.

Since when the diaphragm deflects it does not move like a rigid piston, which means the distance between the diaphragm and the backplate is a function of the radial distance to center, the electrostatic force per unit area whose radial distance to center is r is used as [7-7]:

$$F_{el} = \frac{1}{2}\varepsilon_0 \left[\frac{V}{d_0 - d(r)} \right]^2 \tag{7.12}$$

After introduction of the generalized quantities

$$\eta = d(r)/d_0 \tag{7.13}$$

$$\zeta = r/R \tag{7.14}$$

$$\lambda = \frac{\varepsilon_0 R^2 V^2}{2 d_0^3 T} \tag{7.15}$$

eqn. (7.11) can be rewritten as

$$\frac{1}{\zeta}\frac{d}{d\zeta}\left(\zeta \frac{d\eta}{d\zeta}\right) + \frac{\lambda}{(1-\eta)^2} = 0 \tag{7.16}$$

The differential equation assumes that the effects of the fringing of the electrical fields in the openings of the diaphragm acting as the stationary electrode is negligible. These fringing effects are usually very small because of the close spacing between the diaphragm and the backplate about 20 μm compared to the backplate radius about 1.95 *mm* to 4.6 *mm* for 1/4" and ½" microphones.

In order to get the maximum bias voltage we have to determine that for which value of λ eqn. (7.16) becomes unstable. For a circular diaphragm with high tensile stress that has a same size circular backplate, Warren presented λ =0.789 [7-7].

According to λ =0.789, the collapse voltage can be described as:

$$V_c = \sqrt{\frac{0.789 \cdot 2 \cdot \sigma \cdot h \cdot d_0^3}{R^2 \cdot \varepsilon_0}} \tag{7.17}$$

7.4.4 Design trade-off

Rewriting eqns. (7.7) and (7.10) gives,

$$S_o = -\frac{R^2}{8\sigma h} \cdot \frac{V}{d_0} \tag{7.18}$$

$$f_{res} = \frac{0.383}{R}\sqrt{\frac{\sigma}{\rho}} \tag{7.19}$$

Eqns. (7.17), (7.18) and (7.19) show that

$$
\begin{aligned}
V_c &\propto \sigma^{1/2} \cdot h^{1/2} \cdot d_0^{3/2} \cdot R^{-1} \\
S_0 &\propto \sigma^{-1} \cdot h^{-1} \cdot d_0^{-1} \cdot R^2 \cdot V \\
f_{res} &\propto \sigma^{1/2} \cdot R^{-1} \cdot \rho^{-1/2}
\end{aligned}
\tag{7.20}
$$

According to eqn. (7.20), the design trade-offs are:

(1) Increasing the tensile stress of the diaphragm not only increases the resonance frequency, but also decreases the sensitivity.
(2) Increasing the diaphragm radius not only increases the sensitivity, but also decreases the resonance frequency.

It has be noted that there are other important specifications for condenser microphones, for example noise [7-1, 8, 9], but the project is not going to be concerned with them.

7.5 Design methods

A condenser microphone can be modeled by the Equivalent Electrical Circuit shown in Fig. 7.6. The components of the equivalent electrical circuit represent stiffness, masses and damping of the electro-mechanical system. The components are explained with Table 7.2. The more detailed explanation is beyond the thesis.

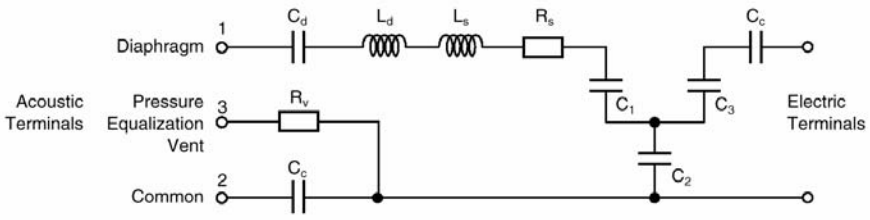

Fig. 7.6: The Equivalent Electrical Circuit of a condenser microphone.

Table 7.2: The explanation of the components in Fig. 7.6.

Symbol	Model Element
C_d	Diaphragm Compliance
L_d	Diaphragm Mass
L_s	Acoustic Mass of slit behind diaphragm
R_s	Acoustic Resistance of slit behind diaphragm
C_c	Acoustic Compliance of internal cavity
R_v	Acoustic Resistance of pressure equalization vent
C_1	Acoustic Coupling Compliance
C_2	Coupling Compliance / Capacitance
C_3	Electrical Coupling Capacitance
C_e	Electrical Capacitance (when diaphragm is blocked)

The lumped parameter modeling can determine the sensitivity, the frequency response including the magnitude and the phase, the complex acoustic diaphragm impedance, the electrical impedance and the inherent electrical noise of the microphone.

But the Equivalent Electrical Circuit also has limitations. Firstly, analytical expressions for the characteristic parameters are available only for simple mechanical and acoustic structures. Secondly, the one-dimentional displacement condition assumes a flat diaphragm, which is an important approximation when evaluating the sensitivity and the electrostatic forces. Finally, non-linear effects are neglected. Because of the limitations, the Equivalent Electrical Circuit can only calculate the average diaphragm deflection. Furthermore, it cannot calculate the collapse voltage.

For a condenser microphone design, the trade-off between the sensitivity and the resonance frequency has already been known for more than 40 years. Unfortunately it cannot be achieved by using the Equivalent Electrical Circuit effectively. Therefore, we have to face such a fact that on one hand, in order to get the best design we want to go to the limits of what is physically possible; on the other hand, the existing design methods cannot do so efficiently. This means that a new design method is needed. Conforming to the general tendency in industry, it should be the numerical simulation method.

Besides solving the problem the numerical design method can also make the trial-and-error process faster, reducing the time-to-market [7-10] for condenser microphones.

Since we have already achieved a considerable success in accelerometer design by using the FEM, the FEM is supposed to be to a new design method for condenser microphones. But it has to be stated that the work described in this thesis is not aiming to calculate all the microphone's specifications, since we for example cannot do calculations on the microphone's acoustic behavior. The main purpose is to calculate the open-circuit sensitivity and the diaphragm collapse voltage.

As presented in section 7.4.1, traditional analytical models assume the coupling effect negligible by using the independent mechanical and electrical part. But the FEM takes a true electromechanical system model. For example, with a FE model the electrostatic forces obtained based on the diaphragm mechanical movement change the diaphragm movement conversely. This cannot be simulated by using any traditional analytical model. Therefore from this point of view, we expect that the FEM could produce more accurate results than the traditional analytical methods.

7.6 Conclusion

In this chapter, an introduction of condenser microphones was given including the construction, operation principle, specifications and design methods.

The trade-off between the sensitivity and the resonance frequency has been known for more than 40 years for the condenser microphone design. Unfortunately this trade-off cannot be achieved effectively by using the traditional design methods. Therefore a numerical design method is put forward to solve the problem in order to get the better and faster design.

The following chapters are going to show how the FEM, one of the numerical methods, is applied to condenser microphones and what can be achieved.

Chapter 8 is going to present the FEM application to circular condenser microphones including the verification of results with well documented B & K microphones.

Chapter 9 is going to present the FEM application to silicon condenser microphones including the verification of results with experimental measurements.

References

7-1 A.G.H. van der Donk, "A silicon condenser microphone: modeling and electronic circuitry", University of Twente, 1992, Ph.D. thesis

7-2 Brüel & Kjær Sound & Vibration A/S, "Microphone Handbook", July 1996

7-3 Patrick Scheeper, "ASilicon Condenser Microphone: Materials and Technology", University of Twente, 1993, Ph.D. thesis

7-4 G.M. Sessler, "Topics in applied physics", Vol. 33, Electrets, 4th edn. Springer-Verlag, Berlin, 1980

7-5 Fritz Ingerslev and Knud Rasmussen, "Noter til forelaesninger i elektroakustik: Svingende membraner", 1965, in Danish

7-6 K. Teer, "On the Optimum Configuration for a condenser microphone", ACUSTICA, Vol.15 (1965), p.256-263

7-7 J.E. Warren and A.M. Brzezinski, "Capacitance-Microphone Static Membrane Deflections", J. Acoust. Soc. Am., Vol. 52, No. 3, 1972, p.711-719

7-8 R.R. Spencer et al., "A Theoretical Study of Transducer Noise in Piezoresistive and Capacitive silicon Pressure Sensors", IEEE Trans. Elec. Devices, Vol. 35, No. 8, August 1988, p.1289-1298

7-9 P.R. Barabash and R.S.C. Cobbold, "Basic Limitations of Isfet and Silicon Pressure Transducers: Noise Theory, Models and Device Scaling", Sensors and Actuators, 4(1983), p.427-438

7-10 V. Cutanda, "Business report – Technology management and technology creation in Brüel & Kjær in connection with the industrial Ph.D. project Numerical Transducer Modeling", 2001

8
FEM Applied to Circular Condenser Microphone

8.1 Introduction

The main objective of the modeling work for microphones is to explore the possibilities of new and better design methods, particular for traditional measurement condenser microphone and the micro-machined silicon condenser microphone. As demonstrated, the FEM is used to carry out the work.

The first model described here is based on the traditional circular geometry. The advantage of this approach is that the FE model can be compared with existing analytical models, and that experimental verification of simulated results can be done with well-documented B & K microphones.

In this chapter, the modeling of a circular condenser microphone is described first including a static study of a circular diaphragm, a study of the diaphragm with a same size backplate and the diaphragm with a smaller backplate. A comparison between the simulated and measured results of two B & K Type 4190 ½" microphones is shown. In the last part of this chapter the backplate dimension is optimized generally.

8.2 Modeling of a circular condenser microphone

In this analysis several simplifying assumptions have been made. First, it has been assumed that the diaphragm is under isotropic tension, which remains constant as the diaphragm moves. Because the range of the diaphragm dynamic deflections is relatively small (1 to 20 μm), the assumption is valid [8-1].

Second, it has been assumed that the bending rigidity of the diaphragm is insignificant compared to the tensile restoring force. For the diaphragm using very fine-grained nickel foil or special stainless steel alloy as studied in this project, this assumption is correct [8-1].

Third, it has been assumed that the damping can be neglected for our study. It is due to the fact that the frequency we studied is far below the resonance frequency.

In this section, analytical results are used to verify the FE model. It has to be noted that the analytical results are not 100% accurate because some assumptions and simplifications have to be made to derive these models as well. It even may be true that the simulated results are more accurate than the analytical ones. But since there is no experimental reference for the

work described in section 8.2, before the FE model is verified the analytical results are the only references that can be used.

8.2.1 Computer model

Steinmann et al. studied whether the sensor diaphragm should be treated as a plate or a membrane [8-2]. In the ideal case a "membrane" is a physical element, which has only the capability to carry in-plane tensile stresses. It has no flexural rigidity at all. An ideal "plate" is an element in which the in-plane stresses are negligible. [8-2] pointed out that by increasing the in-plane stress the real physical deflection shape of the diaphragm becomes more and more the shape of a pure membrane. In our case, the diaphragm of the condenser microphone has very high tensile stress. Therefore, it is treated as a membrane.

A comparison between simulated results by using different element types to model a microphone diaphragm had been made in [8-3]. A 4-node shell element, a 16-node shell element, and an 8-node 2-D solid element were used to make the simulation. The results showed that according to the deflection the variation in the results was less than 0.3%, which means that the FEM analysis converged to the same answer regardless of the element types. Therefore the simplest element should be chosen to reduce the calculating time.

We choose element type Shell63 defined by ANSYS [8-4] shown in Fig. 8.1 to make the computer model. ① to ⑥ denote the face. *I, J, K* and *L* denote the node. The element has both bending and membrane capabilities. Both in-plane and normal loads are permitted, which is necessary for our case with in-plane tensile stress and normal pressure load. The element has six degrees of freedom at each node: translation in the nodal x, y and z directions and rotations about the nodal x, y and z-axes. Stress stiffening and large deflection capabilities are included. The thickness is assumed to vary smoothly over the area of the element, with the thickness input at the four nodes.

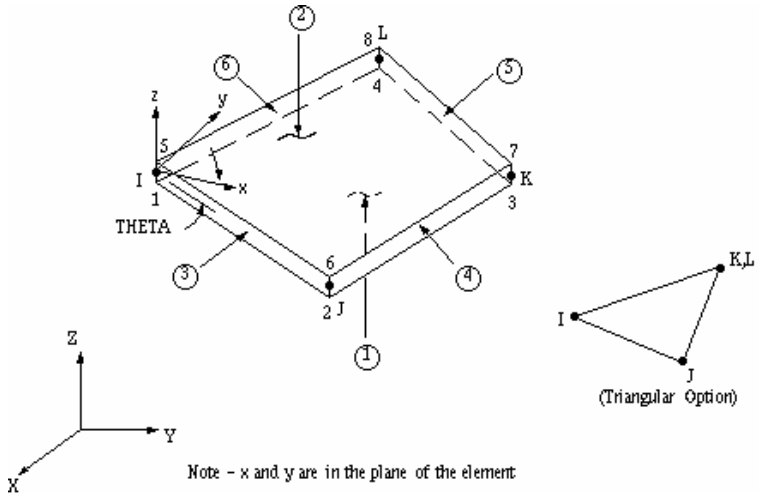

Fig. 8.1: Shell63 elastic shell.

A test of mesh density is made first. We take the first resonance frequency of a circular diaphragm as the tested parameter. Table 8.1 shows the simulated results with different mesh

densities when the diaphragm properties are the same as those listed in Table 8.2. Analytical resonance frequency, according to eqn. (7.10), is 75500 Hz.

Table 8.1: Simulated first resonance frequency with different mesh densities.

Element number	72	162	288	648	1152	1800
Resonance frequency	75000	75200	75300	75400	75400	75400
Deviation	-0.6%	-0.3%	-0.2%	-0.1%	-0.1%	-0.1%
Calculation time	8 seconds	15 seconds	36 seconds	3 minutes 20 seconds	14 minutes	54 minutes 30 seconds

It can be seen that the density of FE mesh influences the simulation accuracy. With finer mesh density, we can obtain more accurate simulated resonance frequency compared to the analytical one, which is the only available reference, but the calculation takes more time.

Since the analytical results are not the exact values as mentioned at the beginning of the section, to some extent the calculation time is more important than the accuracy. We choose 162 elements for the following simulation.

8.2.2 A circular diaphragm with a same radius backplate

We assume that the studied diaphragm with tensile stress is ideally clamped at the edge. The properties used in this section are shown in Table 8.2.

Table 8.2: The properties of the microphone.

Properties of the microphone	Value
Young's modulus E	$3\times10^{11}\ Pa$
Poisson's ratio ν	0.3
Density ρ	2300 kg/m^3
Radius R	1.95 mm
Thickness h	0.5 μm
Air gap d_0	20 μm
Tensile stress σ	$340\times10^{6}\ Pa$

Resonance frequency

The first resonant mode of the circular diaphragm is shown in Fig. 8.2. The number on the right is the displacement. The grid is the outline of the elements. It can be seen from the figure that the first resonance frequency is 75234 Hz, which is shown as FREQ=75234 in Fig. 8.2.

Fig. 8.3 shows the comparison between the analytical and simulated results. As expected, though a good agreement is achieved, there is a relative big difference at zero prestress. At zero prestress, the analytical first resonance frequency is zero, but the simulated results show that it is not zero. The reason is that the bending rigidity of a membrane is neglected in the analytical model, but not in the FE model. Since the practically used diaphragm for condenser

microphones has more than 100 MPa tensile stress, this zero-difference does not need to be considered.

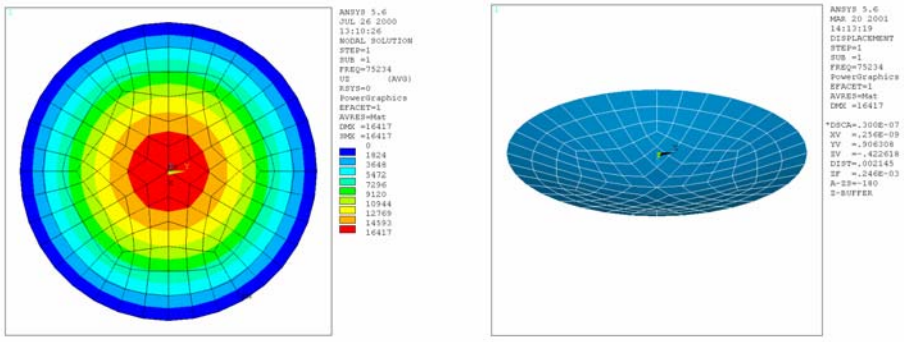

Fig. 8.2: The first resonant mode of the circular diaphragm.

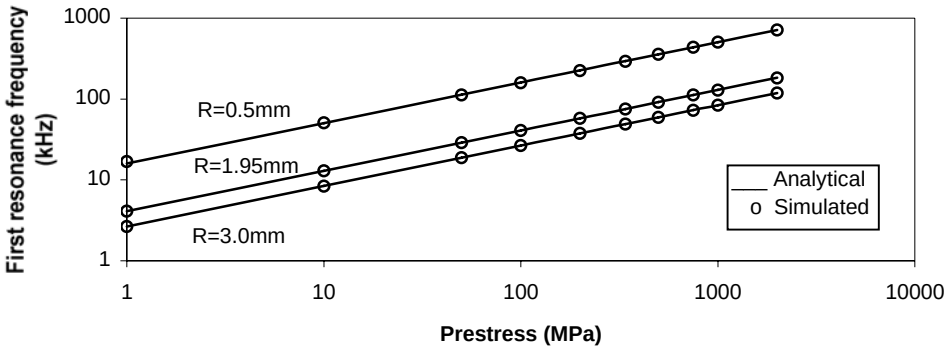

Fig. 8.3: The first resonance frequency as a function of the prestress.

During the computer simulation, there are two methods to change the tension of the diaphragm, applying tensile stress to the diaphragm directly and changing the diaphragm temperature. Both methods can be used to define a prestress in a circular diaphragm, but it is difficult for the first method to define a prestress in an octagonal diaphragm evenly. Since an octagonal diaphragm will be studied in the next chapter and we want to maintain the continuity of the simulated results, we take the second method, changing the diaphragm temperature, to stretch the diaphragm.

Though the two methods apply the exactly same tensile stress to the circular diaphragm, Table 8.3 shows that the simulated first resonance frequencies are different. From a practical point of view, the difference is so small that it can be neglected. But from a simulation point of view, the result should be exactly same because the exactly same model was used. So far the reason for the difference is unknown.

Table 8.3: The first resonance frequency.

Analytical result	FE simulated result		Deviation
75.5 kHz	Applying stress	75.5 kHz	0.01%
	Changing temperature	75.2 kHz	-0.3%

Static deflection profile

The static deflection profile of an ideal circular membrane, which is tensile stressed, is [8-5]:

$$d(r) = d(0) \cdot \left(1 - \frac{r^2}{R^2}\right) \tag{8.1}$$

where the center deflection *d(0)* is expressed as

$$d(0) = \frac{R^2}{4\sigma h} P \tag{8.2}$$

From the above two equations, we have

$$\frac{d(r)}{d(0)} = 1 - \left(\frac{r}{R}\right)^2 \tag{8.3}$$

which means though the diaphragm radius R can be different, as long as r/R is the same, the normalized deflection is the same. Fig. 8.4 illustrates it.

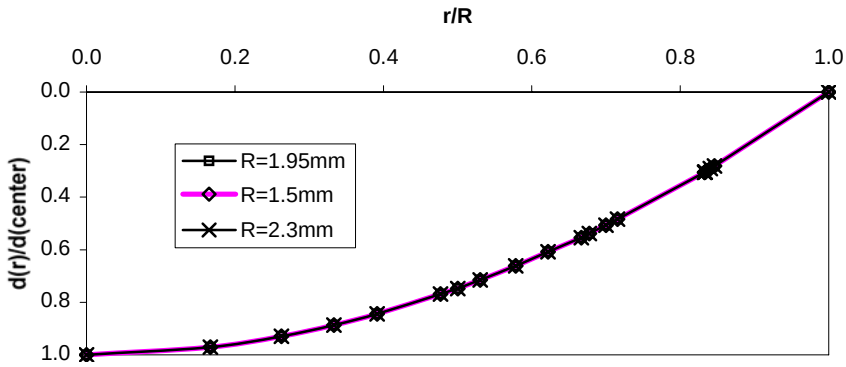

Fig. 8.4: Normalized deflection profiles for circular diaphragms of different sizes.

Collapse voltage

Rewriting eqn. (7.12) gives

$$F_{el} = \frac{1}{2}\varepsilon_0 \left[\frac{V}{d_0 - d(r)}\right]^2 \tag{8.4}$$

Eqn. (8.4) describes the electrostatic force between the diaphragm and the backplate. It can be seen that the electrostatic force F_{el} is dependant on the diaphragm deflection, while the diaphragm deflection is depending on the magnitude of the electrostatic force. Since this is a non-linear system, the diaphragm deflection can only be calculated using an iterative procedure. The flowchart is shown in Fig. 8.5.

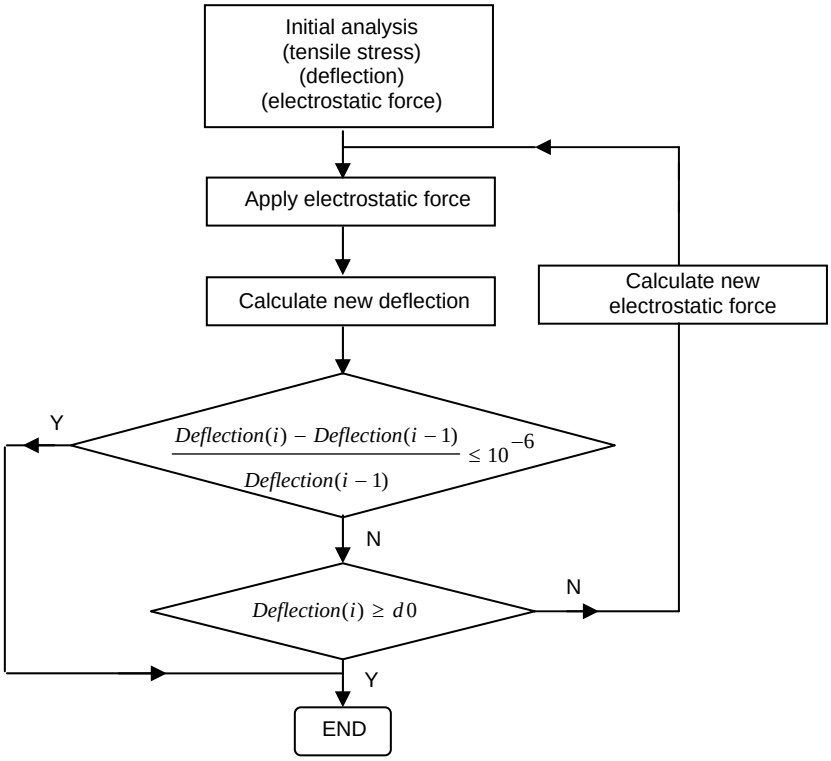

Fig. 8.5: The flowchart for the electrostatic force calculation.

The criteria to stop the loop are either the calculation is converged by $\frac{Deflection(i)-Deflection(i-1)}{Deflection(i-1)} \le 10^{-6}$ or the collapse happens by $Deflection(i) \ge d_0$, where i denotes the step of iteration, $Deflection(i)$ denotes the center deflection of the diaphragm at the i[th] iteration.

10^{-4} is chosen based on the results given by Warren [8-6] which says that "the accuracy of the highest stable value found was not greatly changed when the critical edge deflection value was less than 10^{-4}". It should be noted that what Warren mentioned is the critical edge deflection value while what we talk about is the center deflection value.

Fig. 8.6, 8.7 and 8.8 show the comparison between the Warren's [8-6] and simulated collapse voltage of a circular diaphragm with different diaphragm radii, different air gap distances and different tensile stresses, respectively. The properties of the microphone are shown in Table 8.2 except the varied parameter. R=R_B=1.95mm, h=0.5 μm. The figures show that very good agreements are achieved between the Warren's results and the FE simulated results.

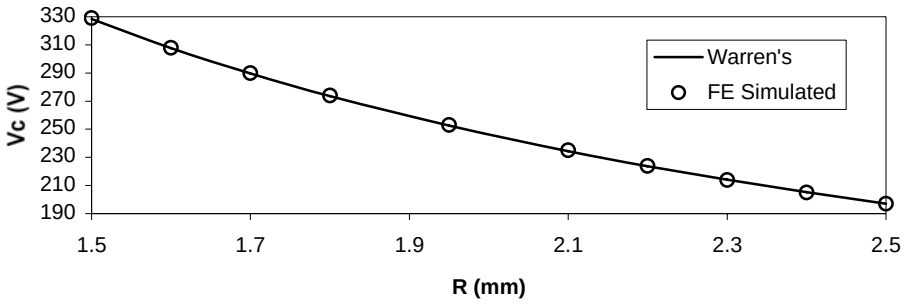

Fig. 8.6: Collapse voltage as a function of the diaphragm radius.

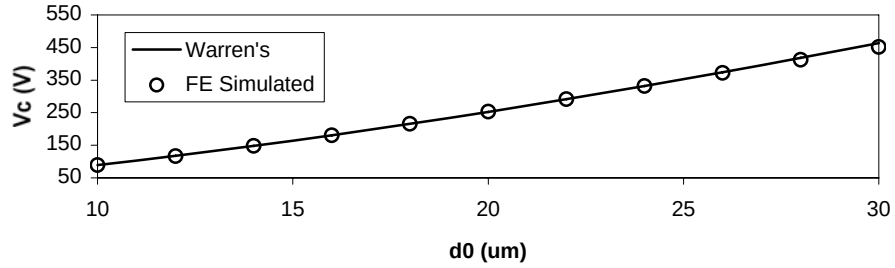

Fig. 8.7: Collapse voltage as a function of the air gap distance d_0.

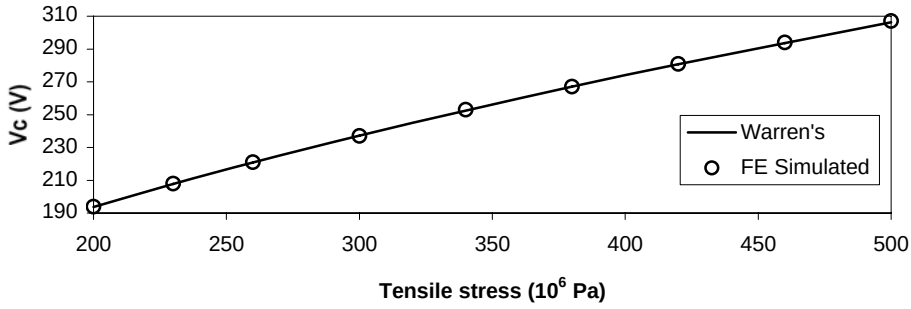

Fig. 8.8: Collapse voltage as a function of tensile stress.

The studies on the resonance frequency, the deflection profile and the collapse voltage show that the computer model can be used to make the further simulation.

8.2.3 A circular diaphragm with a smaller radius backplate

As we have shown that the computer model for a circular microphone with a same radius backplate works, we can make further simulation with the same way for a circular diaphragm with a smaller backplate, we have reference [8-7] for the study.

Table 8.4 shows the simulated collapse voltage for different backplate radii while the properties of the microphone are taken from Table 8.2. R=1.95mm.

Table 8.4: Collapse voltage for different backplate radii.

R_B (mm)	1.95	1.8	1.7	1.6	1.5	1.4	1.3	1.2	1.1	1.0	0.9
Simulated collapse voltage V_c (V)	253	253	255	258	262	267	274	283	294	308	325

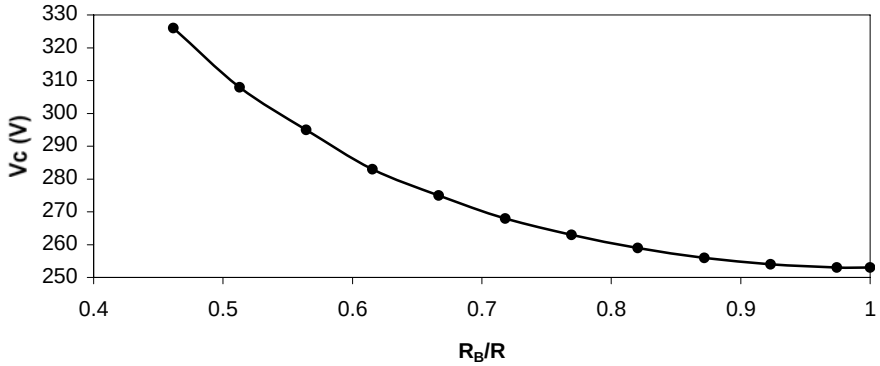

Fig. 8.9: Collapse voltage as a function of the ratio between the backplate and the diaphragm radius.

It can be seen that the collapse voltage becomes bigger as the backplate radius becomes smaller. Warren arrived at the same conclusion in [8-7]. The reason is that the decreased area of the stationary electrode (the backplate) decreases the total electrostatic forces acting on the diaphragm, therefore causes the increase of the collapse voltage.

A polynomial fitting function for the collapse voltage based on Fig. 8.9 is expressed as

$$V_c(\lambda) = (622 - 1010 \cdot \lambda) + 918 \cdot \lambda^2 - 276 \cdot \lambda^3 \tag{8.5}$$

where $\lambda = R_B / R$. The equation fits the simulations (dots in Fig. 8.9) within 1%.

Fig. 8.10 shows the normalized deflection of the diaphragm with 80% of the collapse voltage. The properties used are all taken from Table 8.2. The diaphragm radius is 1.95mm.

For a full size backplate R_B=1.95mm=R, the deflection shape in Fig. 8.10 is very close to the parabolic shape, which was derived for a uniformly loaded diaphragm. When the backplate is smaller than the diaphragm, the electrostatic forces are no longer acting on the complete diaphragm. The smaller the backplate radius, the more the loading due to the electrostatic force gets concentrated at the center of the diaphragm, and the more the shape starts deviating from the parabolic shape.

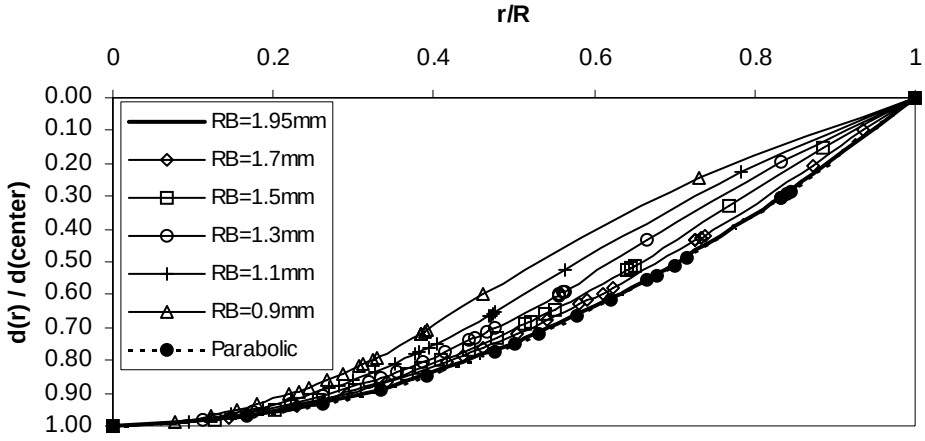

Fig. 8.10: Normalized deflection with 80% of V_c.

8.3 Experimental verification

In order to verify the simulated results, we measured two B & K Type 4190 microphones, series number 2238314 and 2237921. A comparison between the measured and simulated results is made for both microphones.

Type 4190 is a Free-field ½" microphone for general sound measurements and for standardized noise measurements. The microphone requires an external polarization voltage of 200V. The backplate has 14 holes. Since during manufacturing each microphone will be adjusted manually to meet the assigned specifications, there is no way to obtain the 100% accurate properties for each microphone. Therefore, the specified values are used. They are shown in Table 8.5 [8-8].

In this analysis several simplifying assumptions have been made. First, it has been assumed that the diaphragm is under isotropic tension, which remains constant as the diaphragm moves. Because the range of the diaphragm dynamic deflections is relatively small (1 to 20 μm), the assumption is valid.

Table 8.5: Specified properties of Type 4190 microphone.

Properties	Value
Young's modulus E	$20\times10^{10}\ Pa$
Poisson's ratio ν	0.3
Density ρ	8300 kg/m^3
Diaphragm radius R	4.6 mm
Backplate radius R_b	3.45 mm
Diaphragm thickness h	2.35 μm

Second, it has been assumed that the bending rigidity of the diaphragm is insignificant compared to the tensile restoring force. For the diaphragm of Type 4190 using stainless steel alloy, this assumption is correct.

Third, it has been assumed that the damping can be neglected. It is due to the fact that the frequency we studied is far below the resonance frequency.

Fig. 8.11 presents the profile of the model. The grid denotes the outline of the elements. The diaphragm is divided into three parts, which are the cyan parts overlapping with the backplate holes, the blue part overlapping with the backplate, and the purple part.

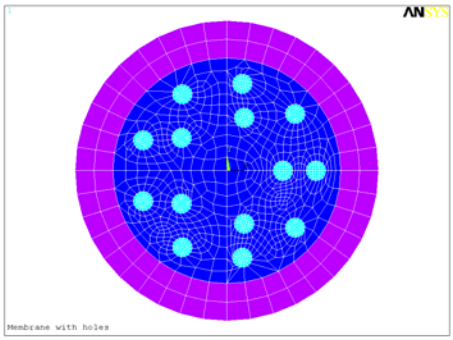

Fig. 8.11: The profile of the model.

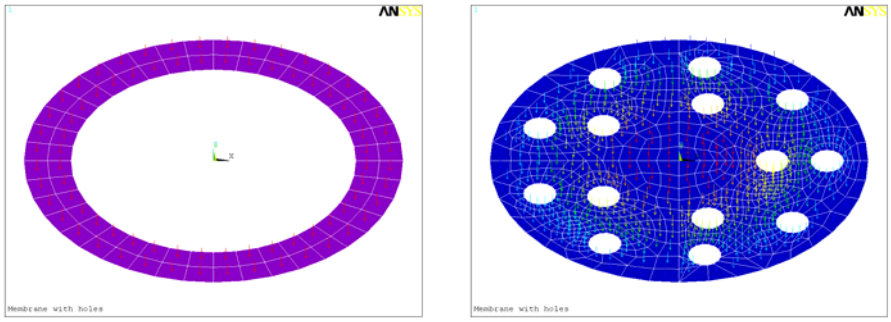

(a) (b)

Fig. 8.12: The normal pressure applied to the model.

During the simulation, the sound pressure and the rear volume pressure are applied on the purple and cyan parts shown in Fig. 8.12(a). The sound pressure, the rear volume pressure and the electrostatic force are applied on the blue part shown in Fig. 8.12(b). The arrow denotes the pressure direction.

Fig. 8.13 shows the distribution of the z-direction displacement of the diaphragm. The external polarization voltage is 200V.

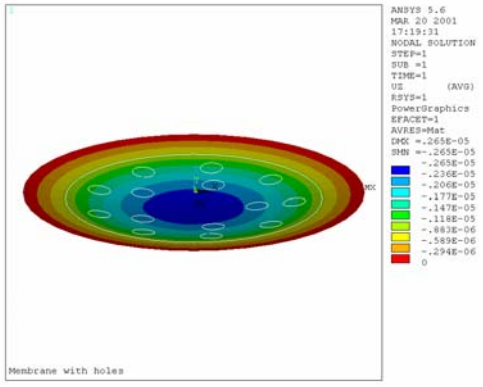

Fig. 8.13: The z-direction displacement.

Once the microphone is assembled some physical parameters are known, except the diaphragm tensile stress, the air gap distance and the parasitic capacitance. The scheme shown in Table 8.6 is used to determine the unknown parameters and then use these parameters to predict (1) the capacitance as a function of the polarization voltage, and (2) the open-circuit sensitivity of the microphone.

Table 8.6: Experimental procedure for verification of the FE model.

Measurement	Assumed Parameters	Derived Paramter
(1) Vacuum resonance frequency	Diaphragm thickness 2.35 μm Diaphragm radius 4.6 *mm* Diaphragm density 8300 kg/m^3	Diaphragm stress
(2) Collapse voltage	Diaphragm stress from (1) Diaphragm thickness 2.35 μm Diaphragm radius 4.6 *mm* Backplate radius 3.45 *mm* Hole geometry of the backplate	Air gap distance
(3) Capacitance at 0 V	Backplate radius 3.45 *mm* Hole geometry of the backplate Air gap distance from (2)	Parasitic capacitance
(4) Capacitance measured at 100 kHz	All parameters used and derived in (1) to (3)	
(5) Open-circuit sensitivity	All parameters used and derived in (1) to (3)	

The methods presented in the literature to estimate the tension in the diaphragm may be classified into three main categories: one is based on the relationship between the diaphragm tension and the static displacement of the diaphragm [8-9, 10], the second one is based on finding the tension from the resonance frequency of the diaphragm [8-11], the third one is based on the measurement of the electric admittance of the condenser microphone cartridge [8-12]. This thesis uses the second method to predict the tension in the diaphragm. Table 8.7 shows the results of Step 1.

Table 8.7: The diaphragm stress.

	Vacuum resonance frequency	Diaphragm stress
2238314	14 kHz	236 MPa
2237921	13.5 kHz	219 Mpa

Since it is difficult to measure the air gap distance, as Step 2 shows, the air gap distance is derived from the collapse voltage. The results are shown in Table 8.8.

Table 8.8: The air gap distance.

	Collapse voltage	Air gap distance
2238314	298 V	25.1 μm
2237921	298 V	25.7 μm

8.3.1 Capacitance

The diaphragm displacement can be measured directly by using laser interferometry, as for instance used by Warren [8-6]. However the measuring procedure is complicated. Therefore we have chosen an indirect method, which is to measure the capacitance determined by the separation between the diaphragm and the backplate. This method is experimentally easy and fast to be used.

In order to make the description easier, it is necessary to give the definitions of the microphone capacitances used in this section.

C_{00} is the capacitance with no diaphragm deflection, which means the microphone does not have a polarization voltage. C_0 is the capacitance with a static diaphragm deflection due to the polarization voltage, which is constant, where $d_0(r)$ is the static displacement of diaphragm. C_m is the time-varying capacitance due to the dynamic diaphragm motion, which is caused by the input sound pressure and the polarization voltage, where $d(r)$ is the displacement of the diaphragm.

$$C_{00} = \varepsilon_0 \frac{\pi R^2}{d_0} \tag{8.6}$$

$$C_0 = \varepsilon_0 \int_0^R [\frac{2\pi r}{d_0 - d_0(r)}] dr \tag{8.7}$$

$$C_m = \varepsilon_0 \int_0^R [\frac{2\pi r}{d_0 - d(r)}] dr \tag{8.8}$$

The microphone capacitance consists of the diaphragm-backplate capacitance C_m and the parasitic capacitance C_p, which is the backplate-housing capacitance. Since the simulated C_{00} does not include the parasitic capacitance while the measured C_{00} does, the difference between them is C_p.

The comparisons between the measured and simulated microphone capacitances of 2238314 and 2237921 as a function of the applied bias voltage are shown in Fig. 8.14 and Fig. 8.15, respectively. The measured capacitance is obtained by exciting the microphone with a 100 kHz signal while the polarization voltage is varied from 0V to 250V.

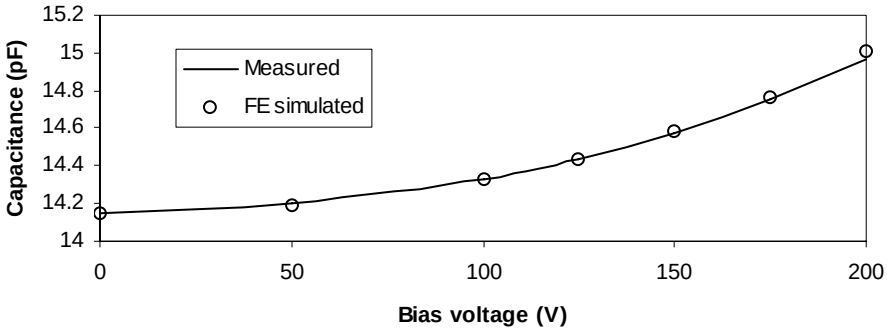

Fig. 8.14: Capacitance comparison of 2238314.

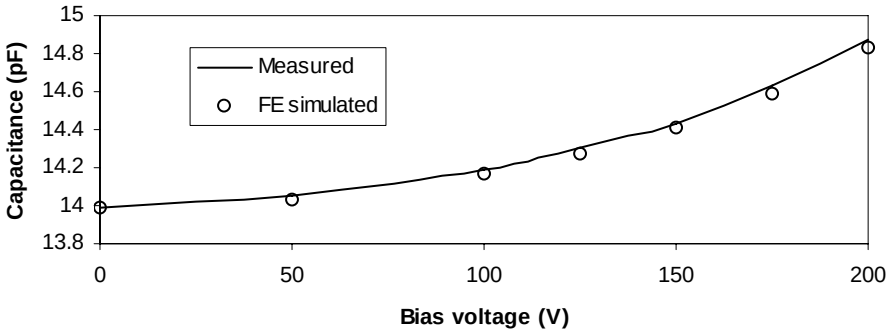

Fig. 8.15: Capacitance comparison of 2237921.

As shown in Fig. 8.14 and 8.15, the capacitance increases almost exponentially as the applied bias voltage increases. Two figures indicate a good agreement between the simulated and measured results.

8.3.2 Open-circuit sensitivity

Analytical model of the open-circuit sensitivity for a diaphragm with a smaller backplate can be derived from [8-13].

Fig. 8.16 illustrates a simplified microphone consisting of dynamic capacitance C_m, load resistance R_b, and input capacitance C_i.

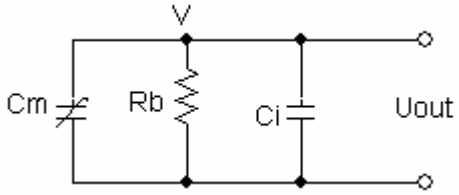

Fig. 8.16: A simplified electrical circuit of a microphone.

When the charge Q_0 is kept constant, the voltage across capacitances with the diaphragm and the backplate at rest position V_0 (external polarization voltage) will vary to V with the variation of the active capacitance that is caused by the sound pressure. Therefore based on the output voltage change during the operation, the open-circuit sensitivity can be predicted.

$$V \cdot (C_m + C_i) = Q_0 = V_0 \cdot (C_{00} + C_i) \tag{8.9}$$

Rewriting eqns. (8.1), (8.6) and (8.8) for circular pre-stressed diaphragm with holes we have:

$$d(r) = d(0) \cdot \left(1 - \frac{r^2}{R^2}\right) \tag{8.10}$$

$$C_{00} = R_s \cdot \varepsilon_0 \cdot \frac{\pi R_B^{\ 2}}{d_0} \tag{8.11}$$

$$C_m = R_s \cdot \varepsilon_0 \int_0^{R_B} [\frac{2\pi r}{d_0 - d(r)}] dr \tag{8.12}$$

where $R_s = \dfrac{\pi \cdot R_B^2 - n \cdot \pi \cdot R_h^2}{\pi \cdot R_B^2}$, n is the number of holes, R_h is the radius of the hole by assuming the holes have same radius.

Simplification and integration of the above equations lead to:

$$\begin{aligned} C_m &= R_s \cdot \frac{\varepsilon_0 \cdot \pi \cdot R_B^2}{d_0} \cdot R_B^{-2} \cdot \int_0^{R_B} \frac{2 \cdot r}{1 - y \cdot \left(1 - \dfrac{r^2}{R^2}\right)} dr \\ &= C_{00} \cdot (1-k)^2 \cdot y^{-1} \cdot \ln \frac{1+y}{1+k \cdot y} \end{aligned} \tag{8.13}$$

where $k = 1 - \dfrac{R_B^2}{R^2}$ and $y = \dfrac{d(0)}{d_0}$.

Inserting eqns. (8.11) and (8.13) into eqn. (8.9) gives the output voltage as:

$$V = V_0 \cdot \frac{C_{00} + C_p}{C_{00} \cdot (1-k)^{-1} \cdot y^{-1} \cdot \ln \dfrac{1+y}{1+k \cdot y} + C_p} \tag{8.14}$$

Taylor series expansion of eqn. (8.14) leads to:

$$\begin{aligned} V &= V_0 + V_0 \cdot \frac{k+1}{2} \cdot \frac{C_{00}}{C_{00}+C_p} \cdot \left(y + F_2 \cdot y^2 + F_3 \cdot y^3 + ...\right) \\ &= V_0 + V_0 \cdot \frac{k+1}{2} \cdot \frac{C_{00}}{C_{00}+C_p} \cdot \frac{d(0)}{d_0} \end{aligned} \tag{8.15}$$

where F_2 and F_3 are functions of the parameter k and thus of the ratio between the backplate and diaphragm radii, which are neglected here.

According to eqn. (8.15), we have,

$$\frac{dV}{d(d(0))} = V_0 \cdot \frac{k+1}{2} \cdot \frac{C_{00}}{C_{00}+C_p} \cdot \frac{1}{d_0} \tag{8.16}$$

Therefore, the analytical open-circuit sensitivity can be derived as:

$$S_0 = \frac{d(d(0))}{dP} \cdot \frac{dV}{d(d(0))} = \frac{R^2}{4\sigma h} \cdot \frac{V_0}{2d_0} \cdot (2 - \frac{R_B^2}{R^2}) \tag{8.17}$$

where R_B and R are the radius of the backplate and the diaphragm, respectively, V is the polarized voltage, σ is the tensile stress of the diaphragm, h is the thickness of the diaphragm, d_0 is the air gap distance.

According to the derivation of eqn. (8.17), it can be seen that the mechanical and electrical coupling effect was not considered.

Another method to calculate the open-circuit sensitivity is the FE simulation that considers the complete coupling effect. Fig. 8.17 gives the flowchart for the calculation.

Taking the same two B & K 4190 microphones used for capacitance studying in last section, a comparison can be made among calibration, analytical estimation and FE simulation for open-circuit sensitivity. It can be seen that FE simulation is more accurate then the analytical estimation.

Table 8.9: Open-circuit sensitivity of 2238314.

	Calibration	Analytical estimation	FE simulation
2238314	47.8 mV/Pa	54.6 mV/Pa	48.55 mV/Pa

The FE simulated sensitivity as a function of applied sound pressure is shown in Fig. 8.18 and 8.19. Fig. 8.18 shows that with low sound pressure, the curve is not very smooth. This can be caused by numerical error, which should be reduced by changing the convergence criterion. However this increases the calculation time. Therefore it is better to use a sound pressure for example 6 to 8 *Pa* to calculate the sensitivity.

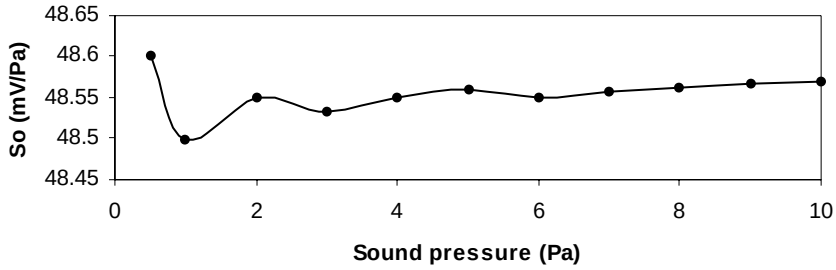

Fig. 8.18: The open-circuit sensitivity at low sound pressure of 2238314.

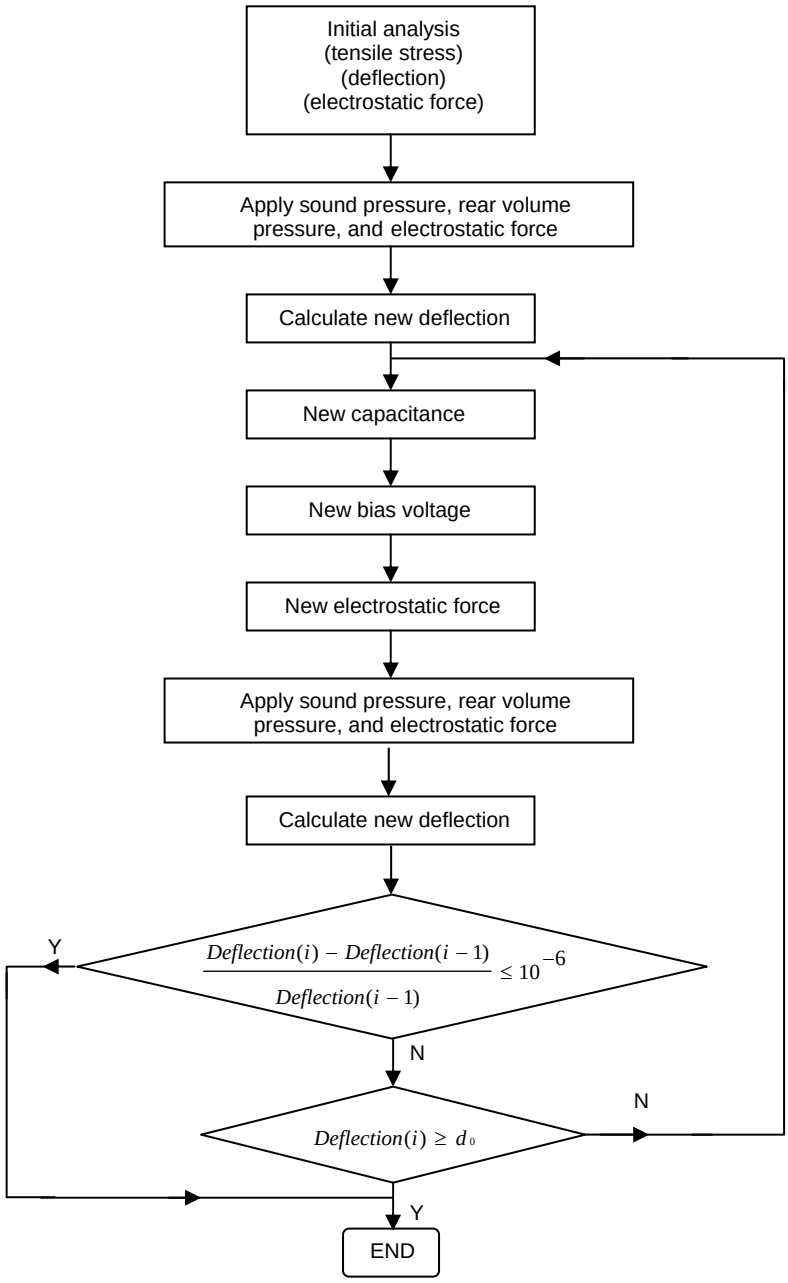

Fig. 8.17: The flowchart for the open-circuit sensitivity calculation.

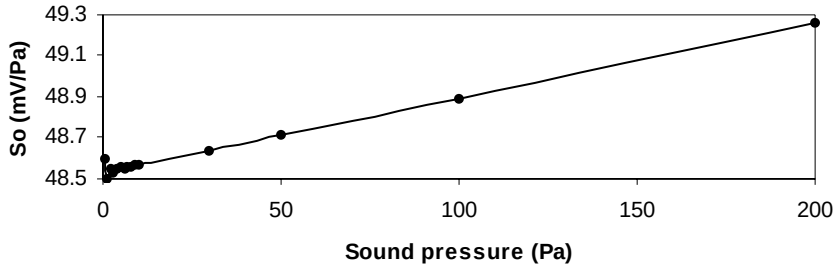

Fig. 8.19: The open-circuit sensitivity of 2238314.

The sound pressure 20 *Pa* corresponds to 120 *dB* (re 20 μPa) while 200 *Pa* corresponds to 140 *dB* (re 20 μPa). In Fig. 8.18, between 2 and 10 *Pa*, the sensitivity is almost constant. Above 20 *Pa*, there is a notable increase in sensitivity with the sound pressure as shown in Fig. 8.19. This nonlinearity gives a distorted output signal at high sound levels. Eqn. (8.15) shows that the larger the backplate becomes, the higher the distortion is. Practically the bigger the applied sound pressure, the bigger the diaphragm deflection. This is why there is distortion at the high sound pressure level as shown in Fig. 8.19.

Fig. 8.19 indicates that the distortion at sound pressure 200 *Pa* is 1.55%. It has to be stated that this distortion presents different information regarding to the distortion described in [8-13]. After making FFT analysis with the results shown in Fig. 8.19, we can obtain the result of the distortion defined in [8-13]. But this work has not been done.

In order to avoid any occasional simulation results, the sensitivity of 2237921 is calculated. Table 8.10 shows that the FE simulation is more accurate than the analytical estimation. The FE simulated open-circuit sensitivity as a function of applied sound pressure is presented in Fig. 8.20.

Table 8.10: Open-circuit sensitivity of 2237921.

	Calibration	Analytical estimation	FE simulation
2238314	50.2 mV/Pa	57.5 mV/Pa	50 mV/Pa

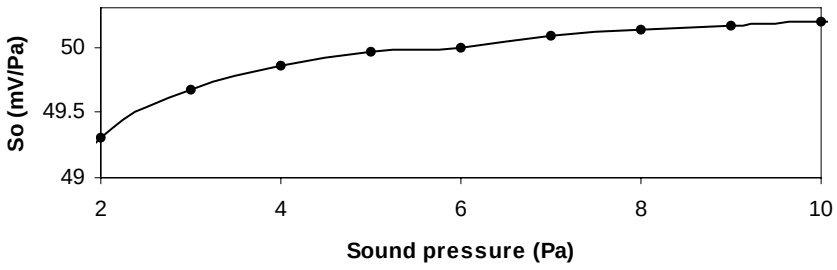

Fig. 8.20: The open-circuit sensitivity of 2237921.

During the sensitivity simulation, large deflection effect is not included because the big sound pressure is not considered. Fig. 8.21 shows that when the sound pressure is smaller than 1000 Pa, whether the large deflection effects is included or not does not influence the simulated results.

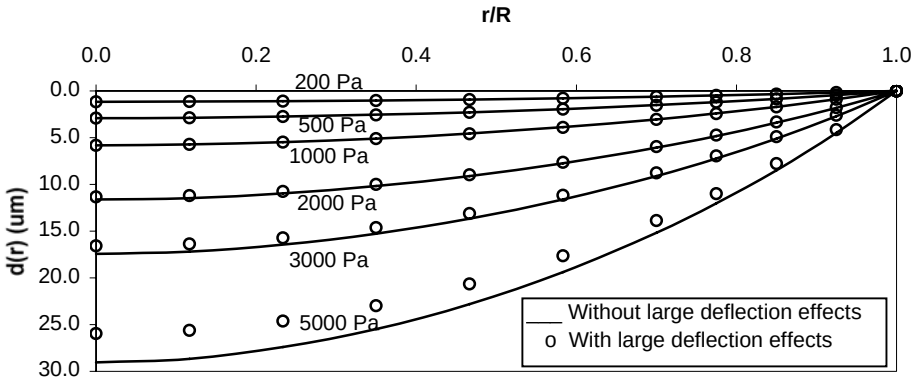

Fig. 8.21: The large deflection effects.

So far the experimental verifications have substantiated that the FE circular condenser microphone modeling is successful and gives much better results than analytical modeling.

8.4 Optimization of the backplate

The microphone diaphragm has the largest vibration amplitude at center. Therefore most of the signal is generated at the diaphragm center. The edge region of the diaphragm does not contribute much to the signal, but adds to the parasitic capacitance. Therefore, the outer region of the backplate only attenuates the microphone signal, thereby reducing the sensitivity and the Signal/Noise ratio. Calculating the sensitivity for different backplate radii, an optimized value of the backplate radius can be found.

Voorthuyzen [8-14] has presented an analytical modal to optimize the radius of the backplate for a capacitive microphone with a stress free diaphragm. The diaphragm deflection profile is described by a fourth-order polynomial. This section gives an optimization theory analogous to the one presented in [8-14], but for a diaphragm with a parabolic deflection profile.

8.4.1 Analytical analysis

Redrawing Fig. 8.16 as Fig. 8.22 gives us:

$$Q_0 = (C_m + C_i) \cdot V \tag{8.18}$$

where Q_0 is the charge, C_m is the dynamic capacitance, C_i is the input capacitance, V is the output voltage.

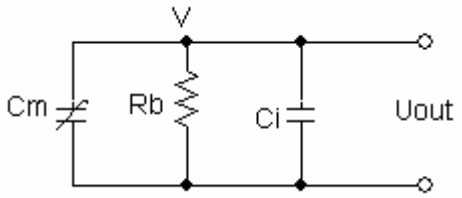

Fig. 8.22: A simplified electrical circuit of a microphone.

After differentiating eqn. (8.18) with respect to the pressure, we have:

$$\frac{d}{dP}Q_0 = \frac{d}{dP}(C_m + C_i)\cdot V \tag{8.19}$$

Since the microphone operates at frequencies $\omega >> (R_b \times C_m + C_i)^{-1}$, the static charge Q_0 is constant, which is

$$\frac{d}{dP}Q_0 = 0 \tag{8.20}$$

Inserting eqn. (8.18) into eqn. (8.20), we have

$$[\frac{d}{dP}(C_m + C_i)]\cdot V + (\frac{d}{dP}V)\cdot(C_m + C_i) = 0 \tag{8.21}$$

The microphone sensitivity is defined as the ratio between *dP*, a small change of the pressure acting on the diaphragm, and *dV*, the resulting change of the voltage across the two plates.

$$S = \frac{d}{dP}V = \frac{-V}{C_m + C_i}\cdot\frac{d}{dP}C_m \tag{8.22}$$

where C_i has a fixed value, which means $\frac{d}{dP}C_i = 0$.

We define the backplate radius as $\lambda \times R$ with $0 \le \lambda \le 1$, then the microphone capacitance, C_m, can be expressed as:

$$\begin{aligned} C_m &= \varepsilon_0 \cdot 2\pi R^2 \cdot \int_0^{\lambda} \frac{\zeta}{d_0 - d(0)\cdot(1-\zeta^2)}\,d\zeta \\ &= \frac{\varepsilon_0 \cdot \pi R^2}{d_0}\cdot\frac{d_0}{d(0)}\ln\frac{1 - d(0)/d_0 + \lambda^2 \cdot d(0)/d_0}{1 - d(0)/d_0} \end{aligned} \tag{8.23}$$

Taylor series expansion of the *ln*-term for small normalized deflections α, $\alpha = d(0)/d_0$, is as following:

$$\frac{1}{\alpha}\cdot\ln\left[\frac{1-\alpha+\alpha\cdot\lambda^2}{1-\alpha}\right]=\lambda^2+\left[\frac{1}{2}\cdot\left(-\lambda^2+1\right)\cdot\left(\lambda^2-1\right)+\frac{1}{2}\right]\cdot\alpha+O(\alpha^2) \tag{8.24}$$

According to eqn. (8.24), eqn. (8.23) can be rewritten as:

$$\begin{aligned} C_m &= \frac{\varepsilon_0\cdot\pi R^2}{d_0}\cdot\left[\frac{1}{\alpha}\cdot\ln\left[\frac{1-\alpha+\alpha\lambda^2}{1-\alpha}\right]\right] \\ &= \frac{\varepsilon_0\cdot\pi R^2}{d_0}\cdot\left[\lambda^2+\left[\frac{1}{2}\cdot\left(-\lambda^2+1\right)\cdot\left(\lambda^2-1\right)+\frac{1}{2}\right]\cdot\alpha\right] \end{aligned} \tag{8.25}$$

We define $C_{00}=\varepsilon_0\cdot\dfrac{\pi R^2}{d_0}$ and $\alpha=\dfrac{P\cdot R^2}{d_0\cdot 4\sigma_0 h}=K_p\cdot P$, then eqn. (8.25) becomes:

$$\begin{aligned} C_m &= C_{00}\lambda^2+\left[\frac{1}{2}\left(-\lambda^2+1\right)\cdot\left(\lambda^2-1\right)+\frac{1}{2}\right]\cdot C_{00}K_pP \\ &= C_{00}\lambda^2\left[1+\frac{1}{2}K_p\cdot P\cdot\left(2-\lambda^2\right)\right] \end{aligned} \tag{8.26}$$

Inserting eqn. (8.26) into eqn. (8.22) by omitting the second term of eqn. (8.26), we have:

$$\begin{aligned} S &= \frac{d}{dP}V=\frac{-V}{C_m+C_i}\cdot\frac{d}{dP}C_m \\ &= \frac{-V}{C_{00}\lambda^2+C_i}\cdot\frac{d}{dP}\left[\frac{1}{2}\left(-\lambda^2+1\right)\cdot\left(\lambda^2-1\right)+\frac{1}{2}\right]\cdot C_{00}K_pP \\ &= \frac{-V}{C_{00}\lambda^2+C_i}\cdot\left[\left(-\frac{1}{2}\lambda^2+\frac{1}{2}\right)\cdot\left(\lambda^2-1\right)+\frac{1}{2}\right]\cdot C_{00}K_p \end{aligned} \tag{8.27}$$

After defining $C_n = C_i/C_{00}$, we have the sensitivity as a function of λ and C_n

$$S(\lambda,C_n)=\frac{-V}{\lambda^2+C_n}\cdot\left[\left(-\frac{1}{2}\lambda^2+\frac{1}{2}\right)\cdot\left(\lambda^2-1\right)+\frac{1}{2}\right]\cdot K_p \tag{8.28}$$

In order to obtain the highest sensitivity we need to find the optimum λ.

$$\frac{d}{d\lambda}S = \frac{d}{d\lambda}\frac{V}{(\lambda^2 + C_n)} \cdot \left[\left(-\frac{1}{2}\lambda^2 + \frac{1}{2}\right)\left(\lambda^2 - 1\right) + \frac{1}{2}\right] \cdot K_p$$
$$= -V \cdot \lambda \cdot K_p \cdot \frac{\left(\lambda^4 + 2\lambda^2 C_n - 2C_n\right)}{\left(\lambda^2 + C_n\right)^2} = 0 \tag{8.29}$$

Eqn. (8.23) equals to 0 for λ=0 or $\lambda^4 + 2\lambda^2 C_n - 2C_n = 0$. We can obtain the optimized λ, which gives the optimized backplate radius as:

$$\lambda_{\max}(C_n) = \sqrt{-C_n + \sqrt{C_n^2 + 2C_n}} \tag{8.30}$$

8.4.2 Simulated analysis

Since the general optimization procedure is only to optimize the circular microphone geometry, no specific backplate design needs to be considered. The model used does not have holes. The properties of Type 4190 shown in Table 8.5 are used. The analytical results referenced are obtained by eqn. (8.30).

A comparison between the analytical and simulated results in Fig. 8.23 shows that:

(1) The simulated optimized λ as a function of (C_n) is very close to the analytical one obtained by eqn. (8.30). The optimized λ equals to 0.7, 0.8 and 1.0 for C_n equals to 0.33, 1.0 and 3.0, respectively.
(2) The simulated sensitivity is bigger than the analytical one obtained by eqn. (8.28) for the same geometry model.

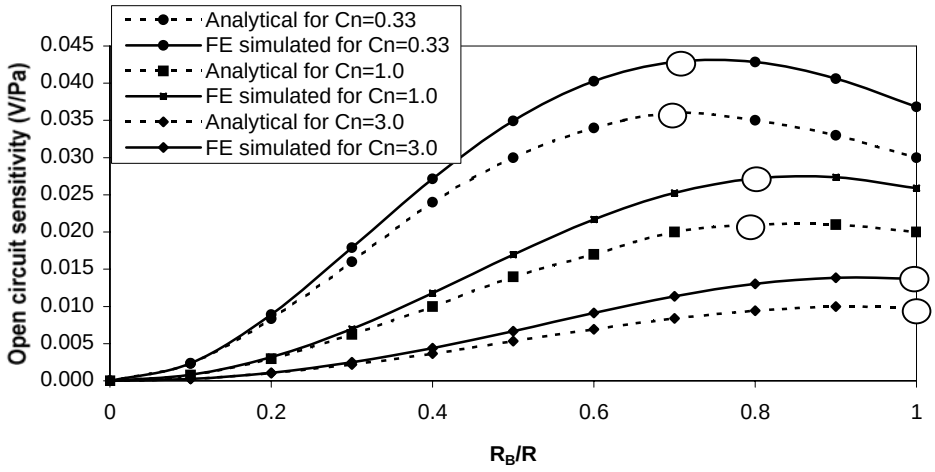

Fig. 8.23: A comparison between the analytical and FE simulated optimization.

8.4.3 Discussion

The analytical model according to eqn. (8.22) ignores the mechanical and electrical coupling effect. Besides, the analytical model takes the assumption that the diaphragm deflection is parabolic. Some simplifications are taken by the analytical model as well. The first one is that $\lambda^2 + \left[\frac{1}{2}\cdot\left(-\lambda^2+1\right)\cdot\left(\lambda^2-1\right)+\frac{1}{2}\right]\cdot\alpha$ is used instead of $\frac{1}{\alpha}\cdot\ln\left[\frac{1-\alpha+\alpha\lambda^2}{1-\alpha}\right]$ for eqn. (8.25). The difference is less than 4%. The second one is that $C_m = C_{00}\lambda^2$ is used instead of $C_m = C_{00}\lambda^2\left[1+\frac{1}{2}K_p\cdot P\cdot\left(2-\lambda^2\right)\right]$ for eqn. (8.27). The difference is less than 8%.

The FE model includes the complete mechanical and electrical coupling effect, considers the actual diaphragm deflection. Therefore, the FE simulated results should be more accurate than the analytical results.

8.5 Conclusion

The simulated results not only show that the computer model is correct by compared with the analytical results and experimental results, but also give us some practically useful information.

(1) Based on Fig. 8.9 and eqn. (8.5), it is easy to estimate the collapse voltage for a circular diaphragm of different backplate radii. It makes it possible for designers to use the biggest bias voltage to achieve the highest sensitivity.

(2) Fig. 8.23 gives the designers a better opportunity to optimize the backplate radius to achieve the highest open-circuit sensitivity.

The unique work presented in this chapter is a new method to simulate the open-circuit sensitivity. A comparison with the experimental results shows that the new method gives a more accurate sensitivity estimation than the analytical method.

The FEM application to the silicon condenser microphone will be presented in the next chapter.

References

8-1 IIene J. Busch-Vishniac, ”Response of an edge-supported circular membrane electret earphone. Part I – Theory”, Acoustical Society of America, 75(3), March 1984, p. 977-989.

8-2 R. Steinmann et al., “Mechanical behavior of micromachined sensor membranes under uniform external pressure affected by in-plane stresses using a Ritz method and Hermite polynomials”, Sensors and Actuators, A, 48(1995), p.37-46

8-3 J.Y. Pan et al., ”Verification of FEM Analysis of Load-Deflection Methods for Measuring Mechanical Properties of Thin Film”, 1990, p.70-73

8-4 ANSYS User Manuel, Version 5.6
8-5 S.P. Timoshenko and S. Woinowsky-krieger, “Theory of Plates and Shells”, McGraw-Hill, London, 2nd edn., 1984
8-6 J.E. Warren and A.M. Brzezinski, “Capacitance-Microphone Static Membrane Deflections”, J. Acoust. Soc. Am., Vol. 52, No. 3, 1972, p.711-719
8-7 J.E. Warren, “Capacitance microphone static membrane deflections: Comments and further results”, J. Acoust. Soc. Am., Vol. 58, No.3, September 1975, p.733-740
8-8 “Microphone Handbook“, Bruel & Kjaer, 1992
8-9 IIene J. Busch-Vishniac, ”Response of an edge-supported circular membrane electret earphone. Part II – Experimental results”, Acoustical Society of America, 75(3), March 1984, p. 990-995.
8-10 M.J. Anderson et al., ”Broadband electrostatic transducers: Modeling and experiments”, J. Acoust. Soc. Am. 97, 1995, p.262-272
8-11 A.J. Zuckerwar, “Theoretical response of condenser microphones”, J. Acoust. Soc. Am. 64, 1978, p.1278-1285.
8-12 X. Yan and M.J. Crocker, “A method for measuring the diaphragm tension of condenser microphones using electric admittance”, J. Acoust. Soc. Am. 108(5), Nov. 2000, p.2145-2150.
8-13 Erling Frederiksen, “Reduction of Non-linear Distortion in Condenser Microphones by Using Negative Load Capacitance”, Technical Review, No.1-1996, Bruel & Kjaer, 1996J.E. Warren, “Capacitance microphone static membrane deflections: Comments and further results”, J. Acoust. Soc. Am., Vol. 58, No.3, September 1975, p.733-740
8-14 J.A. Voorthuyzen et al., ”Optimization of Capacitive Microphone and Pressure Sensor Performance by Capacitor-electrode Shaping”, Sensor and Actuators A, 25-27 (1991), p. 331-336.

9
FEM Applied to Silicon Condenser Microphone

9.1 Introduction

The first microphone fabricated with silicon micro-machining techniques was presented by Royer et al. in 1983 [9-1]. After that, silicon microphones using piezoelectric [9-1, 2], piezoresistive [9-3], capacitive [9-4, 5, 6, 7] and optical measurement principles [9-8, 9] are put forward. Among these microphones, silicon micro-machined capacitive microphones have superior performances. Fig. 9.1 illustrates a silicon condenser microphone.

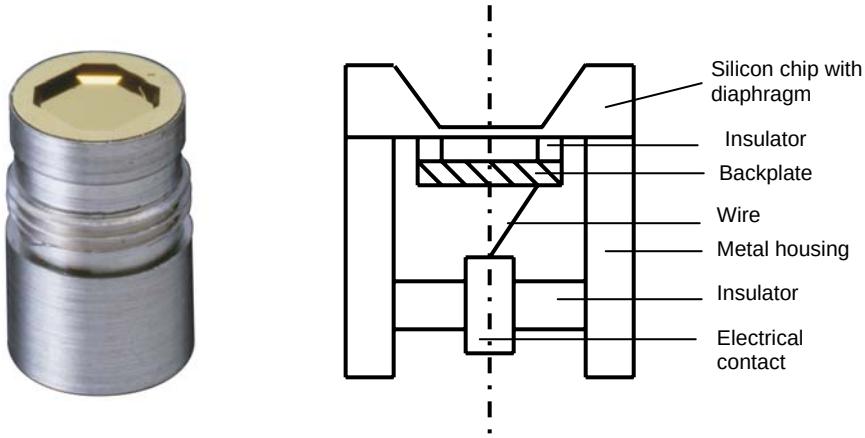

Fig. 9.1: A silicon condenser microphone.

For traditionally manufactured condenser microphones, the design can be made by using the Equivalent Electrical Circuit and trial-and-error, though such methods based design is time consuming and the estimated results are less accurate than those obtained by the FEM as shown in Chapter 8.

For the micro-machined microphones that are fabricated by a sub-supplier (foundry), besides the traditional methods based design is both too expensive and time consuming, there is one more critical problem. The new micro-machined microphone will be very sensitive. This is achieved by applying a new thin ($0.5\,\mu m$) low stress ($340 MPa$) diaphragm technology. Consequently, the microphone will operate closer to the collapse voltage, which makes a careful design optimization more critical than for traditional microphones that operate further from collapse. This critical design optimization, in combination with foundry-based production and product development, cannot be done with traditional modeling and trial-and-error methods. Therefore new design tools are required, such as the FEM based simulation of resonance frequency, collapse voltage and sensitivity.

In this chapter, a literature review of the FE simulation for silicon microphone is presented first. Then the modeling of a silicon condenser microphone is described, including the static study on an octagonal diaphragm, the study on an octagonal diaphragm with a quadratic backplate. Since to our knowledge, we do not have any analytical models or literature reference on octagonal diaphragm, we assume that there will not be a big difference between the properties of an octagonal and a circular diaphragm with the same dimension. Therefore we take the analytical results of a circular diaphragm as reference for the octagonal diaphragm. An experimental verification is made by using B & K silicon condenser microphone. At the end of the chapter, the optimization of the backplate dimension is given.

9.2 Overview of the FE simulation for silicon microphones

Silicon condenser microphone study based on FEM began in the 1990's. In 1990 Pourahmadi presented the work on the modeling of thermal and mechanical stresses in silicon microstructures [9-10]. The modeling of various thin films at different temperature cycles can be used to obtain information about the behavior of the structure at room temperature, about the magnitude of built-in stresses, and about its sensitivity to temperature variations.

Bergqvist presented a method to simulate the sensitivity and frequency response of capacitive microphones in 1993 [9-11]. The FE model of the microphone mechanical structure determines the mechanical stress by changing the temperature. Then the static displacements and stress distributions are outputted. By applying the electrostatic force calculated by an iterative procedure external to ANSYS, the deflection as a function of bias voltage is obtained. Applying a static pressure resulting displacements and change in dynamic capacitance C_m, the open-circuit sensitivity is determined according to

$$S_o = V_0 \cdot \frac{\Delta C_m / C_m}{\Delta P} \cdot \frac{1}{1 + C_p / C_m} \tag{9.1}$$

where V_0 is the external polarization voltage, ΔC_m is the pressure induced change of the microphone dynamic capacitance C_m, C_p is the parasitic capacitance, ΔP is the sound pressure. The sensitivity is valid for the flat part of the microphone frequency response. The complete frequency response is estimated by the combination of the FEM and the Equivalent Circuit.

In 1998 J. Bay described his work about a silicon microphone for hearing aid application [9-12]. He presented the FEM simulations on double diaphragm microphones. The results include static deflection and the sensitivity to static sound pressure.

Ying showed the FE analysis of silicon condenser microphones with corrugated diaphragms [9-13] in 1998. Based on the FE simulation, Ying optimized the design parameters, for example the optimum number of corrugations and the optimum depth of the corrugation.

Generally the publicly presented FE models for silicon microphones have square or circular diaphragm. This chapter will present the simulation of a silicon condenser microphone with an octagonal diaphragm and a quadratic backplate. Furthermore, during the simulation shown

later, the open-circuit sensitivity is calculated according to the output voltage instead of the change in dynamic capacitance C_m. Both of them have not been done by the publicly presented simulation work yet.

9.3 Simulation of a silicon condenser microphone

This analysis has several approximations. First, the holes of the backplate are not included in the computer model. Second, the linear analysis but not the large deflection analysis is made.

Most definitions of the symbols that will be used in this chapter are the same as those defined in section 7.4. The different ones are the dimensions of the diaphragm L_B and the backplate L corresponding to R_B and R. They are illustrated in Fig. 9.2.

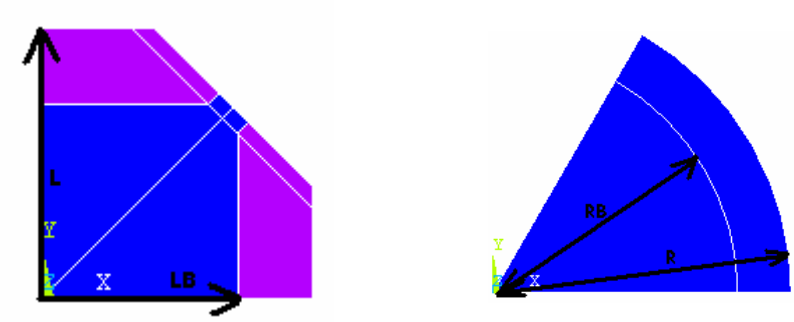

Fig. 9.2: The illustration of the dimension of the diaphragm and the backplate.

9.3.1 Computer model

The element type Shell63 is used to make the computer model. The element description can be found in section 8.2.1. The computer model is shown in Fig. 9.3. The blue part is the diaphragm area that is overlapped with the backplate. The purple part is the part of the octagonal diaphragm that is not overlapped with the backplate. The grid is the outline of the elements. The properties of the silicon microphone used are listed in Table 9.1.

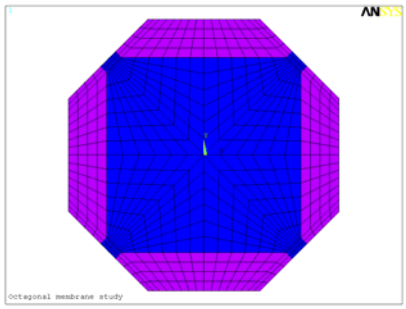

Fig. 9.3: The computer model for a silicon condenser microphone.

The calculated properties of an octagonal diaphragm are expected to be close to the properties of a circular diaphragm of the same size, which is L=R. This comparison gives an indication of the reliability of the simulated results of the octagonal diaphragm.

Table 9.1: The properties of the microphone.

Properties of the diaphragm	Value
Young's modulus E	$30\times10^{10}\ Pa$
Poisson's ratio ν	0.3
Density ρ	2300 kg/m^3
L	1.95 mm
Thickness h	0.5 μm
Air gap d_0	20 μm
Tensile stress σ	$340\times10^{6}\ Pa$

9.3.2 Static analysis

Resonance frequency

As shown in section 7.4.2, the first resonance frequency of a circular diaphragm is:

$$f_{res} = \frac{0.383}{R}\sqrt{\frac{\sigma}{\rho}} \tag{9.2}$$

Fig. 9.4 shows the first resonant mode of the octagonal diaphragm with the properties listed in Table 9.1, which is excited at 73.7 kHz. The color in Fig. 9.4 denotes the amplitude of the displacement. Red means the largest deflection while blue means the least deflection. According to eqn. (9.2), the resonance frequency of the same size circular diaphragm with the same properties is 75.5 kHz.

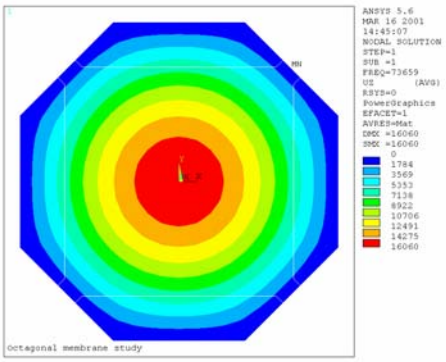

Fig. 9.4: The first resonance mode of an octagonal diaphragm.

In Fig. 9.5, 9.6 and 9.7 simulated results for the octagonal diaphragm are compared with the results obtained by eqn. (9.2) for the same size circular diaphragm. The deviation between the simulated results and the results according to eqn. (9.2) is 2.4%, 2.3% to 2.5% and 2.4% for Fig. 9.5, 9.6 and 9.7, respectively.

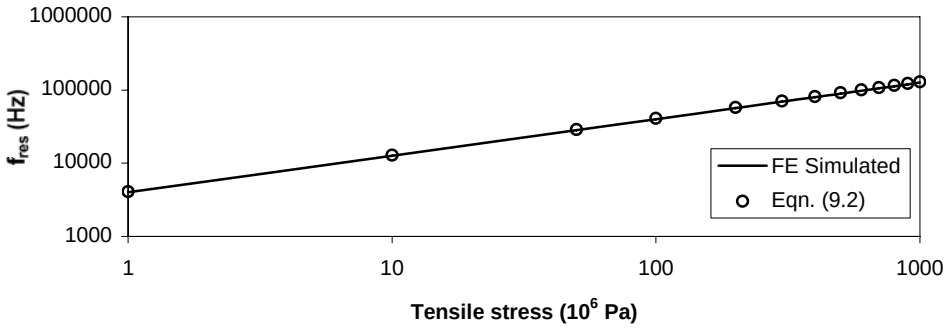

Fig. 9.5: Resonance frequency as a function of the tensile stress.

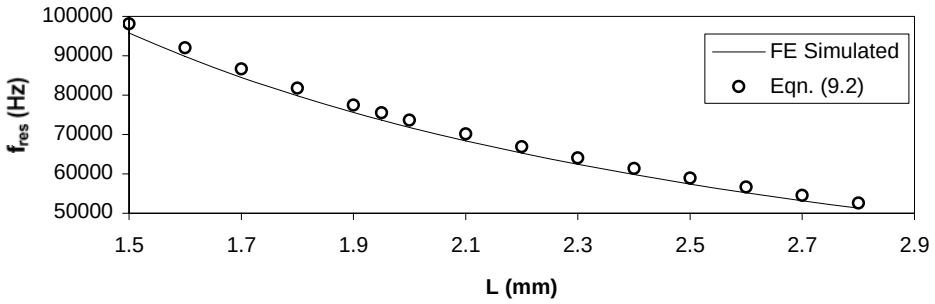

Fig. 9.6: Resonance frequency as a function of the diaphragm dimension.

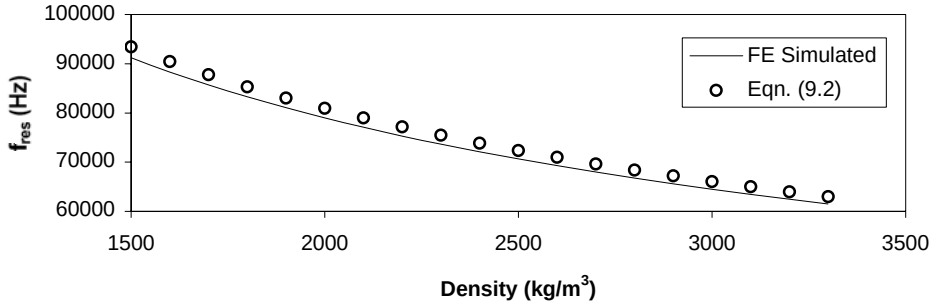

Fig. 9.7: Resonance frequency as a function of the diaphragm density.

The figures show that the first resonance frequency of the octagonal diaphragm is always smaller than that of the same size circular one. It is due to the fact that for the same dimension $L=R$ diaphragm, the octagonal one has bigger mass than the circular one illustrated by Fig. 9.2. At the same time, the octagonal one has lower stiffness than the circular one as will be shown in Fig. 9.8.

Though Fig. 9.5 shows that a good agreement is achieved for the comparison between the analytical and simulated results, there is a relative big difference at zero prestress. At zero prestress, the analytical first resonance frequency is zero, but the simulated one is 400 Hz. The reason is that the bending rigidity of a membrane is neglected in the analytical model, but not in the FE model. Since the practically used diaphragm for condenser microphones has more than 100 MPa tensile stress, the zero-difference is not a big deal.

All the changes are within the reasonable range of the practical situation. Therefore, we can obtain an analytical resonance frequency expression for the octagonal diaphragm:

$$f_{res} = \frac{0.373}{L}\sqrt{\frac{\sigma}{\rho}} \tag{9.3}$$

Static deflection profile

Fig. 9.8 gives the deflection with different diaphragm radius. The properties used are listed in Table 9.1 except the diaphragm dimension *L*.

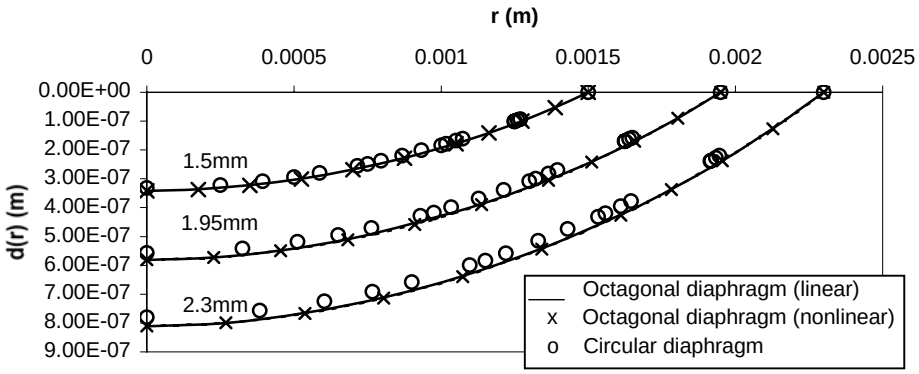

Fig. 9.8: Deflection profile as a function of the diaphragm dimension.

It can be seen that the deflection profile of an octagonal diaphragm is very close to that of the same size circular one. The figure also shows that for our case, whether the large deflection effects are included in the simulation process or not does not influence the simulated results. It is because that the diaphragm deflection is only up to 0.8 μm as shown in the figure.

Fig. 9.9 shows that the octagonal and circular diaphragm have similar normalized deflection profile when the studied point is in the range of *r/L*=0.5 to *r/L*=0 or *r/R*=0.5 to *r/R*=0 to. It is because that the deflection of the center part is so strong that the shape of the diaphragm does not influence the deflection where is close to the diaphragm center point. The difference increases as the *r/R* or *r/L* increases because the shape difference between the octagonal and circular diaphragm becomes bigger.

The simulated results on resonance frequency and deflection profile of an octagonal diaphragm are not very different from those of a same dimension circular diaphragm.

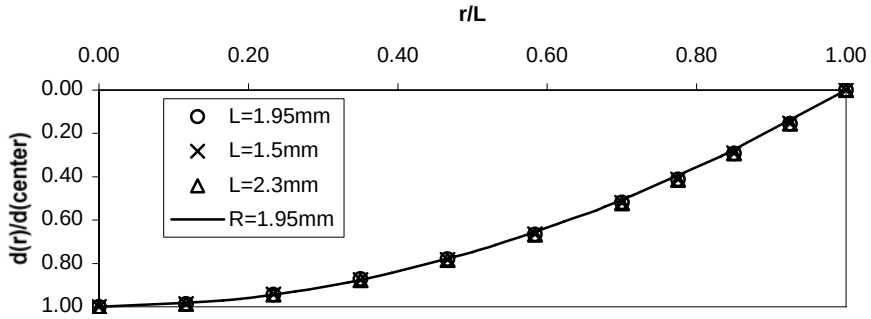

Fig. 9.9: Normalized deflection profile with different diaphragm dimension.

9.3.3 Collapse voltage

To simulate the collapse voltage, the model with square backplate is used as shown in Fig. 9.3. Fig. 9.10 shows the collapse voltage as a function of the dimension ratio between the diaphragm and the backplate. It can be seen that the collapse voltage decreases as the backplate dimension increases. The reason is that the decreased area of the stationary electrode (the backplate) decreases the total electrostatic forces acting on the diaphragm. Therefore the collapse voltage is increased.

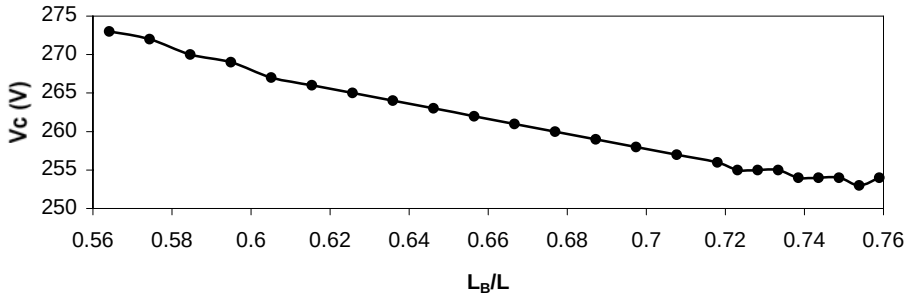

Fig. 9.10: Collapse voltage as a function of the dimension ratio between the diaphragm and the backplate.

The small wave around L_B/L=0.75 can be the result of the numerical errors. Since the largest square that fits within the octagonal shape is L_B=0.76×L, there are no simulation results for L_B/L >0.76.

A pure mathematic fitting function for the collapse voltage based on Fig. 9.10 can be expressed as

$$V_c(\lambda) = 395 - 276 \cdot \lambda + 71.9 \cdot \lambda^2 - 59.7 \cdot \lambda^3 \qquad (9.4)$$

where $\lambda = L_B / L$. The equation fits the simulations (dots in Fig. 9.10) within 1%.

Fig. 9.11 allows us to conveniently estimate the collapse voltage with different un-deflected distance between the diaphragm and the backplate, d_0. We can see that the collapse voltage

increases as the air gap distance at rest increases. A pure mathematic fitting function for the collapse voltage according to Fig. 9.11 shows that $V_c \propto d_0^{2/3}$.

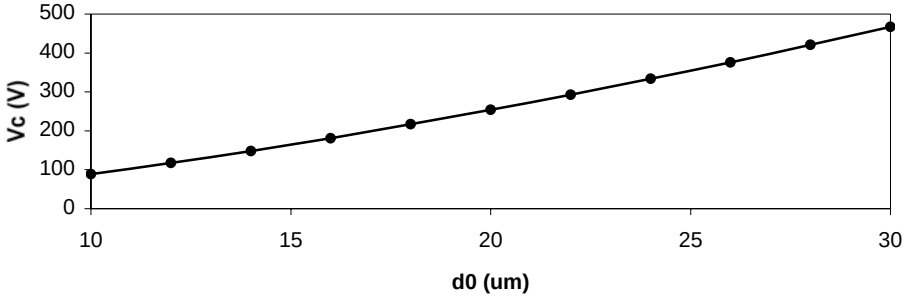

Fig. 9.11: Critical voltage as a function of the air gap distance d_0.

It can be seen from Fig. 9.12 that when the backplate becomes smaller, the more loading due to electrostatic forces gets concentrated at the center of the diaphragm, and the more the shape starts deviating from the parabolic shape. It should be noted that the V_c is different for all three backplate sizes.

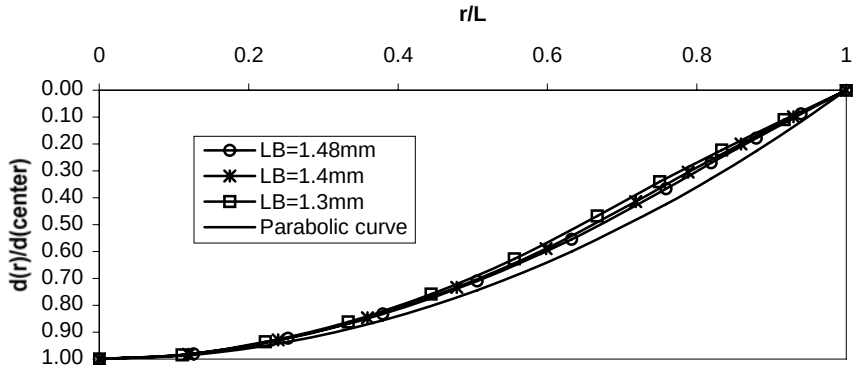

Fig. 9.12: Non-dimensionalized deflection of an octagonal diaphragm with 80% of *Vc*.

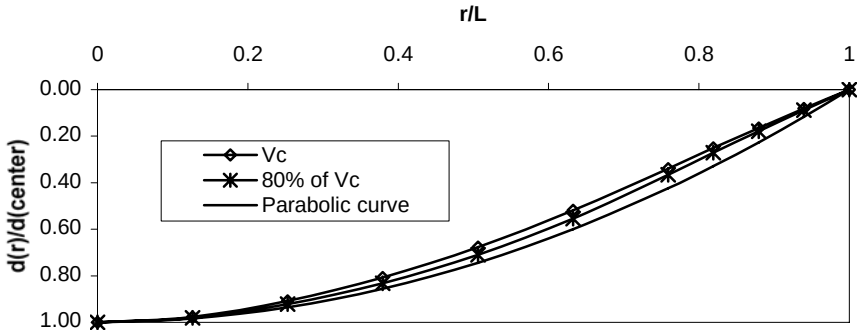

Fig. 9.13: Normalized deflection with *Vc* and 80% of *Vc* as a function of the position within the diaphragm (L=1.95mm, L_B=1.48mm).

Fig. 9.13 illustrates that the normalized deflection with 80% of *Vc* is more parabolic than that with *Vc*. It is because that when the bias voltage is closer to *Vc*, the loading on the diaphragm is more non-uniform. Consequently the deflection is less parabolic.

9.3.4 Open-circuit sensitivity

Same flow diagram as shown in Fig. 8.17 is used to calculate the open-circuit sensitivity except that the rear volume pressure is zero for silicon condenser microphones.

9.4 Experimental verification

In practice metal is evaporated to both sides of the (insulating) silicon nitride diaphragm to act as electrode. The specified properties of the gold electrodes are listed in Table 9.2. The procedure for the experimental verification is shown in Table 9.3. The specified properties of the microphone are taken from Table 9.1 except the density is changed to 3000 kg/m^3.

Table 9.2: The specified properties of the gold electrode.

Property	Value
Density	19.3×10^3 kg/m^3
Thickness	0.07 $\mu m \pm 20\%$

Table 9.3: Experimental procedure for verification of the FE model.

Measurement	Assumed Parameters	Derived Paramter
(1) Vacuum resonance frequency	Diaphragm thickness 0.50 μm Diaphragm size Diaphragm stress 340 Mpa	• Resonance frequency using effective diaphragm density • Diaphragm density/gold thickness from measured resonance frequency
(2) Collapse voltage	Diaphragm stress 340 Mpa Diaphragm thickness 0.50 μm Air gap distance 20 μm Diaphragm size Backplate size No holes in the backplate	Compare measured and simulated collapse voltage
(3) Capacitance at 0 V	Backplate size No holes in the backplate Air gap distance 20 μm	Parasitic capacitance
(4) Capacitance measured at 100 kHz	All parameters used and derived in (1) to (3) Parasitic capacitance from (3)	Compare measured and simulated results
(5) Open-circuit sensitivity	Same as in (4)	Compare measured and simulated results

In the first step, since the gold electrode changes the mass of the diaphragm, consequently it changes the resonance frequency. We take the effective diaphragm density ρ_{eff} to reflect the influence of the gold electrode.

$$\rho_{eff} = \rho_d + \frac{h_{au}}{h_d} \cdot \rho_{au} \tag{9.5}$$

where ρ_d is the diaphragm density, ρ_{au} is the gold density, h_d is the diaphragm thickness, and h_{au} is the gold electrode thickness.

Inserting the known parameters into eqn. (9.5), we have $\rho_{eff} = 5700\,kg/m^3$. Correspondingly the resonance frequency is 46.9 kHz.

Table 9.4 shows the effective diaphragm density and the gold thickness derived from the measured resonance frequencies of three silicon condenser microphones. It shows that the gold thickness of 1560068 and 1560077 fit the specified thickness $0.07\,\mu m$ within 6% while that of 1560078 fits $0.07\,\mu m$ within 32%. The 32% can be caused by the mismatch between the assumed and actually used parameters for the specific microphone.

Table 9.4: Effective diaphragm density and the gold thickness.

Microphone series number	Measured Resonance frequency	Effective diaphragm density	Gold thickness
1560068	47.1 kHz	5625 kg/m^3	$0.068\,\mu m$
1560077	47.4 kHz	5550 kg/m^3	$0.066\,\mu m$
1560078	50.7 kHz	4850 kg/m^3	$0.048\,\mu m$

Table 9.5 shows the results obtained in the second step. The reason why the simulated collapse voltages for the three microphones are the same is that we took the specified parameters for making simulation instead of taking particularly adjusted parameters as what had been done for the simulation of Type 4910 presented in Chapter 8. It is because no manually adjustment is done for the silicon condenser microphone production.

Table 9.5: The collapse voltage.

Microphone series number	Measured Collapse voltage	FE simulated collapse voltage
1560068	257 V	256 V
1560077	255 V	256 V
1560078	263 V	256 V

In the third step, by comparing the measured and simulated capacitance at 0 V, we obtain the parasitic capacitance, which is 5.09 pF.

Fig. 9.14 illustrates the results obtained in the forth step. It can be seen that a good agreement is achieved.

The measured open-circuit sensitivity of 1560068, 1560077, and 1560078 is 21.8 mV/Pa, 22.6 mV/Pa, and 20.5 mV/Pa, respectively. Since we took the specified parameters for making simulation, there is only one simulated sensitivity, which is 22 mV/Pa. Fig. 9.15 illustrates the simulation results.

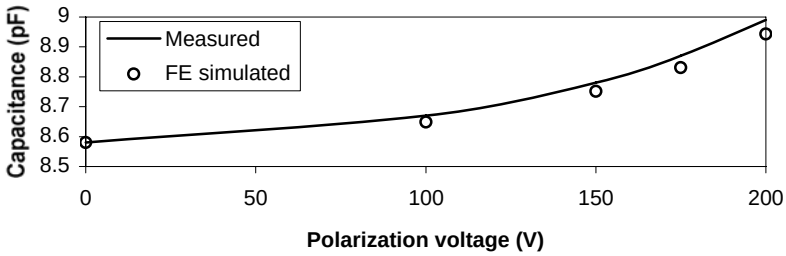

Fig. 9.14: The capacitance.

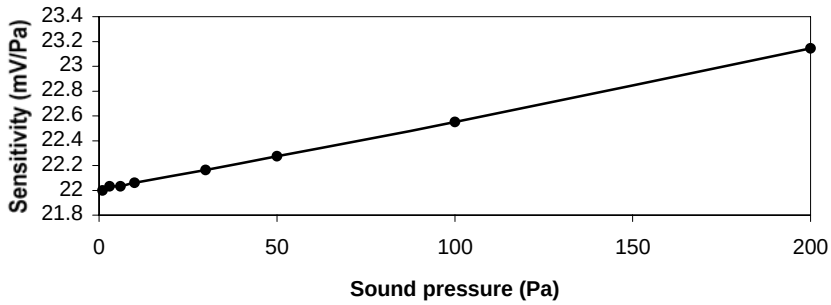

Fig. 9.15: Open-circuit sensitivity of silicon condenser microphone.

By making FFT analysis, the distortion at 200 Pa can be obtained by using the data shown in Fig. 9.15. But it has not been done.

The experimental verifications substantiate that the FE silicon condenser microphone modeling is successful. The FE simulated results can be regarded as reliable reference.

9.5 Optimization

The optimization of the backplate dimension is shown in Fig. 9.16, where $C_n = C_p / C_{00}$, C_p is the parasitic capacitance, C_{00} is the capacitance formed by the diaphragm and the backplate at rest. Due to the geometric limitation mentioned in section 9.4, only the backplate whose dimension is between 60% to 76% of the diaphragm dimension is considered. There is no analytical reference for the optimization.

It can be seen from Fig. 9.16 that the smaller the parasitic capacitance the bigger the sensitivity. This is because that $V = V_0 \cdot \frac{C_{00} + C_p}{C_m + C_p}$, where V_0 is the external polarization voltage.

Let's define $\lambda = L_B/L$. According to Fig. 9.16, the optimized λ is 0.73, 0.75 and 0.75 for C_n=0.33, 1.0, 3.0, respectively.

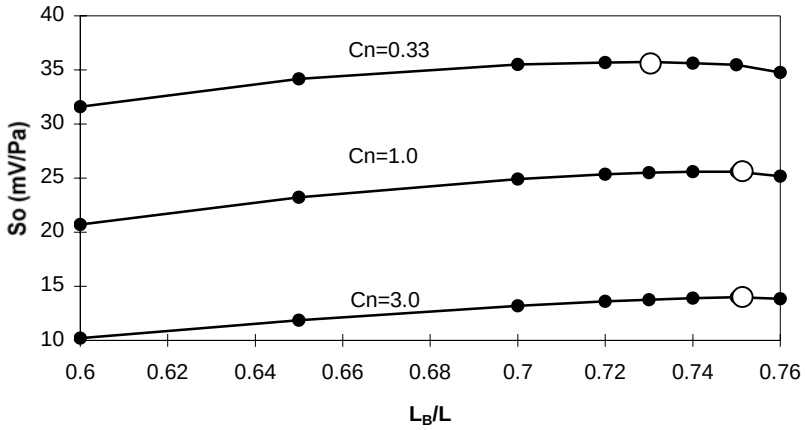

Fig. 9.16: The optimization of the backplate dimension.

Compared to the optimization made in Chapter 8 for circular microphones, the optimized λ with different C_n shown in Fig. 9.16 are much closer to each other. It may be because the similarity of the shape between the diaphragm and the backplate is much worse for silicon microphone than for circular microphone.

Since λ in Fig. 9.16 sits within a narrow range, the numerical error might be more sensitive for this case than for the optimization of a circular diaphragm in which λ is from 0 to 1. Further study needs to be done.

9.6 Conclusion

From the simulation results, we can obtain:

(1) An indication of the reliability of the FE simulation results of the octagonal diaphragm by the comparison between the calculated properties of an octagonal diaphragm and the analytical properties of a same size circular diaphragm.

(2) The collapse voltage estimation for different diaphragm and backplate dimensions according to eqn. (9.4).

(3) The collapse voltage estimation for different air gap distances according to Fig. 9.11.

(4) The accurate open-circuit sensitivity estimation.

(5) The optimization of the backplate dimension for silicon microphones according to Fig. 9.16.

The unique work done by the FEM is the basic study for an octagonal diaphragm with a quadratic backplate and the new method to simulate the open-circuit sensitivity for silicon

condenser microphones. Based on our results, it can be said that the project did a very good job for silicon condenser microphone simulation. It is valuable for helping practical design.

References

9-1 M. Royer et al., ”ZnO on Si integrated acoustic sensor”, Sensors and Actuators, 4, 1983, p.357-362

9-2 E.S. Kim and R.S. Muller, “IC-processed piezoelectric microphone”, IEEE Electron. Device Lett., EDL-8, 1987, p.467-468

9-3 R. Schellin and G. Hess, “A silicon subminiature microphone based on piezoresistive polysilicon strain gauges”, Sensors and Actuators A, 32, 1992, p.555-559

9-4 D. Hohm and G. Hess, “A subminiature condenser microphone with silicon nitride membrane and silicon backplate”, J. Acoust. Soc. Am., 85, 1989, p.476-480

9-5 J. Bergqvist and F. Rudolf, “New condenser microphone in silicon”, Sensors and Actuators, A21-A23, 1990, p.123-125

9-6 J. Bergqvist et al., ”A silicon condenser microphone with a highly perforated backplate”, Tech. Digest, 6th International Conference on Solid-State Sensors and Actuators (Transducers’ 91), June 1991, p.266-269

9-7 P.R. Scheeper et al., ”Fabrication of a subminiature condenser microphone using the sacrificial layer technique”, Tech. Digest, 6th International Conference on Solid-State Sensors and Actuators (Transducers’ 91), June 1991, p.408-411

9-8 W. Lukosz and P. Pliska, “Integrated optical interferometer as a light modulator and microphone”, Sensors and Actuators A, 25-27, 1991, p.337-340

9-9 D. Garthe, “A fiber-optic microphone”, Sensors and Actuators A, 25-27, 1991, p.341-345

9-10 F.B. Pourahmadi et al., ”Modeling of thermal and mechnical stresses in silicon microstructures”, Sensors and Actuators, A, 1990, p.850-855

9-11 J. Bergqvist, “Finite-element modeling and characterization of a silicon condenser microphone with a highly perforated backplate”, Sensors and Actuators, A, 39, 1993, p.191-200

9-12 Jesper Bay, “Silicon Microphone for Hearing Aid Applications”, Mikroelektronik Centret and Microtronic A/S, 1997, Ph.D. thesis

9-13 M. Ying et al., ”Finite-element analysis of silicon condenser microphone with corrugated diaphragms”, Finite Elements in Analysis and Design, 20, 1998, p.163-173

10
Conclusions and Suggestions for the Future Work

10.1 Conclusions

In this thesis a new development method for transducers for sound and vibration is described. Compared to the traditional design methods, which are the Equivalent Electrical Circuit and the trial-and-error, the new method, FEM, can make faster and better designs.

The work behind the thesis has led to some original contributions concerning the theory and technology of piezoelectric accelerometers and condenser microphones. These contributions are summarized below:

(1) The applicability of the FEM to the design of piezoelectric accelerometers and condenser microphones can be realized to the degree of precision required for R&D. Chapter 4 and 6 show that good agreements are achieved between the measurements and the simulations for existing piezoelectric accelerometers and new piezoelectric accelerometer designs, respectively. Chapter 8 and 9 show that good agreements are achieved between the measurements and the simulations for traditional and silicon condenser microphones, respectively.

(2) The scientific understanding of piezoelectric accelerometers and condenser microphones is improved. With FE simulation results, we have chances to visualize how the transducer operates at different resonant modes or under different circumstances, predict what is going to happen when the product is used. This allows the designers to solve problems and/or make better design fast.

(3) Basic study improves the scientific understanding for the piezoelectric accelerometer. Though some items of the study are already well known, the thesis gives the items both qualitatively and quantitatively. The improved understanding has been used together with virtual prototypes to make new designs. Experimental results substantiate that the methods work well.

(4) The method to simulate the open-circuit sensitivity for condenser microphones used in this thesis, to our knowledge, is presented the first time. It improves the simulation accuracy of the open-circuit sensitivity for the condenser microphone.

(5) The simulated properties of an octagonal diaphragm with a quadratic backplate are important for the future silicon condenser microphone design. Since there are not any analytical models for silicon condenser microphones, the FE simulation is the only reference.

(6) The simulation of the basic properties for condenser microphones gives the designers more opportunities to go to the physical limitation to get the best design. The optimization of the backplate dimension concerning the open-circuit sensitivity for both traditional and silicon condenser microphones can make the future design more efficiently.

10.2 Suggestions for the future work

The work described in this thesis leads to the following suggestions for continuation of the research.

(1) Piezoelectric accelerometers exhibit sensitivity to temperature transients. It is due to the pyroelectric effect and the non-uniform thermal expansion, which were explained in Chapter 2. Practically because of some complicated application circumstances, the temperature can change the accelerometers' performance much. Therefore, it is necessary to make temperature transient analysis. Unfortunately this analysis has not been finished yet. Future effort should be put on it.

(2) Shock analysis is useful to analyze how durable the transducers are. In fact, it is not a complicated analysis at all, only takes time to go through all programming work. It should be the very fist work to be done in the future.

(3) During the simulation for condenser microphones presented in this thesis, we used an ideal loss-free microphone model. The damping effect is completely neglected because the studied frequency in this thesis is far below the main resonance frequency. The sensitivity is simulated quasistatically, i.e., by observing the response to a static sound pressure load. This is valid for the flat stiffness-controlled part of the frequency response. By estimating the influence of viscous damping by a reduced Equivalent Electric Circuit, the frequency response at the full frequency range should be able to achieve by the combination of the FEM simulation and the Equivalent Electric Circuit.

(4) The physical prototypes should be made according to the optimization of the backplate dimension for both traditional and silicon condenser microphones in order to verify the simulated results.

References:

10-1 Patrick L. Walter, "Smart Transducer – Boon or Bane?", Sound and Vibration, June 2000, p.5

10-2 J. Bergqvist, "Finite-element modeling and characterization of a silicon condenser microphone with a highly perforated backplate", Sensors and Actuators, A, 39, 1993, p.191-200

List of Publications

"Finite Element Based Design and Optimisation for Piezoelectric Accelerometers"
B. Liu, Q. Yao and B. Kriegbaum, InterNoise 98', New Zealand

"The Development of Piezoelectric Accelerometers Using Finite Element Analysis"
B. Liu, Q. Yao and B. Kriegbaum, IMAC 99', USA

"Piezoelectric Accelerometers Modification Based on the Finite Element Method"
B. Liu and B. Kriegbaum, ICSV 99', Denmark

"Piezoelectric Accelerometers Modification Based on the Finite Element Method"
B. Liu and B. Kriegbaum, International Journal of Acoustics and Vibration, Feb. 2000, Volume 5, Number 3

"A New Annular Shear Piezoelectric Accelerometer"
B. Liu and B. Kriegbaum, IMAC 00', USA

"A New Annular Shear Piezoelectric Acceleomter"
B. Liu and B. Kriegbaum, Brüel & Kjær Technical Review

"A New Design for Triaxial Piezoelectric Accelerometer"
B. Liu and B. Kriegbaum, ICSV 01', Hong Kong